



**PREDICTIVE MESOSCALE MODEL FOR ROCKET
PROPELLANT DISPERSAL**

Tetsuji Yamada

**Yamada Science & Art Corporation
147 Monte Rey Drive South
Los Alamos NM 87544**

**ENVIRONICS DIRECTORATE
139 Barnes Drive, Suite 2
Tyndall AFB FL 32403-5323**

February 1996

Final Technical Report for Period November 1991 - November 1993

Approved for public release; distribution unlimited.

19960522 097

**AIR FORCE MATERIEL COMMAND
TYNDALL AIR FORCE BASE, FLORIDA 32403-5323**

ARMSTRONG

LABORATORY

NOTICES

This report was prepared as an account of work sponsored by an agency of the United States Government. Neither the United States Government nor any agency thereof, nor any employees, nor any of their contractors, subcontractors, or their employees, make any warranty, expressed or implied, or assume any legal liability or responsibility for the accuracy, completeness, or usefulness of any privately owned rights. Reference herein to any specific commercial products, process, or service by trade name, trademark, manufacturer, or otherwise, does not necessarily constitute or imply its endorsement, recommendation, or favoring by the United States Government or any agency, contractor, or subcontractor thereof. The views and opinions of the authors expressed herein do not necessarily state or reflect those of the United States Government or any agency, contractor, or subcontractor thereof.

When Government drawings, specifications, or other data are used for any purpose other than in connection with a definitely Government-related procurement, the United States Government incurs no responsibility or any obligation whatsoever. The fact that the Government may have formulated or in any way supplied the said drawings, specifications, or other data, is not to be regarded by implication, or otherwise in any manner construed, as licensing the holder or any other person or corporation; or as conveying any rights or permission to manufacture, use, or sell any patented invention that may in any way be related thereto.

This technical report has been reviewed by the Public Affairs Office (PA) and is releasable to the National Technical Information Service, where it will be available to the general public, including foreign nationals.

This report has been reviewed and is approved for publication.



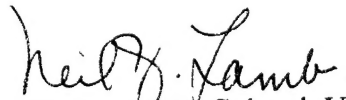
MICHAEL N. JONES, Capt, USAF
Project Manager



MICHAEL G. KATONA, PhD
Chief Scientist, Environics Directorate



EDWARD N. COPPOLA, Maj, USAF
Chief, Environmental Compliance Division



NEIL J. LAMB, Colonel, USAF, BSC
Director, Environics Directorate

REPORT DOCUMENTATION PAGE			Form Approved OMB No. 0704-0188	
<small>Public reporting burden for this collection of information is estimated to average 1 hour per response, including the time for reviewing instructions, searching existing data sources, gathering and maintaining the data needed, and completing and reviewing the collection of information. Send comments regarding this burden estimate or any other aspect of this collection of information, including suggestions for reducing this burden, to Washington Headquarters Services, Directorate for Information Operations and Reports, 1215 Jefferson Davis Highway, Suite 1204, Arlington, VA 22202-4302, and to the Office of Management and Budget, Paperwork Reduction Project (0704-0188), Washington, DC 20503.</small>				
1. AGENCY USE ONLY (Leave blank)		2. REPORT DATE February 1996	3. REPORT TYPE AND DATES COVERED Final Report 8Nov91 - 8Nov93	
4. TITLE AND SUBTITLE Predictive Mesoscale Model for Rocket Propellant Dispersal			5. FUNDING NUMBERS FO8635-91-C-0218	
6. AUTHOR(S) Tetsuji Yamada				
7. PERFORMING ORGANIZATION NAME(S) AND ADDRESS(ES) Yamada Science & Art Corporation 147 Monte Rey Drive South Los Alamos NM 87544			8. PERFORMING ORGANIZATION REPORT NUMBER	
9. SPONSORING / MONITORING AGENCY NAME(S) AND ADDRESS(ES) AL/EQS-OL 139 Barnes Drive, Suite 2 Tyndall AFB FL 32403-5323			10. SPONSORING / MONITORING AGENCY REPORT NUMBER AL/EQ-TR-1994-0005	
11. SUPPLEMENTARY NOTES Capt Michael N Jones, AL/EQS-OL, DSN523-6249				
12a. DISTRIBUTION / AVAILABILITY STATEMENT Approved for Public Release Distribution Unlimited			12b. DISTRIBUTION CODE	
13. ABSTRACT (Maximum 200 words) The purpose of this study was to upgrade the emergency response atmospheric modeling capabilities at Vandenberg Air Force Base (VAFB) with state-of-the-science three-dimensional forecast models adopted on an advanced scientific workstation. The contractor added new capabilities to HOTMAC (Higher Order Turbulence Model for Atmospheric Circulation) and RAPTAD (Random Puff Transport and Diffusion) to meet the objective of the project. Specific improvements included nested grids, four-dimensional data assimilation, incorporation of tower data, radiation transfer in clouds, precipitation microphysics, and positive and negative buoyancy plumes. The HOTMAC and RAPTAD modeling system was installed and tested on a workstation. The whole modeling system was delivered to VAFB for further tests.				
14. SUBJECT TERMS Complex Terrain Models, Simulation of Fog and Clouds, Emergency Response Plan, Continuous Forecast, HOTMAC, RAPTAD			15. NUMBER OF PAGES	
			16. PRICE CODE	
17. SECURITY CLASSIFICATION OF REPORT UNCLASSIFIED	18. SECURITY CLASSIFICATION OF THIS PAGE UNCLASSIFIED	19. SECURITY CLASSIFICATION OF ABSTRACT UNCLASSIFIED	20. LIMITATION OF ABSTRACT	

PREFACE

This report was prepared by Yamada Science & Art Corporation, 147 Monte Rey Drive South, Los Alamos, NM 87544, under contract number F08635-91-C-0218, for the Air Force Engineering and Service Center, Engineering and Services Laboratory (AFESC/RDVS), Tyndall Air Force Base, Florida, 32403-6001.

This report summarizes work performed between November 8, 1991 and November 8, 1993. Major Michael Moss and Captain Michael Jones were the AFESC/RDVS project officers.

(The reverse of this page is blank)

EXECUTIVE SUMMARY

OBJECTIVE

The purpose of this study was to upgrade the emergency response atmospheric modeling capabilities at Vandenberg Air Force Base with state-of-the-science three-dimensional forecast models adopted on an advanced scientific workstation.

BACKGROUND

While employed at Los Alamos National Laboratory, Principal Investigator (PI) of this study was PI of the project entitled "Three-Dimensional Modeling of Rocket Propellant Dispersion," which was sponsored by the U.S. Air Force Engineering and Services Center, Tyndall Air Force Base, FL. The purpose of that project was to demonstrate the feasibility of using a desk-top computer to operate three-dimensional hydrodynamic and diffusion models to describe the transport and dispersion of atmospheric pollutants at VAFB. To accomplish the objective, HOTMAC (Higher Order Turbulence Model for Atmospheric Circulation) and RAPTAD (Random Puff Transport and Diffusion) models were modified to run on an engineering workstation computer. The project was completed in April 1990.

HOTMAC and RAPTAD are significantly different from any AF models currently used at Vandenberg Air Force Base (VAFB). HOTMAC is a prognostic model and solves a set of time-dependent physical equations, such as conservation equations of momentum, internal energy, mixing ratio of water vapor, and turbulence variables. HOTMAC forecasts three-dimensional distributions of wind speed, wind direction, temperature, and moisture. The current AF models use a single wind value or a vertical profile of wind speed and direction at a single location. Clearly, a single value or a single profile of wind cannot provide realistic wind distributions for accurate transport and diffusion computations, because the terrain and meteorology in the VAFB area are highly heterogeneous. HOTMAC provided to RAPTAD both mean and turbulence variables to simulate transport and diffusion processes of airborne materials. Only a few mesoscale atmospheric models can forecast three-dimensional variations of atmospheric turbulence.

The HOTMAC/RAPTAD model results were compared with data collected during the Mountain Iron Diffusion experiments (Reference 4), which were conducted at VAFB in 1965 and 1966. HOTMAC and RAPTAD surface concentration predictions of fluorescent particles were found to be at least as good as those obtained by diagnostic models where wind data were available, and are potentially far better where wind data are not available.

Yamada and Bunker (Reference 13) showed that it was feasible to operate HOTMAC and RAPTAD on a desk-top computer. HOTMAC took 4 hours 11 minutes and 22 hours 10 minutes CPU time, respectively, on a Sun 4/110 workstation and a MicroVax 2000 computer for a 28-hour forecast with 21 X 25 X 16 grid points. RAPTAD took 26 minutes and 3 hours 45 minutes CPU time, respectively, on a Sun 4/110 workstation and a MicroVax 2000 computer for a 20 hour simulation. Significantly faster (approximately 7 times faster than a Sun 4/110) workstations have become available since the previous project was completed. The CPU times quoted above become much shorter with these new workstations.

The increased affordability and portability of workstations have opened the door to upgrading toxic-hazard modeling capabilities for emergency response management. The HOTMAC and RAPTAD modeling system will be a useful enhancement to current launch operation planning and emergency response management capabilities at VAFB.

TASKS

The following tasks were performed and are described in detail in Section III.

Task 1. Develop a method to incorporate National Meteorological Center's (NMC) Limited-Area Fine Mesh (LFM) and/or Nested Grid Model (NGM) weather forecast into HOTMAC.

Task 2. Develop a method to restart HOTMAC prediction, and maintain on disk predictions for the next 24 hours.

Task 3. Develop a method to combine upper-air wind-sounding and tower data taken at VAFB with HOTMAC forecast winds, so that RAPTAD can use the composite (forecast and observed) winds.

Task 4. Add to the model the physics necessary to forecast the formation and dissipation of fog.

Task 5. Develop an innovative method to treat plumes that are not neutrally buoyant.

Task 6. Develop a method to predict concentration variances, which are used to determine how a required confidence level affects the extent of a critical area.

Task 7. Perform model verification runs with a nested grid version of HOTMAC on a workstation.

Task 8. Upgrade computer capabilities used for emergency response modeling at VAFB.

METHODOLOGY

Section III.A.1 reviewed briefly the model equations, boundary conditions, and numerical schemes used in HOTMAC and RAPTAD. HOTMAC is a mesoscale atmospheric model that can forecast three-dimensional distributions of wind speed, wind direction, turbulence, temperature, and water vapor. The basic equations for HOTMAC are the conservation equations for mass, momentum, internal energy, mixing ratio of water vapor, and turbulence kinetic energy. Model physics in HOTMAC were improved considerably in order to simulate evaluation of cloud formation and precipitation processes. Interaction among radiation transfer, cloud development, and turbulent motion was included. Time variations of large-scale wind speed, wind direction, potential temperature, and mixing ratio of water vapor can be incorporated into HOTMAC by a four-dimensional data assimilation method.

RAPTAD is a Lagrangian puff code which uses the Monte Carlo statistical diffusion process. The center location and standard deviations of concentration distribution for each puff are computed by use of wind and turbulence which are modeled by HOTMAC. Concentration at any location is computed by the summation of the concentrations contributed by all of the puffs. RAPTAD can be used under extreme conditions with highly heterogeneous wind and turbulence distributions where a conventional Gaussian plume model may fail. Tower data may be incorporated into RAPTAD in addition to the wind distributions provided by HOTMAC. Buoyancy effects of plumes (positive and negative) were also included in RAPTAD.

RESULTS

Task 1: Four-Dimensional Data Assimilation

To test the simulation capabilities of HOTMAC, we selected data from Phase I WIND data (Reference 18). Horizontal wind components were nudged to the target wind components computed from observed winds, the Coriolis parameter, and a nudging parameter used in the equations of motion.

The Phase I was characterized by typical summertime anticyclonic conditions over the Sacramento River Valley in northern California. Southerly flow (upslope wind) during the day and northerly flow (downslope wind) at night were the characteristic flow patterns.

Comparisons between observations and simulations of the wind directions and speed, temperature, and dew point showed good agreement, both spatially and temporally, throughout entire 24-hour periods. Thus, a single station sounding could be used to represent large-scale meteorological conditions over the model domain.

Statistical parameters, including the mean and standard deviation of both the observed and simulated variables, the systematic and unsystematic components of the root-mean-square differences as well as the total root-mean-square difference (RMSD_s , RMSD_u , and RMSD , respectively), and the agreement measures, were calculated hourly using the surface station data. These statistical parameters were calculated for three different wind fields simulated by nudging to the target winds, with no nudging, and persistence. The wind fields obtained by nudging to target winds yielded better agreement in wind direction and speed when compared to the two other wind fields.

Wind Distributions at 6 Meters agl at 1500 LT on Day 233. Similar to Figures 37 and 43, But Without a Nested Grid

Task 2: Continuous Forecast

A complex scheme was developed to operate HOTMAC and RAPTAD interactively. HOTMAC runs continuously and always maintains 24-hour forecast data. The interactive scheme dictates that as soon as RAPTAD starts computation, HOTMAC halts its forecasting.

Once a 24-hour forecast is completed and the forecast data are written to a disk, HOTMAC "sleeps" until the next computation time. HOTMAC "wakes up" at the clock hour and begins to advance the forecast one hour.

In addition to using the default mode's 24-hour forecast, the user can extend the range of the forecast period manually, up to 48 hours or longer, for planning operations.

Task 3: Tower Data Input

Winds measured by upper-air soundings and at towers were combined with the winds forecasted by HOTMAC. A simple $1/r^2$ weighting method was used to compute the wind at a puff center. The winds at puff centers (obtained from tower winds) were then combined with winds computed by HOTMAC. Tower winds are weighted based on the distance between a puff center and the nearest tower site. If a puff is located at a tower site, then the tower wind is used for puff velocity. The weight function decreases exponentially as the distance between a puff and a tower increases. Such an assumption is reasonable, particularly for airflows over complex terrain, where wind distributions are largely localized.

Task 4: Simulation of Fog

Fog and low stratus clouds are frequently observed at VAFB, and affect the heat energy balance at the ground. The interaction of fog, solar heating, long-wave radiation heating/cooling, and turbulence mixing is complex and is not yet well understood. A simulation of fog consists of modeling condensation, radiation transfer, and precipitation microphysics. Condensation processes were simulated by an ensemble cloud model which is described in detail in Section III.D.1.

The terms for the rate of condensation are purposely eliminated by introducing the liquid water potential temperature and mixing ratio of total water. In order to recover the potential (or absolute) temperature and the mixing ratios of water vapor and liquid water, Gaussian cloud relations, proposed by Sommeria and Deardorff (Reference 33) and Mellor (Reference 34), are used. The present method has been applied to simulations of the BOMEX data (Reference 35), and GATE data (Reference 36).

Solar and long-wave radiation play important roles in the formation and dissipation of clouds and fog. Hanson and Derr (Reference 39) proposed a parameterized solar radiation scheme whose parameters were obtained by curve-fitting to numerical radiative-transfer results using the ATRAD narrow-band model (Reference 40). This parameterized method is simple, yet reproduced solar flux profiles within a single cloud layer which were in good agreement with the numerical results obtained from ATRAD.

Motivated by the success of the solar radiation scheme, Hanson and Derr proposed an infrared (IR) radiation scheme expressed by exponential functions whose decay parameters were determined by the emissivity methods (Reference 41). This method reproduced IR flux profiles within layered clouds which were in good agreement with the numerical results and observations for thick clouds (~800 meters). However, the parameterization overestimated the flux decrease at the cloud top and underestimated the cloud-base warming compared to the numerical model for thin clouds (~300 meters).

We adopted the Hanson and Derr parameterization scheme because of its simplicity and because it can produce flux profiles which are in good agreement with observations and numerical model results.

We adopted the precipitation microphysics proposed by Nickerson et al. (Reference 43). This hydrological model is substantially more complex than Kessler's (Reference 44) classical parameterization for the treatment of microphysics. The model is based on a more realistic log-normal distribution than the Marshall-Palmer distribution in Kessler's parameterization. The mean diameter of raindrops in a given volume is estimated from equations for the mean rain water mixing ratio and the raindrop number concentration. The terminal velocity of raindrops in each volume is calculated as a function of the mean raindrop diameter, thus the terminal velocities in the model are expected to be more accurate than those obtained by a simple parameterization.

Maritime stratus clouds were simulated by using a one-dimensional version of HOTMAC (Reference 20). Integration initiated at 0000 LT (Local Time) on day 200 (July 19) and continued for 48 hours. The results for the second 24-hour simulations are presented here. Clouds were thick during the nocturnal period and occupied the layer between 1200 meters and 1600 meters above the sea surface. As the short-wave solar radiation heating increased, clouds dissipated from the lower part and clouds became as thin as 100 meters by 1800 LT. As the solar heating subsided, the cloud thickness increased again.

A one-dimensional version of HOTMAC was used to simulate time evolution of fog over a horizontally homogeneous terrain. The results were compared with data taken at Cabaw meteorological tower in the Netherlands (Reference 31). Fog began to form almost immediately, as the air temperature decreased due to cooling at the ground. The height of the fog increased as the air temperature near the fog top decreased due to long-wave radiation cooling. The modeled and observed temperature and mixing

ratio of water vapor at 1.1 meters above ground level (agl) were in good agreement with observations.

Task 5: Non-neutrally Buoyant Plumes

Highly buoyant plumes modify the wind and turbulence distributions of the ambient flow. It is almost impossible to parameterize or express such modifications without deploying a dynamic plume model. A physically correct way to treat non-neutrally buoyant plumes is to incorporate plume dynamics into HOTMAC. However, the dynamic plume model requires considerable computer time and is not practical for emergency modeling. This is a dilemma, for one must choose between being accurate (but impractical) and being practical (but inaccurate). It is therefore necessary to adopt a plume parameterization scheme (instead of a dynamic plume model) to meet the time constraints of an emergency response modeling system.

Following Van Dop (Reference 45), the vertical velocity of a buoyant plume is computed from the Langevin equation of motion for a homogeneous and stationary turbulent flow. The temperature of a buoyant plume is also assumed to be computed by the Langevin equation.

Test simulations were conducted under neutral conditions ($N^2 = 0$) and the results were compared with analytical solutions. Simulations and analytical solutions were in good agreement. Simulations were repeated under stable ($N^2 > 0$) and unstable ($N^2 < 0$) atmospheric conditions. Finally, simulations were conducted for a plume whose initial density is heavier than the ambient air.

All simulations were conducted with an integration time step of 0.1 seconds. Accuracy decreased rapidly with increases in the integration time step. RAPTAD uses a time step of 10 seconds, but a small time step was necessary to simulate initial plume rise (drop) accurately. Therefore, a time step which increased linearly with time was used: time step was 0.1 seconds initially and became 10 seconds at 100 seconds after the release.

Task 6: Concentration Variance

Relatively short time-averaging values are required for predicting concentrations of toxic materials. Such values normally exhibit great variations in time and space. Thus, predictions of not only the mean but also the variance of concentrations are essential to determine the extent of a critical area

where concentration values exceed a given limit. The size of a critical area becomes larger if a higher confidence level is required.

Only a limited number of concentration fluctuation measurements are available for comparison. The best measurements were obtained by using wind tunnels. Preliminary comparisons indicate that our simulations are qualitatively in good agreement with wind tunnel data. Both standard deviations, and ratios of standard deviation to mean, showed characteristics similar to those found in measurements where measured mean wind and turbulence were used in RAPTAD computation. No effort was made to compare simulations with atmospheric data because we are not aware of such data.

Task 7: Nested Grid

A nested grid version of HOTMAC had been used with a Cray supercomputer, but it had never been used with a workstation because it would require too much computer time. However, with the rapid advancement of workstation performance, we are now able to run a nested grid version of HOTMAC on a workstation. Test simulations have been performed to demonstrate systematically how nested grids improve the simulation of wind distributions. A two-way nesting method was used: the outer grid provided boundary values to the inner grid, and the inner grid updated outer grid values with new values at grid points common to both grids.

Simulations were conducted with and without nested grids. Three nested grids were used in a control run. Wind distributions at 1500 LT for a single grid case were similar to those for the control run because strong mixing in the vertical direction, due to turbulence, resulted in almost uniform wind distributions. On the other hand, wind distributions at 0200 LT were considerably different from those for the control run, particularly in the area where Grid 3 was nested.

Task 8: Computer Capability Upgrade

Based on discussions between the personnel at VAFB and YSA, the following computer hardware and software were selected:

1. A Sun SPARCstation 10 with 32 Mb RAM, 19" color monitor, 400 Mb internal SCSI disk, 1.44 Mb $3\frac{1}{2}$ " internal floppy disk.

2. A 1.2 Gb external disk.
3. A 150 Mb tape drive.
4. A CD drive.
5. Sun FORTRAN compiler.
6. Sun C compiler.
7. NCAR Graphics.

Hardware and software were installed and tested at YSA, and delivered to VAFB.

CONCLUSION

- It is feasible to operate on a workstation, a nested-grid, three-dimensional atmospheric model, HOTMAC, and a three-dimensional dispersion model, RAPTAD, to forecast the transport and diffusion of airborne materials at VAFB.
- The computer capabilities for emergency response applications at VAFB were upgraded. HOTMAC and RAPTAD were installed and tested on a Sun SPARCstation10.
- HOTMAC was modified to run continuously and store wind and turbulence predictions and data for the next 24 hours. When an emergency occurs, RAPTAD can be used immediately with the wind data stored on a disk. The RAPTAD computation is much faster than that of HOTMAC. This approach meets better the time constraints of emergency situations.
- A method was developed to integrate large-scale weather data into HOTMAC. The weather data are used to initialize and correct HOTMAC forecasts. A four-dimensional data assimilation method was used.
- A method was developed to predict concentration variances which can be used to estimate uncertainties associated with predictions.
- Model physics necessary to simulate the evolution of fog formation and dissipation processes were added. Fog is frequently observed at VAFB and affects the heat energy balance at ground level.
- Positive and negative buoyancy effects of plumes were incorporated to RAPTAD.

RECOMMENDATIONS

- Become familiar with background theories and operating procedures of HOTMAC and RAPTAD. Increase experience by running models under different weather conditions.
- Consider customizing pre- and post- processors of HOTMAC and RAPTAD to meet specific needs at VAFB. The current versions of HOTMAC and RAPTAD are designed for general applications.
- Continue to upgrade computer capabilities at VAFB. Computer hardware technology is expected to advance further and to allow much more sophisticated models to be operated in much less time than previously considered possible.
- Continue to improve model physics in HOTMAC and RAPTAD. These codes have model physics which are considered to be the state-of-the-science but still are far from fully replicating the complex physics of the real atmosphere. Particularly, we recommend strongly that the new model physics added here (precipitation microphysics, radiation transfer in fog and clouds, and positive and negative plume buoyancy effects) be tested, by comparing simulations with observations.

TABLE OF CONTENTS

Section	Title	Page
I	INTRODUCTION	1
	A. OBJECTIVE	1
	B. BACKGROUND	3
	C. SCOPE	8
II	PREVIOUS STUDY	9
III	WORK PERFORMED	12
	A. TASK 1	12
	1. Model	13
	2. Evaluation of Model Performance	16
	3. Simulation of Phase I Data	18
	B. TASK 2	36
	C. TASK 3	37
	D. TASK 4	47
	1. Ensemble Cloud Modeling	47
	2. Short-Wave and Long-Wave Radiation Parameterizations	50
	3. Precipitation Microphysics	55

TABLE OF CONTENTS (CONCLUDED)

Section	Title	Page
	4. Simulation of Maritime Stratus Clouds	56
	5. Simulation of Fog	62
	E. TASK 5	62
	F. TASK 6	65
	G. TASK 7	76
	H. TASK 8	90
IV	CONCLUSION AND RECOMMENDATIONS	91
	A. CONCLUSION	91
	B. RECOMMENDATIONS	91
	REFERENCES	93

LIST OF FIGURES

Figure	Title	Page
1.	Modeled Horizontal Wind Vectors for the MI87 Case at 4 Meters agl from the WOCSS Diagnostic Wind Model. Meteorological Measurement Stations are identified by Numbers	4
2.	Modeled Horizontal Wind Vectors for the MI87 Case at 10 Meters agl from the LINCOM Diagnostic Wind Model	5
3.	Modeled Horizontal Wind Vectors for the MI87 Case at 10 Meters agl from the HOTMAC Prognostic Wind Model	7
4.	Model Domain (200 X 200 Kilometers) for WIND Phase I Simulation. Terrain is Contoured by Solid Lines in Increments of 400 Meters. The Lowest Contour is 400 Meters above Mean Sea Level. The Locations of Surface Stations are Indicated by Characters. Numbers in Parentheses represent Upper-Air Stations	20
5.	Surface (10-Meter Level) Horizontal Wind Vector Distributions for Phase I at 1500 LT of Day 178. (A) the Simulation with Nudging, (B) Observations, (C) the Target Wind Field, and (D) the Simulation without Nudging. An Arrow with a Unit Grid Distance represents 10 m/sec	22
6.	Same as Figure 5 except at 0500 LT of Day 179	23
7.	Time Evolutions of Surface Meteorological Variables During the 24-Hour Period of the Project WIND Phase I, at (A) Station S2, (B) Station S10, (C) Station S14, (D) Station C3. (- Simulation, and o Observation)	25

LIST OF FIGURES (CONTINUED)

Figure	Title	Page
8.	Time Evolutions of Statistical Parameters of Surface (10-Meter Level) Wind Speed and Direction for 24-Hour Period of Phase I for the Simulation with Nudging to the Target Winds. From the Top, Mean Wind Direction (– Simulation, and o Observation), Mean Wind Speed (– Simulation, and o Observation), Standard Deviation of Wind Speed (– Simulation, and o Observation), Root-Mean-Square Differences (* RMSD, x RMSD _u , and o RMSD _s), and Agreement Measure of Wind Speed. (A) Winds were Nudged to the Target Winds, (B) No Nudging was applied, and (C) Persistence Winds were used	28
9.	Time Evolutions of Statistical Parameters of Surface (2-Meter Level) Temperature. From the Top, Mean (– Simulation, and o Observation), Standard Deviations (– Simulation, and o Observation), Root-Mean-Square Differences (*RMSD, x RMSD _u , and o RMSD _s), and Agreement Measure	32
10.	Time Evolution of Wind Direction, Wind Speed, Temperature and Dew Points at Different Heights (agl) at Upper-Air Station 1 during the 24-Hour period of Phase I (– Simulation, and * Observation)	33
11.	Vertical Distributions of Wind Direction and Speed, Temperature and Dew Point at Station 4 for Phase I. (A) 1100 LT, Day 178, (B) 1700 LT, Day 178, (C) 0100 LT, Day 179, (D) 0700 LT, Day 179 (– Simulation, and o Observation)	35
12.	Wind Vectors at Tower Locations (With Numbers) and those at Puff Centers (Without Numbers) at 1110 LT, January 11, 1993. Puff Velocities were Extrapolated from Tower Velocities	38
13.	Similar to Figure 12 but for January 12, 1993	39
14.	Similar to Figure 12 but for January 13, 1993	40
15.	Similar to Figure 12 but for January 14, 1993	41

LIST OF FIGURES
(CONTINUED)

Figure	Title	Page
16.	Similar to Figure 12 but for January 15, 1993	42
17.	Wind Vectors at Tower Locations (With Numbers) and those at Puff Centers (Without Numbers) at 0300 Z, January 12, 1993. Puff Velocities were Computed from Tower Data and HOTMAC Winds by $1/r^2$ Weighting Method.	43
18.	Similar to Figure 17 but for 0600 Z, January 12, 1993	44
19.	Similar to Figure 17 but for 0900 Z, January 12, 1993	45
20.	Similar to Figure 17 but for 1100 Z, January 12, 1993	46
21.	Fraction of Cloud Coverage R , Mixing Ratio of Liquid Water $Q_c/2\sigma_s$, and Variance of Liquid Water, $\overline{q_c^2}/4\sigma_s^2$ as a Function of Q_1	50
22.	Diurnal Variation of the Cloud Water Mixing Ratio. Simulation of Maritime Stratus Cloud. Contour From 0 to 128 with an Interval of 8. Labels Scaled by $1.0e0.5$	57
23.	Similar to Figure 22, except for the Rain Water Mixing Ratio (g/g). Contour from 0 to 720 with an Interval of 40. Labels Scaled by $1.0e0.6$	58
24.	Similar to Figure 22, except for the Short-Wave Radiation Cooling Rate ($^{\circ}\text{C}/\text{day}$). Contour From 0 to 180 with an Interval of 10	59
25.	Similar to Figure 22, except for Long-Wave Radiation Cooling Rate ($^{\circ}\text{C}/\text{day}$). Contour from -190 to 20 With an Interval of 10	60
26.	Diurnal Variation of the Cloud Water Mixing Ratio. Simulation of Radiational Fog. Contour from 0 to 600. Labels Scaled by $1.0e0.6$	61

LIST OF FIGURES
(CONTINUED)

Figure	Title	Page
27.	Time Variations of Modeled (-) and Observed (*) Temperature and Mixing Ratio of Water Vapor at 1.1 Meters agl	63
28.	Time Variations of Buoyancy (m/s^2), Vertical Velocity (m/s), and Plume Height (m) in the Neutral Condition. Initial Buoyancy of 1 m/s^2 and Initial Vertical Velocity of 0.1 m/s were used	66
29.	Time Variation of Buoyancy (m/s^2), Vertical Velocity (m/s), and Plume Height (m) in the Stable Condition ($N^2 = (0.408)^2$). Initial Buoyancy of 1 m/s^2 and Initial Vertical Velocity of 0 m/s were used	67
30.	Similar to Figure 29 except in the Unstable Condition ($N^2 = -(0.408)^2$)	68
31.	Similar to Figure 29 except Initial Buoyancy of -1 m/s^2 was used	69
32.	Similar to Figure 30 except Initial Buoyancy of -1 m/s^2 was used	70
33.	Similar to Figure 32 except Variable Integration Time Steps of 0.1 Seconds to 10 Seconds were used	71
34.	Examples of Time Variations of Mean Concentration (Top) and Ratio of Standard Deviation to Mean Concentration at Station B	73
35.	Similar to Figure 34 except at Station C	74
36.	Similar to Figure 34 except at Station I	75

LIST OF FIGURES (CONCLUDED)

Figure	Title	Page
37.	Wind Distributions at 6 Meters agl at 1500 LT on Day 233. Arrows indicate Wind Vectors, whose Scale is shown at the Left Upper Corner. Solid Lines indicate Ground Elevation Contours in increments of 50 Meters. Areas enclosed by Dashed Lines show Nested Grids. Computation Domains are referred to as Grid 1, Grid 2, and Grid 3 for the Outer, Intermediate, and Inner Grids, respectively	77
38.	Similar to Figure 37 except Showing Grid 2. The Area enclosed by the Dashed Lines shows the Grid 3 Domain	78
39.	Similar to Figure 37 except showing Grid 3	79
40.	Similar to Figure 32 except at 0200 LT on Day 234	80
41.	Similar to Figure 40 except showing Grid 2. The Area enclosed by the Dashed Lines shows the Grid 3 Domain	82
42.	Similar to Figure 40 except showing Grid 3	83
43.	Similar to Figure 37, but using only Grid 1 and Grid 2	84
44.	Similar to Figure 38, but using only Grid 1 and Grid 2	85
45.	Similar to Figure 40, but using only Grid 1 and Grid 2	86
46.	Similar to Figure 41, but using only Grid 1 and Grid 2	87
47.	Wind Distributions at 6 Meters agl at 1500 LT on Day 233. Similar to Figures 37 and 43, but without a Nested Grid	88
48.	Similar to Figure 47 except at 0200 LT on Day 234	89

(The reverse of this page is blank)

SECTION I

INTRODUCTION

A. OBJECTIVE

The objective of this effort was to upgrade the emergency response atmospheric modeling capabilities at VAFB with state-of-the-science three-dimensional forecast models adopted on an advanced scientific workstation. Air Force (AF) models designed to calculate the atmospheric transport and dispersion of pollutants at Vandenberg Air Force Base (VAFB) include the Rocket Exhaust Effluent Dispersion Model (REEDM) system (Reference 1; Reference 2) and the Ocean Breeze/Dry Gulch (OB/DG) equation (Reference 3), Mountain Iron (MI) equation (Reference 4; Reference 5), and Sudden Ranch (SR) equation (Reference 6). REEDM was designed to model the transport and dispersion of buoyant plumes of rocket exhaust during normal launch, and fireball rise and subsequent dispersion in the event of an explosive accident. OB/DG, MI, and SR are empirical equations designed to calculate toxic-hazard corridors resulting from accidental spills of toxic chemicals. These models assume that the wind field over the geographical area of interest can be adequately represented by the wind speed and direction measured at a single point (or, in the case of REEDM, a vertical profile of wind speed and direction over a single site). These models also assume that the toxic plume or puff released to the atmosphere is uniformly distributed around a center line determined from the wind direction measured at the single observation site.

While the model and equations listed above have been acceptable in the past, the complex terrain and meteorology at VAFB, increased amounts of toxic chemicals stored there, increases in the surrounding civilian population, higher anticipated launch rates, and the reduction in personal exposure limits for the AF chemicals of interest (nitrogen tetroxide and Aerozine-50) require more accurate methods. Current efforts to improve VAFB's modeling capabilities include development of the Air Force Toxic (AFTOX) Chemical Dispersion model (Reference 7) by the Air Force Geophysics Laboratory (AFGL). AFTOX, in its current form, however, also assumes

that the three-dimensional wind field can be represented by a single wind value. Efforts have been made to couple AFTOX with a surface-layer wind-flow model; however, the complexity of the terrain and meteorology at VAFB require a model that takes into account the three-dimensional wind field over the entire VAFB region.

A considerable number of wind-field models exist that could produce three-dimensional wind distributions over complex terrain. These wind models are of two types:

1. Diagnostic wind models that construct the wind distribution by using existing measurements plus some physical constraints of varying extent.
2. Prognostic wind models that use a set of hydrodynamic equations to predict the wind and turbulence fields.

Diagnostic wind models are based on measurements and interpolation. Most of these models adjust initially interpolated wind fields to satisfy a mass-conservation equation. The accuracy of the model results is greatly dependent upon the quality and representativeness of the measurements.

Diagnostic wind models have been used almost exclusively for emergency response management because they are simple and fast. The critical weakness of this class of models, however, is their lack of predictive capability. Plume models based upon diagnostic wind models must assume that the current wind field will persist until it is updated by future measurements. The assumption of persistency is adequate if the measurements are made frequently and if no abrupt change in the wind field occurs. However, such conditions limit the area of concern to the immediate vicinity of the source, and exclude predictions during the transitional periods between daytime and nighttime conditions. Wind speeds, wind directions, and turbulence change rapidly during the transitional periods.

The question of the representativeness of measurements further limits the applications of diagnostic wind models to simple terrains, because complex surface boundaries require a prohibitively large number of wind measurements.

Prognostic models, on the other hand, solve a set of time-dependent physical equations, such as conservation equations of momentum, internal energy, and the mixing ratio of water vapor. Prognostic models forecast three-dimensional wind field distributions that become the input to transport and diffusion models. For this reason, the terms "prognostic" and "forecast" are used interchangeably in this proposal.

At present, prognostic models have not been used in emergency response systems, because a large amount of computation time was required. This situation should improve considerably in the near future, because the capabilities of engineering workstations are expected to advance at an astonishing rate. Previous AF efforts to improve toxic-hazard models have been limited by available computer power. Recent developments in computer hardware technology, however, have the potential to allow much more sophisticated models to be operated in much less time than previously considered possible.

B. BACKGROUND

There have been considerable efforts to develop three-dimensional wind models that can be used to simulate wind distributions over the area surrounding Vandenberg Air Force Base. A comprehensive review of the present emergency modeling system (REEDM) at VAFB, discussions on candidate wind-field models (both diagnostic and prognostic) for replacement of the current REEDM wind-field model, and recommendations for short- and long-term future improvements are given in recent reports by Conley (Reference 8).

For example, Figure 1 shows the modeled horizontal wind vectors at 4 meters above-ground-level (agl) by using the WOCSS (Winds On Critical Stream Surfaces) diagnostic wind model (Reference 9). WOCSS is the enhanced version of SRI Complex developed by SRI International (Reference 10). An array of 50 X 80 X 6 with a 500-meter grid spacing and the terrain data of a 500-meter resolution were used. Wind vectors at every fourth grid point are shown in Figure 1.

Figure 2 shows the modeled wind vectors at 10 meters agl at 1310 Local Time (LT) by using LINCOM (Reference 11), which is a linear, diagnostic, spectral, and potential-flow wind model.

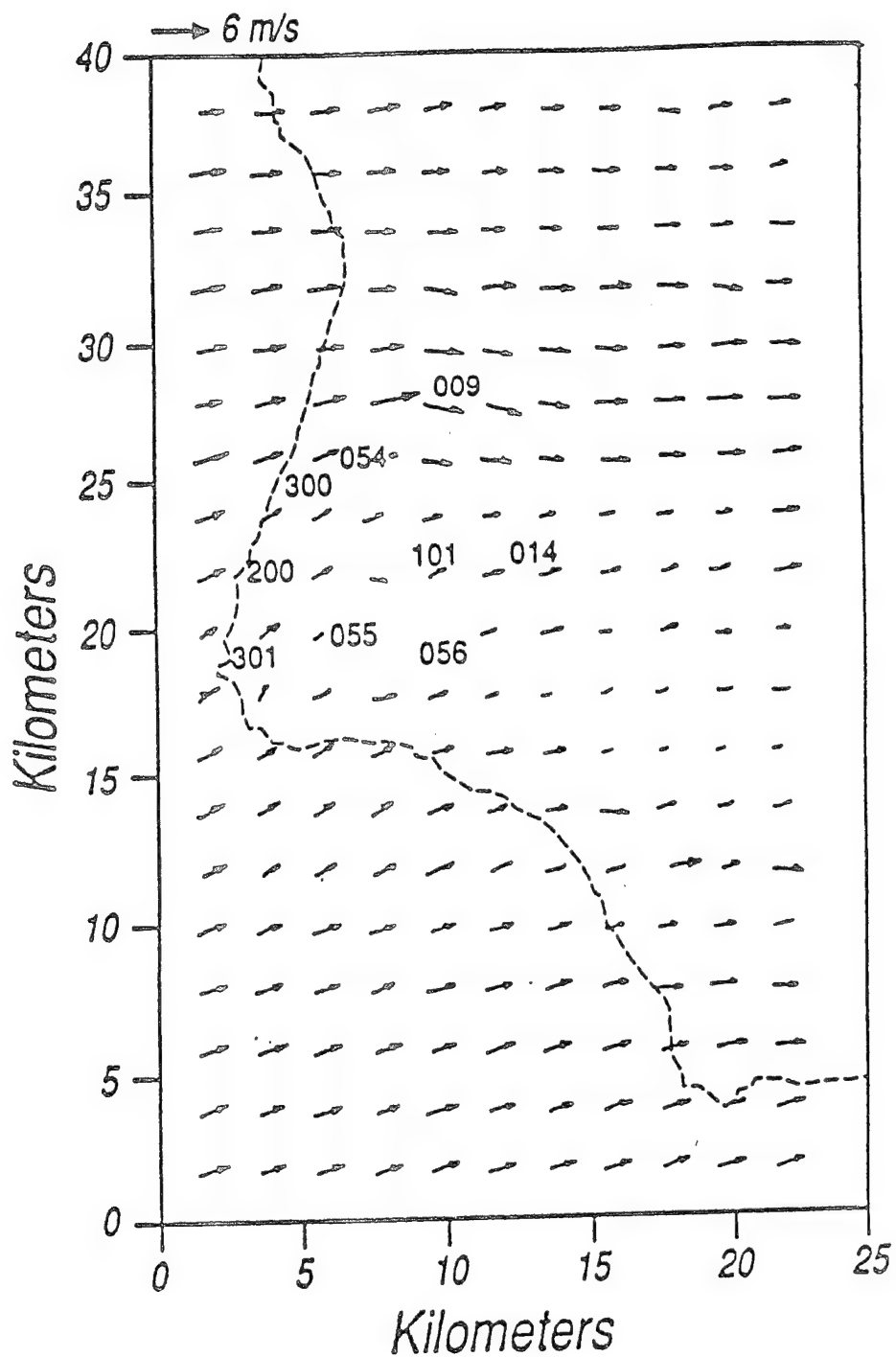


Figure 1. Modeled Horizontal Wind Vectors for the MI87 Case at 4 Meters agl from the WOCSS Diagnostic Wind Model. Meteorological Measurement Stations are identified by Numbers.

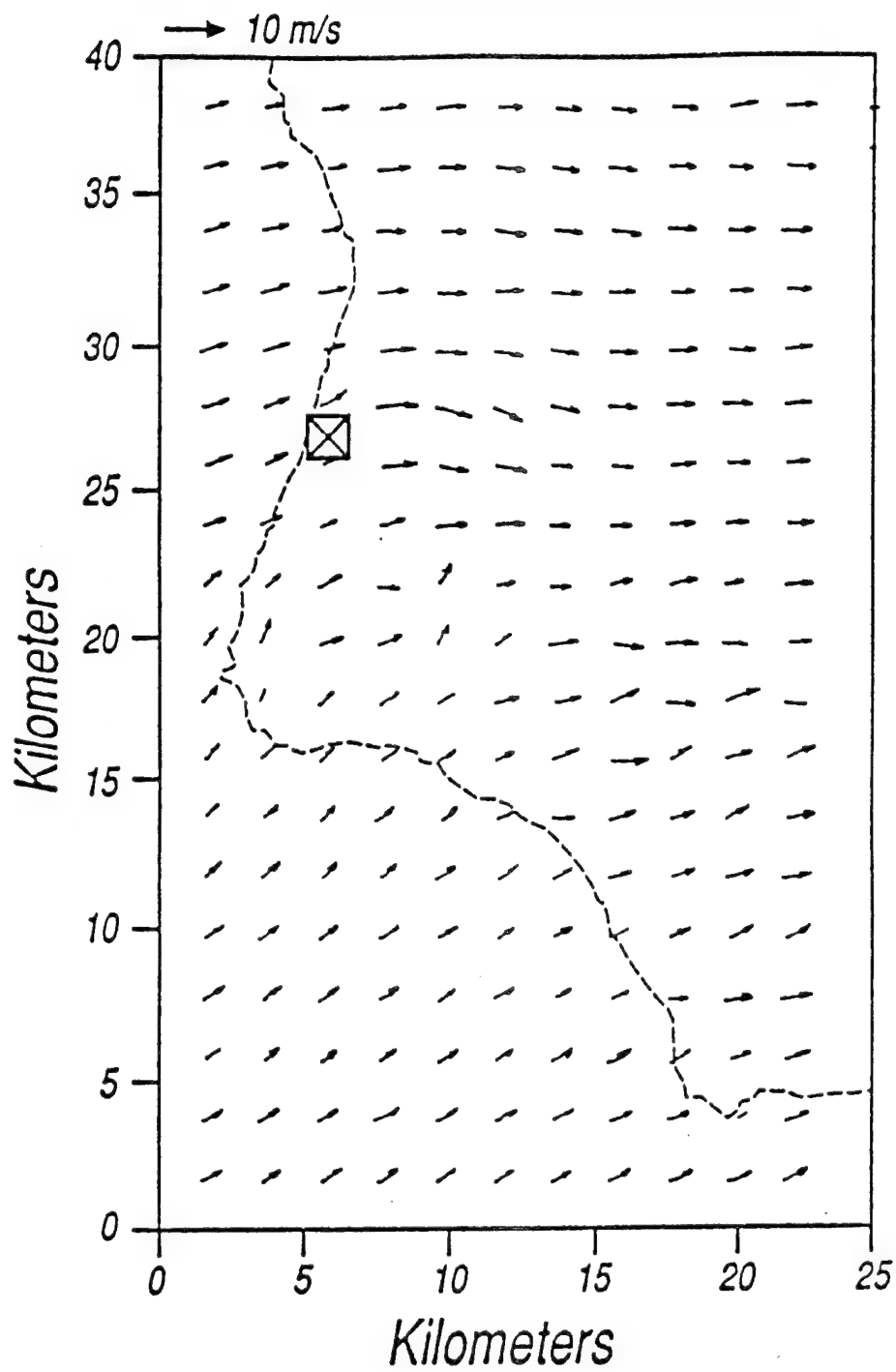


Figure 2. Modeled Horizontal Wind Vectors for the MI87 Case at 10 Meters agl from the LINCOM Diagnostic Wind Model.

Both WOCSS and LINCOM used the same tower data, and wind fields were adjusted to satisfy mass consistency. Indeed, wind distributions shown in Figures 1 and 2 are in close agreement, although LINCOM (Figure 2) produced slightly more spatial variations than WOCSS (Figure 1).

As mentioned earlier, a diagnostic wind model is no more than a scheme for simple interpolation/extrapolation of observed winds at specified grid points. For this reason, the spatial variations of wind vectors in Figures 1 and 2 are confined mainly to the regions where data are available. Mass consistency and other physical constraints used in diagnostic wind models affect the wind vectors away from the measurement sites very little, because initial wind distributions are normally determined by assuming that the influence of measurements will drop, inversely proportionally to the square of the distance from the measurement sites.

A prognostic wind model, on the other hand, is based on a set of physical equations and does not require the measurement of surface winds for forecast of wind and turbulence distributions. Observations are used to verify the predictions. Recently, Yamada (Reference 12) used a three-dimensional prognostic wind model HOTMAC, Higher Order Turbulence Model for Atmospheric Circulation, to simulate diurnal variations of wind and turbulence distributions in the Vandenberg area.

HOTMAC model results (Figure 3) generally agree with the diagnostic model results (Figures 1 and 2) in the area where wind measurements are available. Wind vectors in the prognostic model are determined from the balance between the pressure force, turbulent mixing, and Coriolis force. Therefore, prognostic models can provide wind distributions in regions where no measurements are available. HOTMAC vectors (Figure 3) are quite different from the wind fields computed by WOCSS (Figure 1) and LINCOM (Figure 2) in the areas where topographic features are prominent and no wind measurements are available. The diagnostic models do not incorporate thermal pressure forces generated by the differential heating over sloped surfaces. Therefore, the variations of wind distributions in a diagnostic wind model must be provided by the wind data that reflect wind perturbations caused by surface heterogeneity.

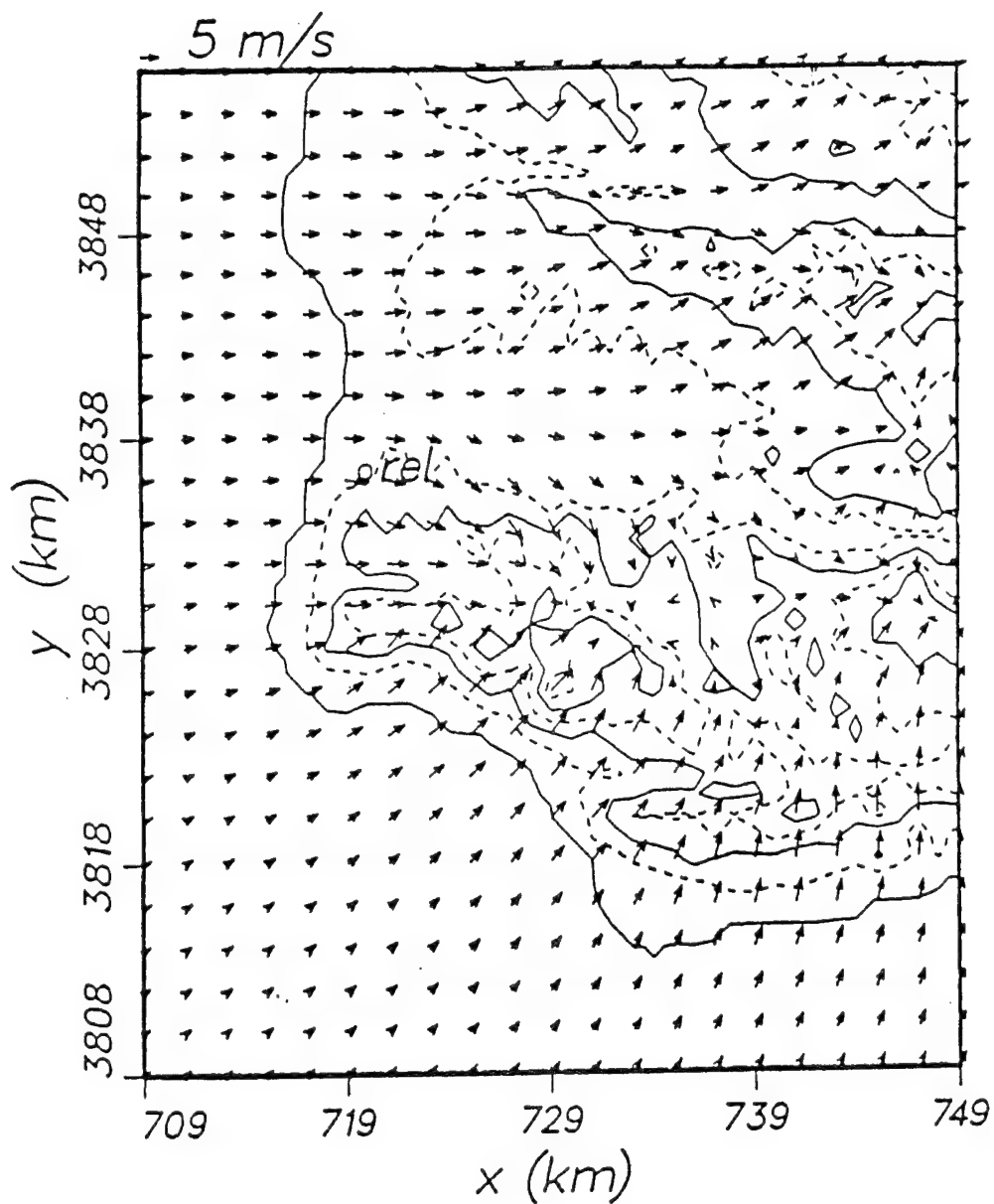


Figure 3. Modeled Horizontal Wind Vectors for the MI87 Case at 10 Meters agl from the HOTMAC Prognostic Wind Model

C. SCOPE

Section II discusses the previous study which is directly related to the present study. Section III discusses in detail the work performed for each task. Large-scale weather variations were incorporated into HOTMAC by using a technique known as four-dimensional data assimilation. Model performance was evaluated by using several statistical measures, such as mean differences, standard deviations, root-mean-square differences, and agreement measures. Section III also discusses newly added model physics, including radiation transfer in fog and clouds, precipitation microphysics, and positive and negative buoyant plumes. Improvements obtainable through the use of nested grids are also demonstrated. Conclusions and recommendations for future work are given in Section IV.

SECTION II

PREVIOUS STUDY

While employed at Los Alamos National Laboratory, the Principal Investigator (PI) of this proposal was PI of the project entitled "Three-Dimensional Modeling of Rocket Propellant Dispersion," which was sponsored by the U.S. Air Force Engineering and Services Center, Tyndall Air Force Base, FL. The purpose of that project was to demonstrate the feasibility of using a desk-top computer to operate three-dimensional hydrodynamic and diffusion models to describe the transport and dispersion of atmospheric pollutants at VAFB. To accomplish the objective, HOTMAC (Higher Order Turbulence Model for Atmospheric Circulation) and RAPTAD (Random Puff Transport And Diffusion) models were modified to run on an engineering workstation computer. The project was completed in April 1990.

HOTMAC and RAPTAD are significantly different from any AF models mentioned in Section I. HOTMAC is a prognostic model which solves a set of time-dependent physical equations, such as conservation equations of momentum, internal energy, mixing ratio of water vapor, and turbulence variables. HOTMAC forecasts three-dimensional distributions of wind speed, wind direction, temperature, and moisture. The current AF models use a single wind value or a vertical profile of wind speed and direction at a single location. Clearly, a single value or a single vertical profile of wind cannot yield realistic wind distributions for accurate transport and diffusion computations, because the terrain and meteorology in the VAFB area are highly heterogeneous. HOTMAC provided to RAPTAD both mean and turbulence variables to simulate transport and diffusion processes of airborne materials. Only a few mesoscale atmospheric models can forecast three-dimensional variations of atmospheric turbulence.

The HOTMAC/RAPTAD model results were compared with data collected during the Mountain Iron Diffusion experiments (Reference 4), which were conducted at VAFB in 1965 and 1966. HOTMAC and RAPTAD surface concentration predictions of fluorescent particles were found

to be at least as good as those obtained by diagnostic models where wind data were available, and are potentially far better where wind data are not available.

Yamada and Bunker (Reference 13) showed that it was feasible to operate HOTMAC and RAPTAD on a desk-top computer. HOTMAC took 4 hours 11 minutes and 22 hours 10 minutes CPU time, respectively, on a Sun 4/110 workstation and a MicroVax 2000 computer for a 28-hour forecast with 21 X 25 X 16 grid points. RAPTAD took 26 minutes and 3 hours 45 minutes CPU time, respectively, on a Sun 4/110 workstation and a MicroVax 2000 computer for a 20-hour simulation. Significantly faster (approximately 15 times faster than a Sun 4/110) workstations have become available since the previous project was completed. The CPU times quoted above become much shorter with these new workstations.

The increased affordability and portability of workstations have opened the door to upgrading toxic-hazard modeling capabilities for emergency response management. The HOTMAC and RAPTAD modeling system will be a useful enhancement to current emergency response management capabilities at VAFB.

To enhance the usefulness of HOTMAC and RAPTAD for operational use at VAFB, Yamada and Bunker (Reference 13) recommended the following:

1. Consider upgrading computer capabilities for emergency response applications at VAFB. MicroVax computers may not be fast enough to operate HOTMAC and RAPTAD usefully.
2. Modify HOTMAC to run continuously and store wind and turbulence data for the next 24 hours. When an emergency occurs, RAPTAD can be used immediately with the wind data stored on disk. The RAPTAD computation is much faster than that of HOTMAC, and is thus more useful in emergency situations.
3. Develop a method to integrate tower data into HOTMAC. The wind data can be used to initialize and correct the wind distribution in HOTMAC. This may be accomplished by using a dynamic initialization technique and a four-dimensional data assimilation method.

4. Develop a method to predict concentration variances which can be used to estimate uncertainties associated with predictions. A short time-averaging value is required for predicting concentration of toxic materials. Such a value normally exhibits great variations in time and space.
5. Add model physics necessary to simulate the evolution of fog formation and dissipation processes. Fog is frequently observed at VAFB and affects the heat energy balance at ground level.
6. Continue to investigate the feasibility of incorporating positive and negative source buoyancy effects in HOTMAC and RAPTAD, and test the scheme with observations.

SECTION III

WORK PERFORMED

A. TASK 1: *Develop a method to incorporate National Meteorological Center's (NMC) Limited-Area Fine Mesh (LFM) and/or Nested Grid Model (NGM) weather forecast into HOTMAC.*

Accuracy of HOTMAC and RAPTAD prediction should be greatly improved when large-scale wind variations in time and space are incorporated into HOTMAC by using NMC's forecast models LFM or NGM.

Since the horizontal scale of the study area (50 kilometers) is comparable to the horizontal grid spacing used in the NMC LFM model (100 kilometers) or NGM (30 kilometers), large-scale wind distribution used to drive HOTMAC will be considered to be spatially uniform across the horizontal domain, though variable in the vertical direction.

Our recent experience (Reference 14) indicated that incorporation of large-scale wind variations (represented by upper-air wind-sounding data) into HOTMAC improved simulations of wind speed and wind profiles over complex terrain in the Sacramento River Valley north of Sacramento, CA. We used a method referred to as Four-Dimensional Data Assimilation (4DDA), developed by Anthes (Reference 15) and Hoke and Anthes (Reference 16; Reference 17) to incorporate the large-scale wind variations into HOTMAC.

Real-time forecast data were not used in this proposal because YSA (Yamada Science and Art Corporation) could not receive NMC data in real-time. Thus, only archived data were used for development of the method.

The following sections present a brief description of HOTMAC, simulations of wind distributions from HOTMAC, and evaluations of model performance using Phase I WIND (Wind In Nonuniform Domain) data (Reference 18). Text was duplicated from a manuscript which was submitted for publication to the Monthly Weather Review (Reference 14).

1. Model

The basic equations for HOTMAC are the conservation equations for mass, momentum, potential temperature, mixing ratio of water vapor, and turbulence kinetic energy (Reference 19).

The potential temperature equation was modified (Reference 20) so that the deviation of potential temperature from that of the large-scale flow at an initial state was solved. This modification was necessary to maintain stable numerical simulations and realistically-predicted wind fields when HOTMAC was applied to simulate air flows over complex terrain with strong wind shear and temperature inversion (Reference 19). The large-scale temperature was allowed to vary with height, and assumed to be uniform in the horizontal directions.

Also referred to as a "second-moment turbulence-closure model," HOTMAC is based on a set of second-moment turbulence equations closed by assuming certain relationships between unknown higher-order turbulence moments and known lower-order moments. HOTMAC can be used under quite general conditions of flow and thermal stratification: its methods for turbulence parameterization are more advanced than those of simple eddy viscosity models. The present model, which is referred to as the level 2.5 model (Reference 21), solves a prognostic equation for turbulence kinetic energy only; the remaining second-moment turbulence variables, such as standard deviations of wind components, and heat and momentum fluxes, are solved from a set of algebraic equations.

The present model assumes hydrostatic equilibrium and uses the Boussinesq approximation. Therefore, in theory, the model applications are limited to flows where the local acceleration and advection terms in the equation of vertical motion are much smaller than the acceleration due to gravity (hydrostatic equilibrium), and temperature variations in the horizontal directions are not too large (Boussinesq approximation). This assumption is probably justified given the horizontal grid spacing of 5 kilometers used in this study. The only way to thoroughly validate these assumptions would be to repeat the simulations with a nonhydrostatic, non-Boussinesq mesoscale model and compare those results with the present results. Construction of a non-Boussinesq turbulence-closure model is complicated if not impossible.

Variations of large-scale wind distributions were incorporated into the equations of motion through a technique referred to as “nudging” or “Newtonian relaxation” (Reference 15; Reference 16). The terms $C_n(U_t - U)$ and $C_n(V_t - V)$ were added, respectively, to the equations of motion for the east-west and north-south components. C_n is the nudging coefficient, and for the present study a constant value of 5×10^{-4} was employed throughout the simulations. The three levels near the surface were not subjected to nudging. U_t and V_t are “target” wind components for the corresponding wind components U and V . U_t and V_t were computed, as in Equations (1) and (2), from the large-scale wind distributions and the geostrophic wind, assuming a horizontally homogeneous condition (Reference 20):

$$U_t = U_{obs} - \frac{f}{C_n}(V_{obs} - V_g) \quad (1)$$

$$V_t = V_{obs} + \frac{f}{C_n}(U_{obs} - U_g) \quad (2)$$

Here, U_{obs} and V_{obs} are the observed wind components, and U_g and V_g the geostrophic wind components. The formulas for U_g and V_g can be found in Yamada (Reference 22) and Yamada and Bunker (Reference 20). U_t and V_t are, in general, different from the corresponding large-scale wind components. Observed winds may be used as target winds if the Coriolis force is absent or if the observed winds are identical to the geostrophic winds. In all other cases, if only the observed winds are used in the nudging, the solutions will generally be different from the observations.

The physical meaning of the target winds from Equations (1) and (2) is that the solutions of the equations of motion with the target winds become identical to the observed winds in the absence of frictional effects. Thus, modeled winds should correspond closely to observed winds in the layers above the boundary layer, where frictional effects are negligible. In the boundary layer frictional effects are significant, due to atmospheric turbulence, and the nudging terms play relatively minor roles. To ensure that the model simulates mesoscale features, the nudging

terms were turned off at the first three vertical levels. In summary, the nudging terms force the modeled winds to match with observations in the free atmosphere, but they play relatively minor roles in the boundary layer.

Three-dimensional fields of the target wind were generated as follows: First, U_{obs} and V_{obs} were calculated from a sounding which was interpolated spatially to satisfy mass continuity. Then, U_{obs} and V_{obs} , together with U_g and V_g (computed by the formulas in Yamada (Reference 22)) were substituted into Equations (1) and (2) to obtain U_t and V_t .

Comparisons in the simulated wind fields were made by nudging to the target wind components U_t and V_t and by nudging to the observed wind components U_{obs} and V_{obs} . Nudging to the target wind components produced better agreement between simulated and observed upper winds than nudging to the observed wind components. Therefore, in the following section, the results obtained by nudging to the target wind components are shown.

Surface boundary conditions were constructed from the empirical formulas of Dyer and Hicks (Reference 23) for nondimensional wind and temperature profiles. The temperatures in the soil layers were obtained by solutions of the heat-conduction equation. Appropriate boundary conditions were the heat balance at the soil surface and specification of the soil temperature at a certain depth. The lateral boundary values were obtained by integration of the corresponding governing equations, except that variations in the horizontal directions were neglected. Parameterization of tall canopy effects on wind and radiation has been studied (Reference 24). These effects are included in the present model.

The governing equations were integrated by use of the Alternating Direction Implicit method (Reference 25). A time increment was chosen to be 90 percent of the minimum value of $\Delta x_i/U_i$, where Δx_i is a grid spacing and U_i the velocity component in the i -th direction (Courant-Freidrich-Lewy criterion). The integration time increment is also limited by the propagation speed of gravity waves, which is computed, based on the potential temperature gradients. To increase the accuracy of finite-difference approximations, mean and turbulence variables are defined at grids which are staggered in both the horizontal and vertical directions. Mean winds,

temperature, and water vapor vary most with height near the surface. To resolve these variations without introducing an excessive computational burden, nonuniform grid spacing is used in the vertical direction.

2. Evaluation of Model Performance

Visual comparisons of simulation with observation are useful. However, quantitative evaluation of model performance is also desirable, since it enables us to objectively compare one model to other models, or one simulation case to another. For the present study, continuous observations of wind direction and speed, temperature, and humidity were available throughout the 24-hour period at 21 surface stations for both the Phase I and II measurement periods, and upper-air sounding data were available every 2 hours at 5 sites.

Hourly means, standard deviations, systematic and unsystematic components of the root-mean-square differences (as well as the total root-mean-square difference), and agreement measures, were calculated for surface wind, temperature, and dew point data. No upper-air statistical comparison was made due to an insufficient amount of such data. Definitions of the statistical parameters are given below.

a. Mean

$$\bar{x} = \frac{\sum_k x(k)}{N} \quad (3)$$

where $x(k)$ is one of the meteorological variables at the k -th station, and N is the total number of stations. Means for both the simulation and the observation were calculated; for good agreement, both should be similar.

b. Standard deviation

$$\sigma = \left\{ \sum_k \frac{[x(k) - \bar{x}]^2}{N} \right\}^{\frac{1}{2}} \quad (4)$$

The standard deviation for both the simulation and the observation should also be similar for good agreement.

c. Root-mean-square differences

Use of systematic and unsystematic components of the root-mean-square differences as well as the total root-mean-square difference ($RMSD_s$, $RMSD_u$, and $RMSD$, respectively) was recommended by Willmott (Reference 26) for quantitative evaluation of model performance. Steyn and McKendry (Reference 27) used these parameters to evaluate the performance of the Colorado State University mesoscale model by Mahrer and Pielke (Reference 28; Reference 29) for a sea-breeze case over complex terrain. These parameters were used also by Ulrickson and Mass (Reference 30) for the evaluation of the above-mentioned model when used for simulation of mesoscale circulations over the Los Angeles Basin.

These parameters are defined as:

$$RMSD_s = \left[\frac{1}{N} \sum_k (x_m^*(k) - x_o(k))^2 \right]^{\frac{1}{2}} \quad (5)$$

$$RMSD_u = \left[\frac{1}{N} \sum_k (x_m^*(k) - x_m(k))^2 \right]^{\frac{1}{2}} \quad (6)$$

$$RMSD = \left[\frac{1}{N} \sum_k (x_m(k) - x_o(k))^2 \right]^{\frac{1}{2}} \quad (7)$$

where N is the number of stations (evaluation points), x_m and x_o are simulated and observed values respectively, and $x_m^* = a + bx_o$ where a and b are the parameters associated with an ordinary least squares linear regression between x_o and x_m (Reference 27).

$RMSD_s$ is an estimate not only of the offset bias of a model, but also of any linear variation in the bias of that model. $RMSD_u$ is a measure of the nonlinear discrepancy between simulation and observations (Reference 30). The definitions of systematic and unsystematic

RMSD apply to the spatial coherence of each hourly set of simulations and observations, and do not address the errors at individual sites.

d. Agreement measure

$$A = 1 - \frac{\sum_k (x_m(k) - x_o(k))^2}{\sum_k (|x_m(k) - \bar{x}_m| + |x_o(k) - \bar{x}_o|)^2} \quad (8)$$

This dimensionless index has a theoretical range of 1.0 (for perfect agreement) to 0.0 (for no agreement). This parameter was also used by Steyn and McKendry (Reference 27), and Ulrickson and Mass (Reference 30) for their studies of model evaluation.

3. Simulation of Phase I Data

HOTMAC was used for simulation of the project WIND Phase I (summer) data (Reference 18). Phase I of the field study was conducted in June and July 1985 during a weak-to-moderate marine incursion regime. The main meteorological events during the Phase I observation period were the diurnal variation of the surface wind fields, upslope winds during the day and downslope winds during the night. Simulation of this diurnal change — its timing, strength, the structure of the winds, and the accompanying changes in temperature near the surface — was the main focus of this study.¹

Simulation results were compared temporally and spatially with both surface and upper-air observations. Statistical comparisons between simulation and observation were also made. The results indicated good simulation capabilities of the model.

a. Model Domain

The study area was centered in the Sacramento River Valley north of Sacramento, CA, extending eastward up the slopes of the Sierra Nevada and westward to the slopes of the Coast Range. Latitude and longitude of the southwestern corner of the domain for the simulation

¹ Pearce, R. (Personal communication), 1992.

(Figure 4) were 39.63 N and 122.99 W. Meteorological variables were calculated at 40 X 40 grid points with a horizontal grid spacing of 5 kilometers. In the figure, characters represent the locations of surface stations. Upper-air soundings were taken near BC3(01), C7(02), S8(03), B2(04), and S3(05). Here, numbers in parentheses represent upper-air stations.

b. Initial Values

A meteorological data set for the 24-hour period starting at 0900 LT of Julian day 178 (27 June) was used in this study, this day being characterized as a typical summer day. The most common flow regime in the Sacramento River Valley during the summer is southerly (upslope) flow during the day and northerly (downslope) flow at night. The southerly flow is consistent with a weak marine incursion, which results when wind that blows onshore from the San Francisco Bay area (more than 200 kilometers away) moves inland and becomes diverted north and south by the Sierra Nevada along the Sacramento River Valley.

An initial wind profile at Station 3 was first constructed by assuming a logarithmic variation with $u_* = 0.2$ m/s and $z_o = 0.1$ m from the ground up to the level where the wind speed reaches an ambient value of 5 m/s. Initial wind profiles at other grid locations were obtained by multiplying the station 3 winds by $(z - z_g)/(H - z_g)$ to satisfy mass continuity approximately, and wind directions were initially from the SW (210 degrees) throughout the atmosphere. The vertical profile of potential temperature was initialized based on an upper-air sounding taken at station 3 at 0900 LT of day 178, and initial potential temperatures were assumed to be uniform in the horizontal directions. Initial values of water vapor were also based on observation, whereas the turbulence kinetic energy and length scale were initialized using the initial wind and temperature profiles, and the relationships determined by the Level 2 turbulence-closure model (Reference 31). The Level 2 model assumes a balance between the production and dissipation terms in the turbulence kinetic energy equation.

The simulation commenced at 0900 LT of day 178 and lasted until 0900 of day 179. However, model calculations were begun 4 hours before the start of the actual simulation to produce an initial adjustment. At 1 hour before the start of simulation, the observed wind data at

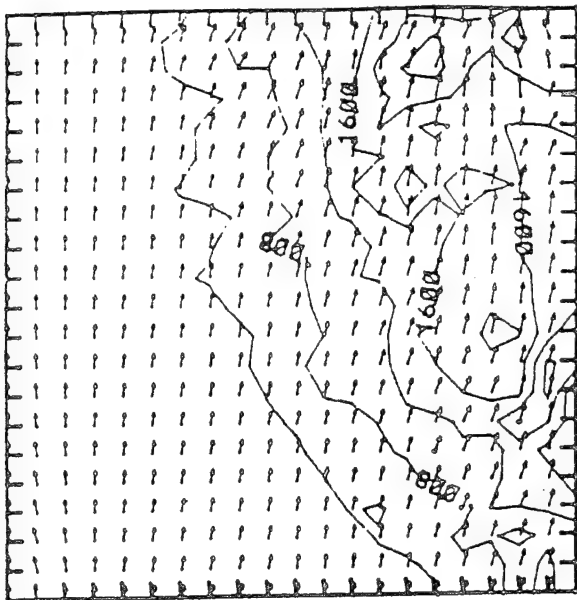
0900 were read in and model winds began nudging toward target winds, as given in Equations (1) and (2).

c. Surface Meteorological Parameters

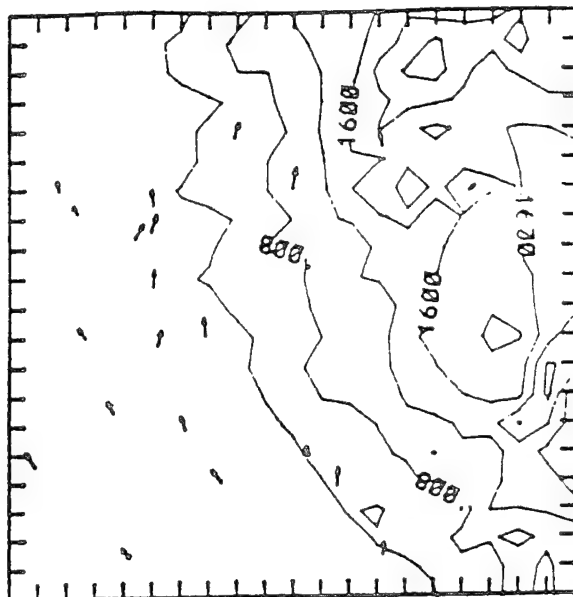
(1) Horizontal Wind Vector Fields. Model calculations were made over the area of 200 X 200 kilometers as shown in Figure 4. However, to make visual comparison easy, simulated horizontal wind vectors were plotted only for the area of 100 X 100 kilometers that contains all of the surface and upper-air stations. Figures 5 and 6 show surface (10-meter level) wind vector fields at 1500 LT of day 178, and 0500 LT of day 179. In these figures, (A) represents the simulated wind field with nudging to the target winds, (B) the observed winds, (C) the target wind field, and (D) the simulated wind field without nudging. An arrow with a unit grid distance represents a wind vector of 10 m/sec. The four fields allow us to examine the influences of nudging. It can be seen in both figures that nudging to the target wind fields has significantly influenced the simulated wind fields. In Figure 5, nudging to the target wind field has produced southerly flow throughout the model domain, whereas the simulated wind field without nudging was southwesterly. In Figure 6, the effects of nudging to the target wind field were to shift the wind direction from easterly along the Sierra Nevada to northeasterly, and to generate northerly flow in the Sacramento River Valley. It was also noted, from the comparisons between (A) and (D), that the simulations with nudging to the target wind fields produced smoother wind fields throughout the domain than those without nudging.

Upslope winds during the day (Figure 5(A)) and downslope winds during the night (Figure 6(A)) can be detected along the foothills of the Sierra Nevada. The observations show that during the day, wind vector distributions were relatively uniform, but during the night, wind vectors varied considerably in space, because the surface layer was decoupled from the atmosphere above, and locally generated forces dominated the wind distributions. These local forces appeared to be due to subgrid scale phenomena. Neither simulations with nor without nudging produced the large variations of wind distributions detected in the observations.

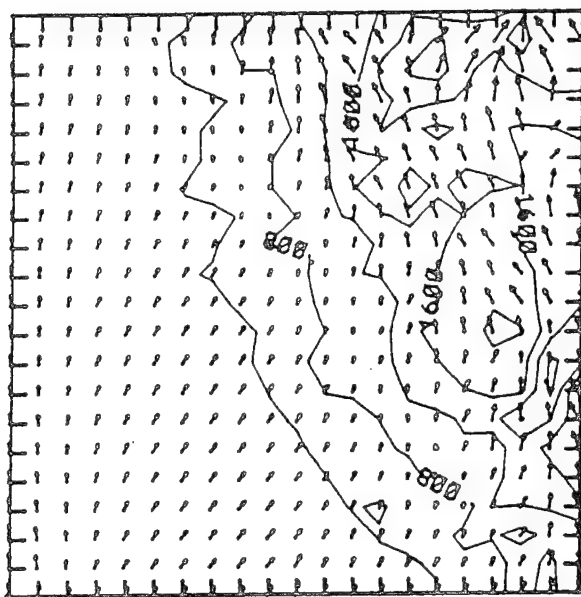
(2) Time Series Comparisons of Station Data. The evolution of the wind direction and



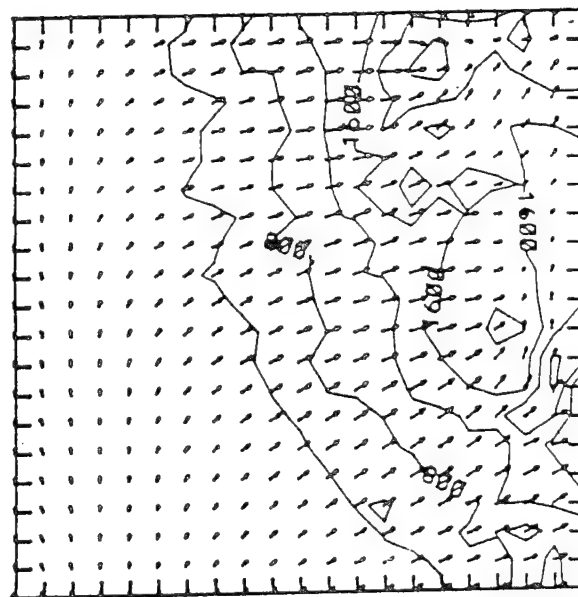
(A)



(B)

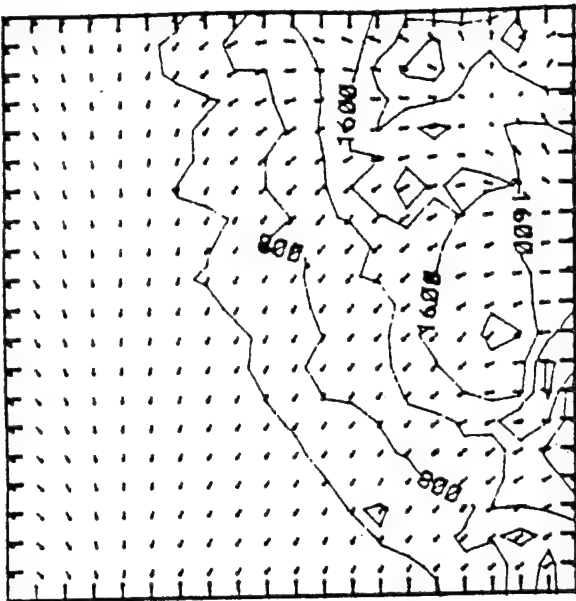


(C)

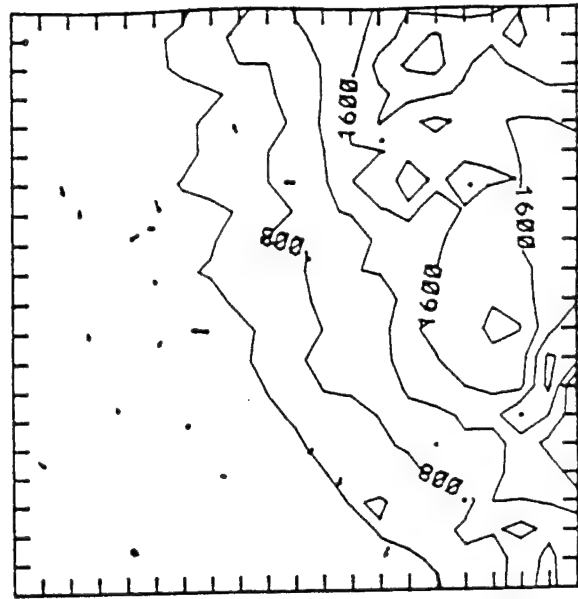


(D)

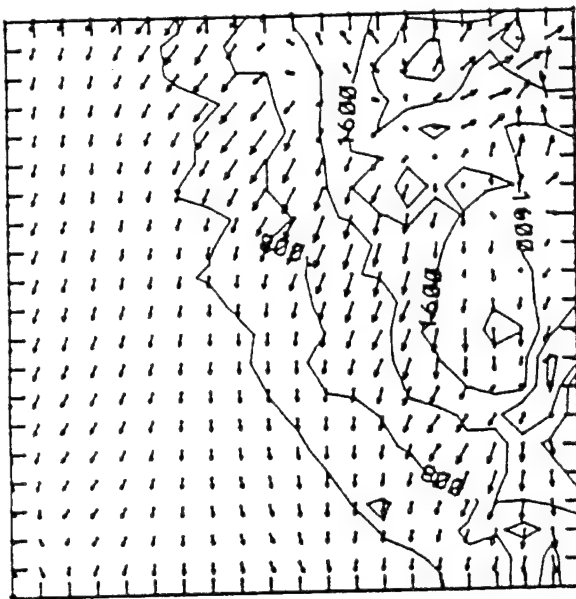
Figure 5. Surface (10-Meter Level) Horizontal Wind Vector Distributions for Phase I at 1500 LT of Day 178. (A) the Simulation With Nudging, (B) Observations, (C) the Target Wind Field, and (D) the Simulation Without Nudging. An Arrow With a Unit Grid Distance Represents 10 m/sec.



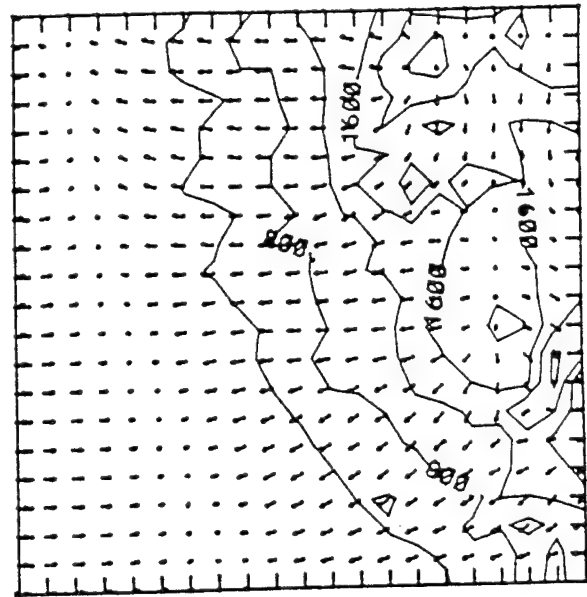
(A)



(B)



(C)



(D)

Figure 6. Same as Figure 5 except at 0500 LT of Day 179.

speed at the 10-meter level, and of the temperature and dew point at the 2-meter level are given in Figures 7(A), (B), (C), and (D) for four representative stations, S2, S10, S14, and C3. These figures show the results of simulation with nudging to the target wind. In these figures, hourly values of observations are plotted with circles, and simulations by solid lines.

Station S2 was located in the valley. The wind direction shift, from south early during the daytime to the north early during the nighttime, was simulated well. The diurnal variation of the modeled wind speed is also in good agreement with the observations.

Station S10, which was located near the foothills of the Sierra Nevada, showed disagreement between simulated and observed wind directions after sunset. Whereas the observed wind direction was predominantly northwesterly, the simulated direction was northeasterly. Observed wind speeds during the nocturnal period were approximately 1 m/s, and at such low speeds determination of wind direction is difficult and may contain large errors.

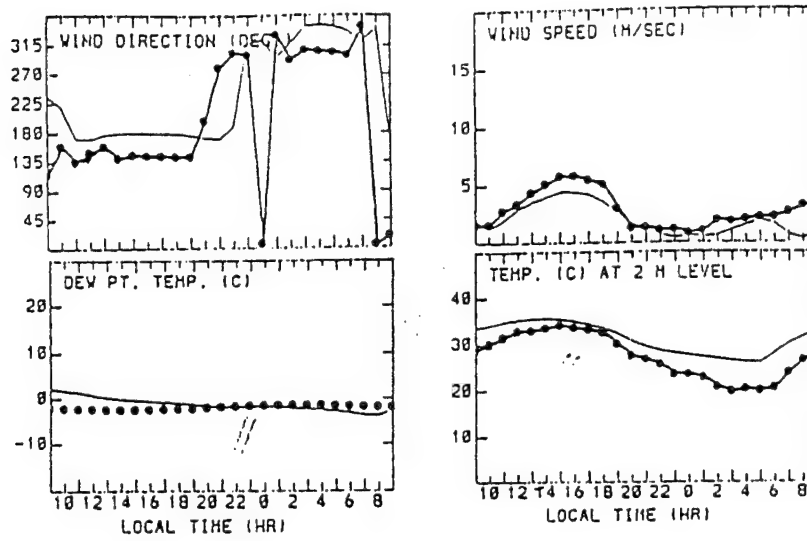
At Station S14, which was located on the western slope of the mountain range, the observed wind direction changed gradually from southeast to east, but the simulated direction showed a sudden shift of wind direction from south to east after sunset. Wind speeds did not agree well during the day.

At Station C3, the observed wind direction changed from southwest early in the day to northwest early at night, whereas the simulated wind direction stayed southerly throughout the 24-hour period. The wind speeds also did not agree well. At this station, the observed wind speeds stayed very low during the night; the model failed to simulate these low wind speeds.

The simulated temperatures agreed well with observations during the day, but during the night the differences between simulated and observed temperatures became significant. Particularly at C3, the model failed to simulate the nocturnal temperature drop. Station C3 was located in a meadow which was surrounded by high mountains. This is clearly an example of subgrid scale phenomena, which the model could not resolve with a 5-kilometer grid spacing. In general, the diurnal ranges of simulated temperature were smaller than those observed.

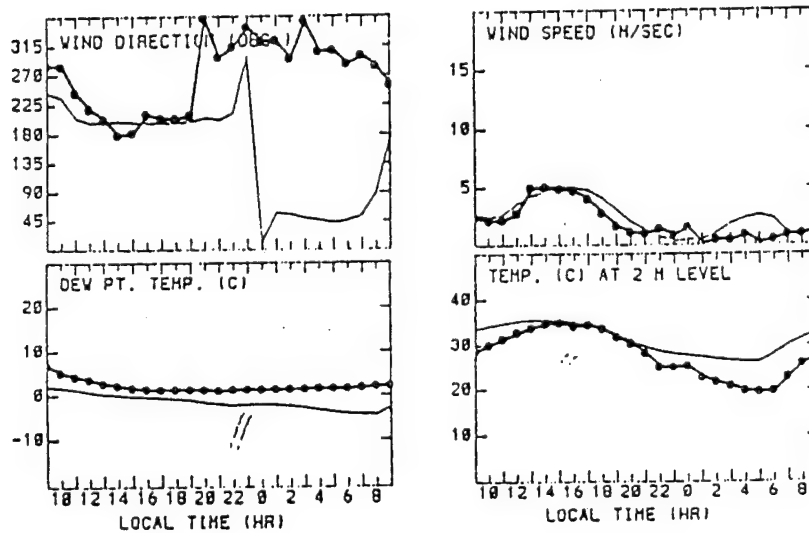
Throughout the 24-hour period, the dew points remained low, as can be seen from

STATION = S2



(A)

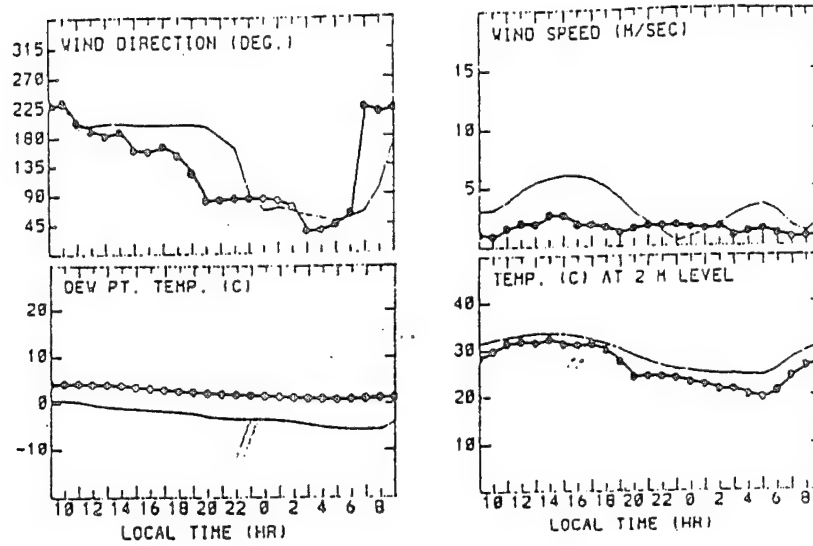
STATION = S10



(B)

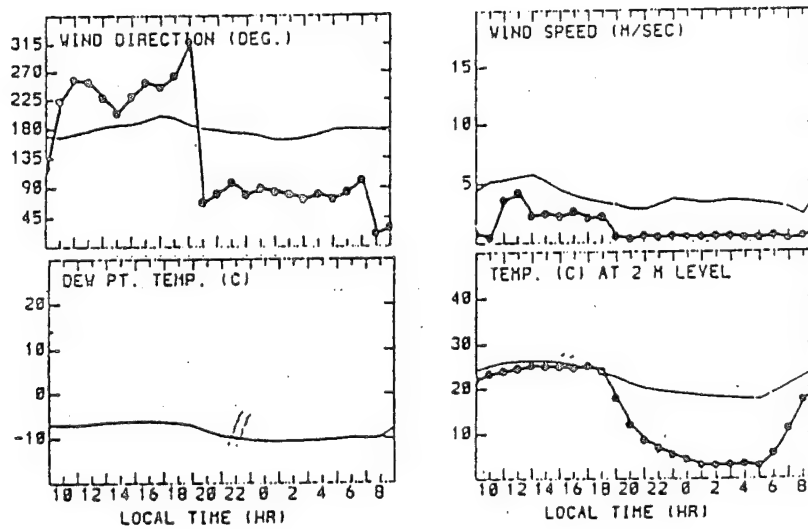
Figure 7. Time Evolutions of Surface Meteorological Variables During the 24-Hour Period of the Project WIND Phase I, at (A) Station S2, (B) Station S10, (C) Station S14, and (D) Station C3. (- Simulation, and o Observation) (Continued)

STATION = S14



(C)

STATION = C3



(D)

Figure 7. Time Evolutions of Surface Meteorological Variables During the 24-Hour Period of the Project WIND Phase I, at (A) Station S2, (B) Station S10, (C) Station S14, and (D) Station C3. (- Simulation, and o Observation) (Concluded)

Figures 7(A), (B), and (C). There was no dew-point observation available at C3.

(3) Statistical Parameters. Using the data from 21 surface observation sites, mean wind directions and speeds, in addition to standard deviation of speed, were calculated hourly for the simulation (solid line) and observation (circles) as shown in Figure 8(A). Also shown are hourly RMSD, RMSD_s and RMSD_u , and agreement measures of wind speeds. Mean wind direction was calculated from the means of the horizontal wind components.

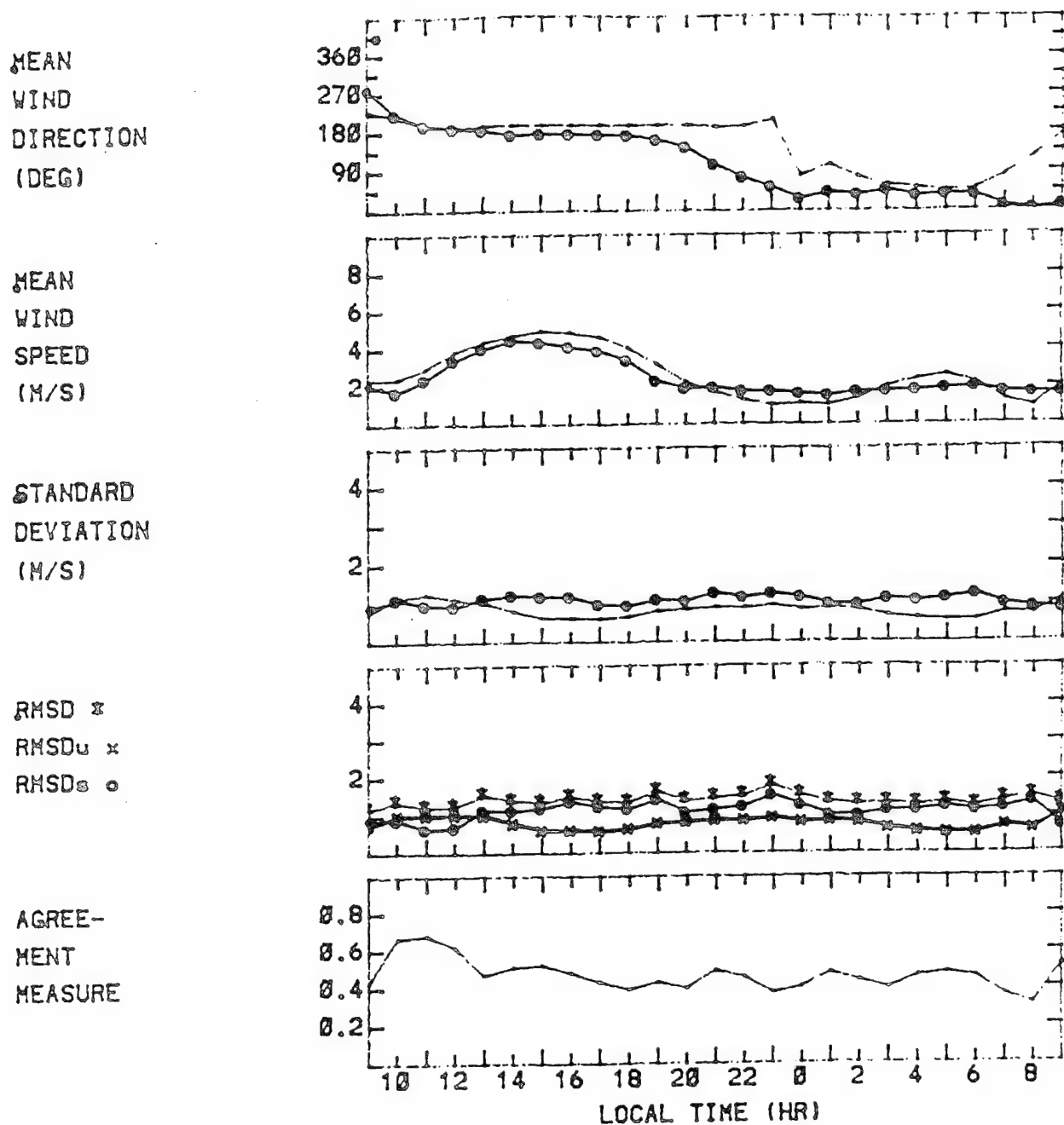
The top two portions of Figure 8(A) show that the overall patterns of the observed and simulated surface wind fields agreed well, except for several hours after sunset.

Mean directions of observed wind were from the southwest during the day, shifted gradually to the north after sunset, and stayed northeast during the night. The simulated mean wind directions agreed well with the observed directions during the day, but the shifting to the north was delayed for several hours in the simulation, and after midnight stayed north rather than northeast. Simulated and observed mean wind speeds agreed well throughout the 24-hour period.

The standard deviations of the observed and simulated wind speeds were comparable throughout the simulation period. The evolution of RMSD and its two components shows no diurnal trend, and both components of RMSD are of roughly equal magnitude. The unsystematic component, RMSD_u , represents the irreducible deviation between observed and simulated results, while the systematic component represents trend-like differences between observed and simulated fields (Reference 27).

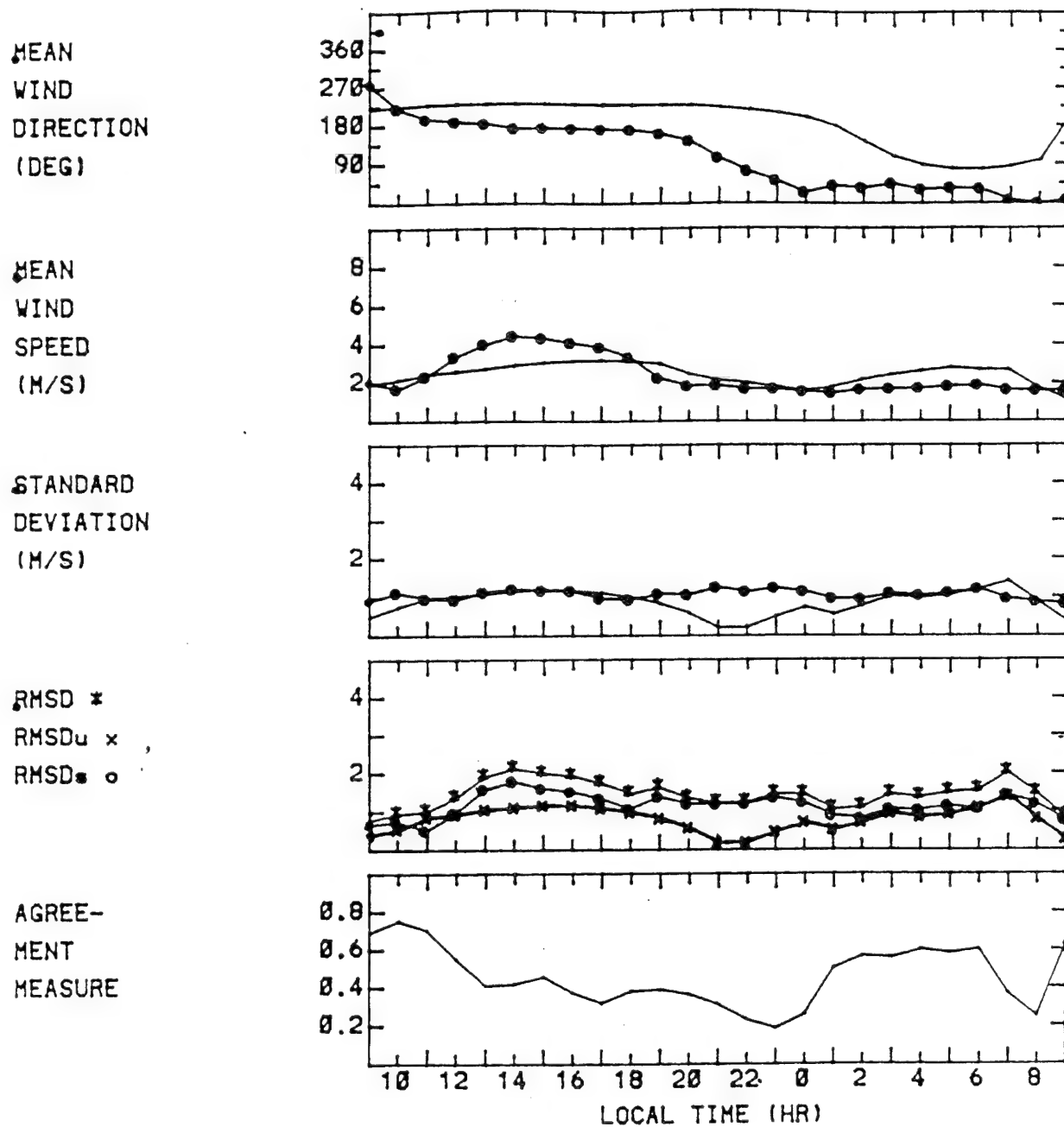
The greatest agreement measure (0.65) was obtained at 1100 LT of Day 178, but after 1200 LT it remained near 0.5, without any systematic trend.

Similar statistical calculations were conducted for the simulated wind fields without nudging and for the persistence wind field, and the results are shown in Figure 8(B) and (C). Here, the persistence wind field was the observed 10-meter level wind field at 0900 LT of Day 178, when the simulation was initialized. From the comparisons between Figures 8(A), (B), and (C), the following can be inferred:



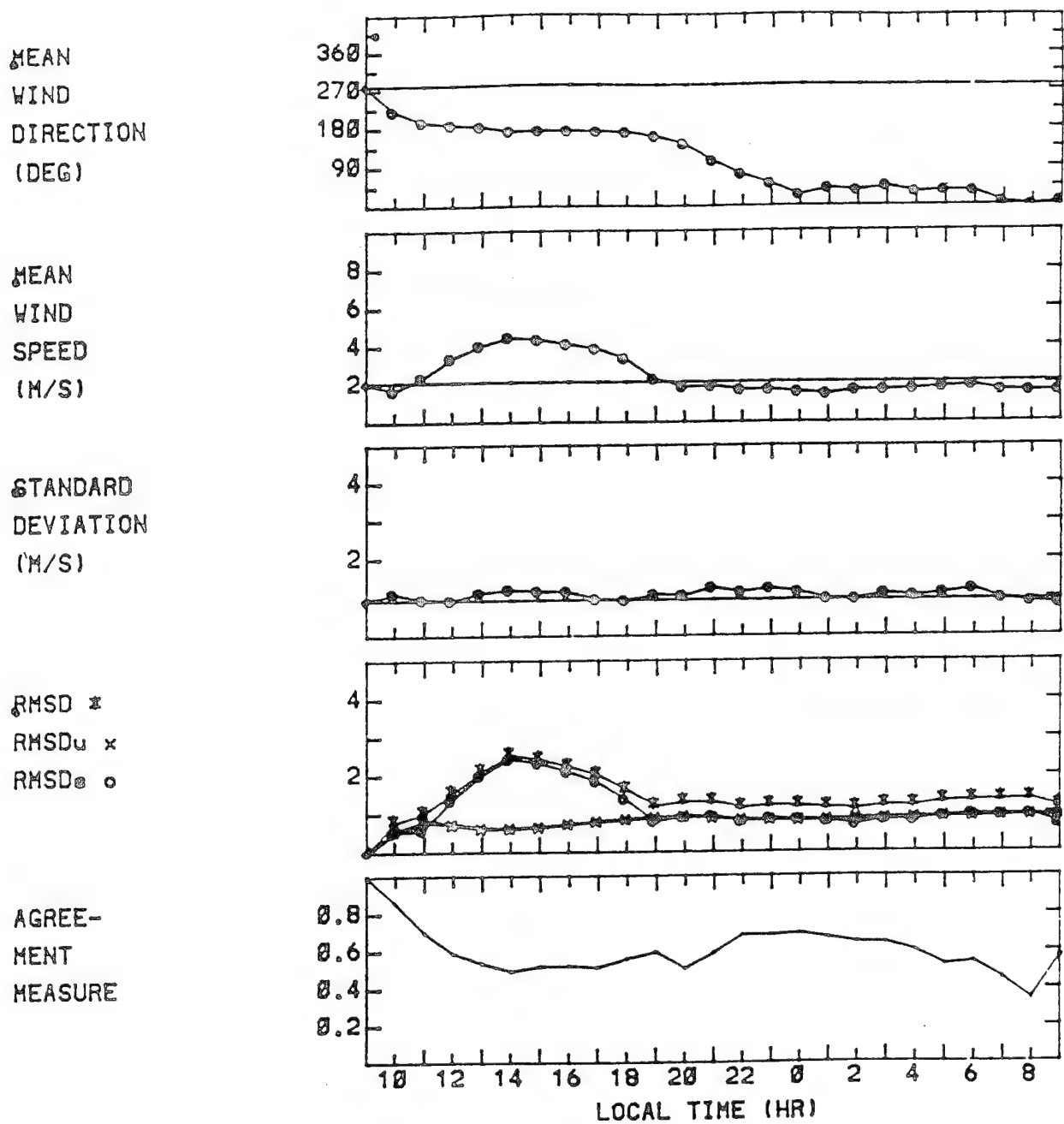
(A)

Figure 8. Time Evolutions of Statistical Parameters of Surface (10-Meter Level) Wind Speed and Direction for 24-Hour Period of Phase I for the Simulation with Nudging to the Target Winds. From the Top, Mean Wind Direction (— Simulation, and o Observation), Mean Wind Speed (— Simulation, and o Observation), Standard Deviation of Wind Speed (— Simulation, and o Observation), Root-Mean-Square Differences (* RMSD, x RMSD_u, and o RMSD_s), and Agreement Measure of Wind Speed. (A) Winds were Nudged to the Target Winds, (B) No Nudging was applied, and (C) Persistence Winds were used. (Continued)



(B)

Figure 8. Time Evolutions of Statistical Parameters of Surface (10-Meter Level) Wind Speed and Direction for 24-Hour Period of Phase I for the Simulation with Nudging to the Target Winds. From the Top, Mean Wind Direction (— Simulation, and o Observation), Mean Wind Speed (— Simulation, and o Observation), Standard Deviation of Wind Speed (— Simulation, and o Observation), Root-Mean-Square Differences (* RMSD, x RMSD_u, and o RMSD_s), and Agreement Measure of Wind Speed. (A) Winds were Nudged to the Target Winds, (B) No Nudging was applied, and (C) Persistence Winds were used. (Continued)



(C)

Figure 8. Time Evolutions of Statistical Parameters of Surface (10-Meter Level) Wind Speed and Direction for 24-Hour Period of Phase I for the Simulation with Nudging to the Target Winds. From the Top, Mean Wind Direction (— Simulation, and o Observation), Mean Wind Speed (— Simulation, and o Observation), Standard Deviation of Wind Speed (— Simulation, and o Observation), Root-Mean-Square Differences (* RMSD, x RMSD_u, and o RMSD_s), and Agreement Measure of Wind Speed. (A) Winds were Nudged to the Target Winds, (B) No Nudging was applied, and (C) Persistence Winds were used. (Concluded)

- (1) The simulation with nudging to the target winds resulted in better agreements in mean wind directions and speeds than the simulation without nudging or the persistence.
- (2) The standard deviations and the RMSDs of the three different wind fields were of similar magnitudes.
- (3) The agreement measures of wind speed calculated for the persistence wind were the greatest among the three different wind fields.

Thus, an evaluation of model performance should not be based on a single statistical parameter. The use of an increased number of observation sites, distributed evenly over the model domain, would yield a better statistical evaluation.

Mean, standard deviation, RMSD and agreement measure of temperature at the 2-meter level were also calculated hourly as shown in Figure 9. Good agreement existed between the simulations and observations during the day, but during the night there were noticeable differences between the observed and simulated fields. The diurnal variation of the simulated surface temperature was much smaller than that of the observed, resulting in poorer agreement during the night than during the day. Smaller variations in the simulated temperature field than those of the observed temperature field resulted in large values of RMSDs during the nocturnal period. Surface temperature is dependent on many physical parameters, including surface vegetation cover and the thermal conductivity of the soil. However, in the present study, a bare surface condition and a constant thermal conductivity were assumed throughout the model domain. The incorporation of locally-dependent surface characteristics might have improved the prediction of surface temperature.

Temperature fields of the simulation without nudging yielded values of the statistical parameters very similar to those with nudging (the results are not shown).

d. Upper-Air Variables

To compare upper-air variables at certain levels, the simulated and observed vertical profiles were expressed by bi-cubic spline curves. Figure 10 shows the evolution of

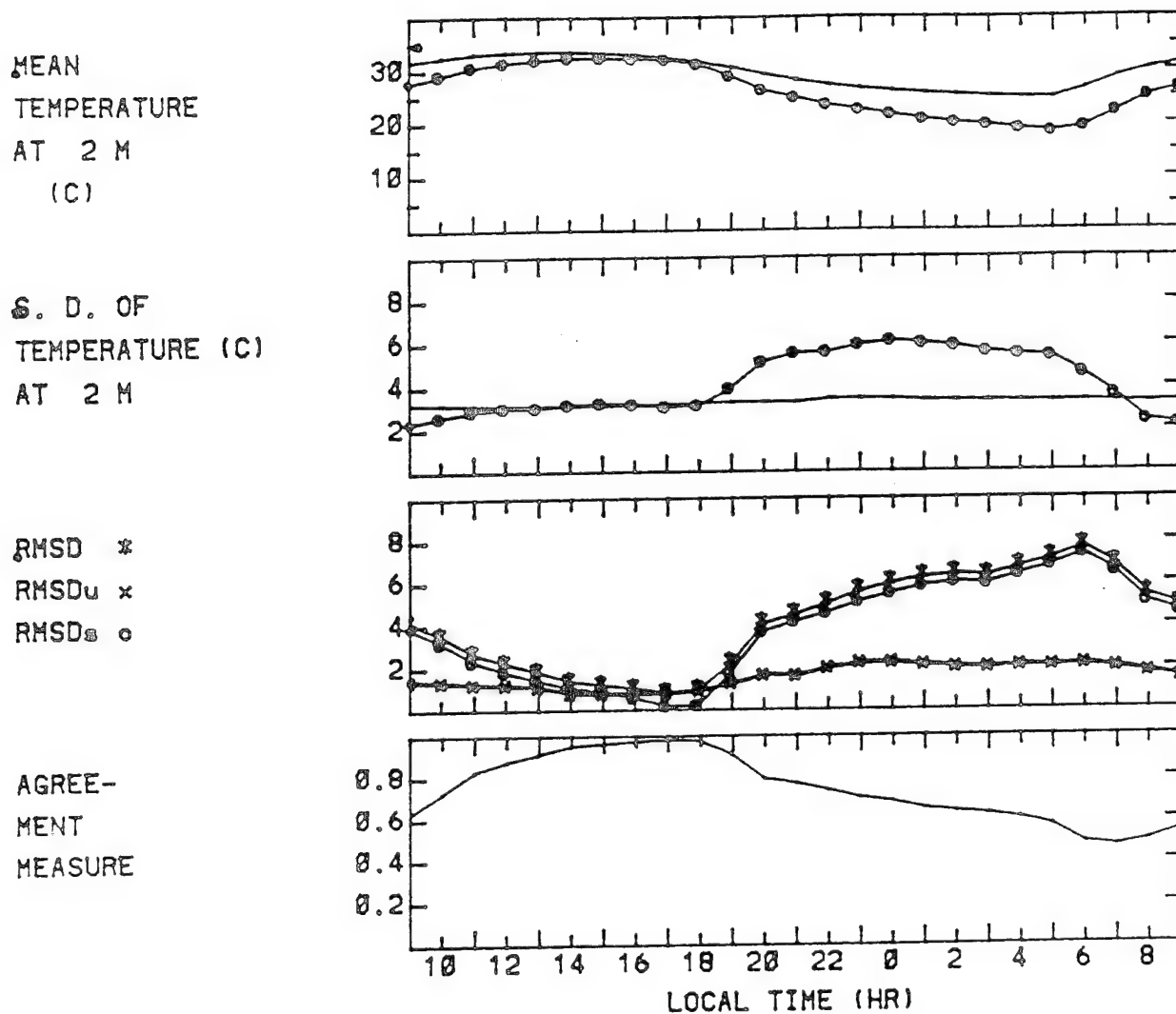


Figure 9. Time Evolutions of Statistical Parameters of Surface (2-Meter Level) Temperature. From the Top, Mean (— Simulation, and o Observation), Standard Deviations (— Simulation, and o Observation), Root-Mean-Square Differences (*RMSD, x RMSD_u, and o RMSD_s), and Agreement Measure.

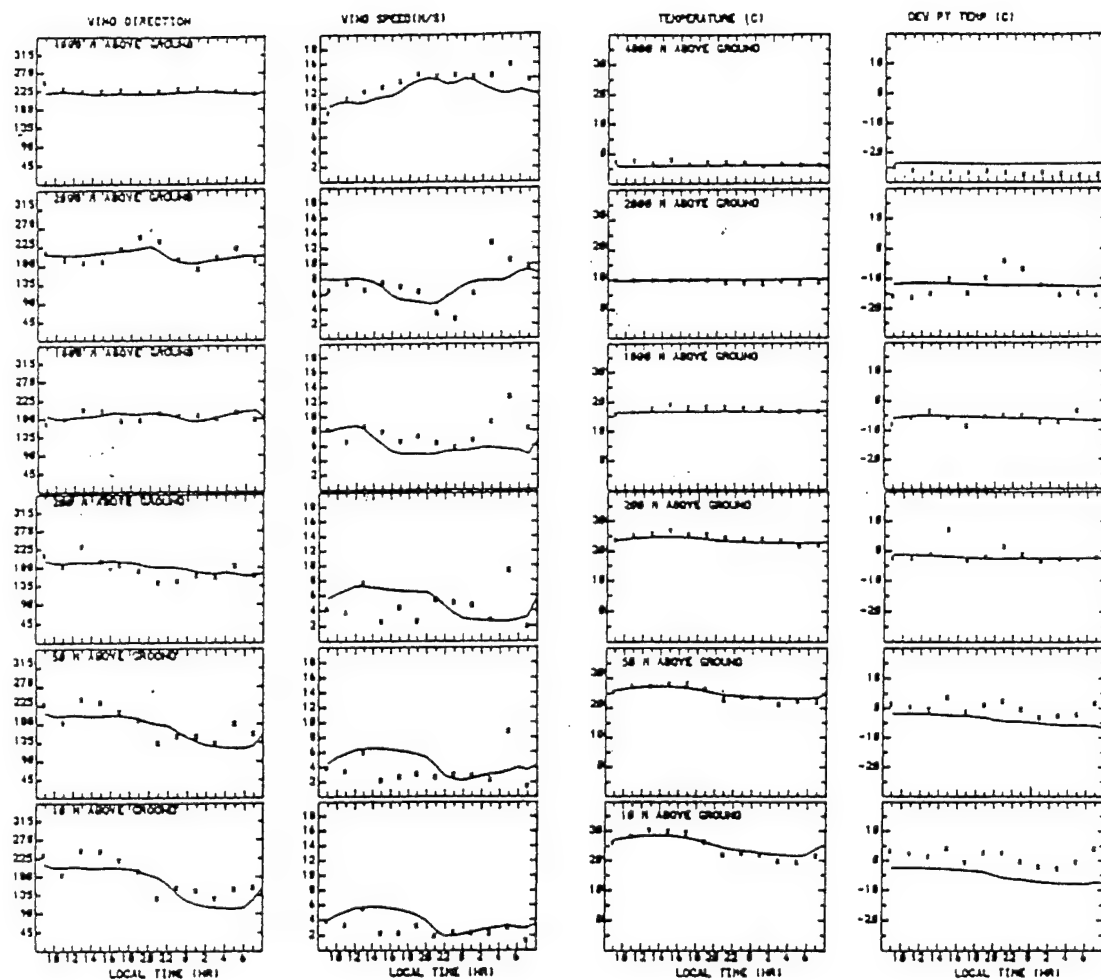


Figure 10. Time Evolution of Wind Direction, Wind Speed, Temperature and Dew Points at Different Heights (agl) at Upper-Air Station 1 during the 24-Hour period of Phase I (- Simulation, and * Observation).

upper-air variables (wind direction and wind speed, temperature, and dew point) at six different height levels (4000, 2000, 1000, 200, 50, and 10 meters agl) for Station 1. Note that the upper-air data taken at Station 3 were assimilated into the model, and that Station 1 was located about 30 kilometers east of Station 3 on the western slope of the Sierra Nevada.

The agreement between model and observation was excellent throughout the simulation at all levels, as seen in these figures, and the effects of diurnal heating and cooling were clearly recognized at the lower levels. Although temperatures and dew points in the layers above 200 meters stayed almost constant throughout the 24-hour period, wind directions and speeds showed some variation.

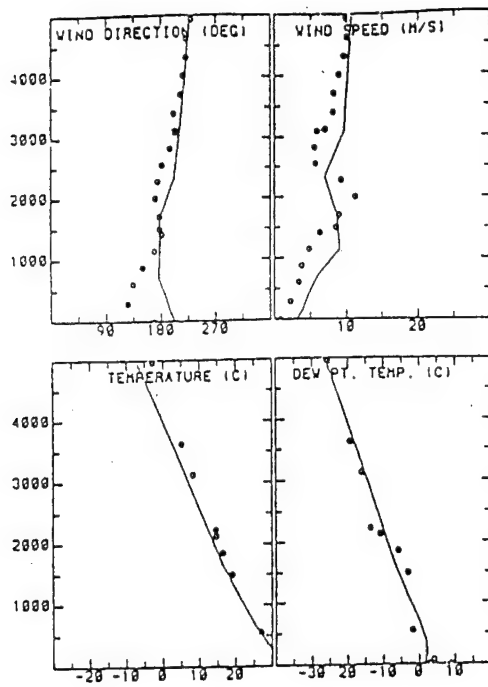
Vertical distributions of wind direction and wind speed, temperature, and dew point at 1100 and 1700 LT of Day 178, and 0100 and 0700 LT of Day 179 at Station 4 are shown in Figure 11. In Figure 11, simulations are plotted by solid lines and observations by circles. Excellent agreement in vertical distributions of wind speed and direction, temperature and dew point were obtained throughout the simulation, and good agreements were also obtained at other stations. As noted previously, no nudging was performed to the temperature and mixing ratio equations.

e. Summary

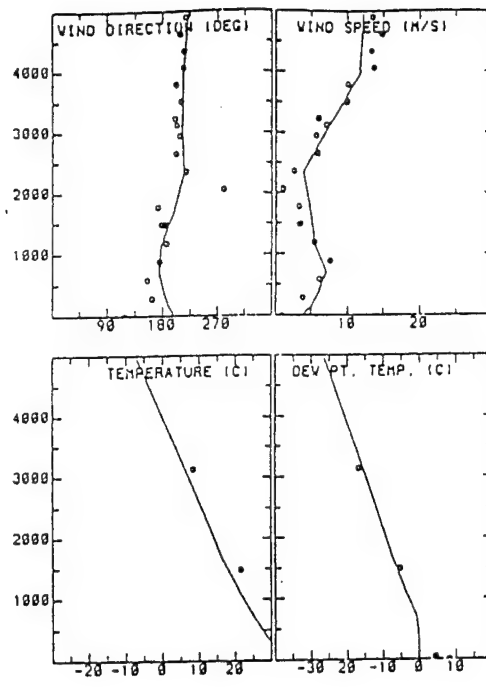
A three-dimensional mesoscale model, HOTMAC, was used to simulate the project WIND Phase I data. The nudging method in which horizontal wind components were nudged to the target wind components defined by Equations (1) and (2) was used. The advantage of nudging to the target winds over nudging to the observed winds was illustrated.

Phase I was characterized by typical summer anticyclonic conditions over the Sacramento River Valley in northern California. Southerly flow (upslope wind) during the day and northerly flow (downslope wind) at night were the characteristic flow patterns.

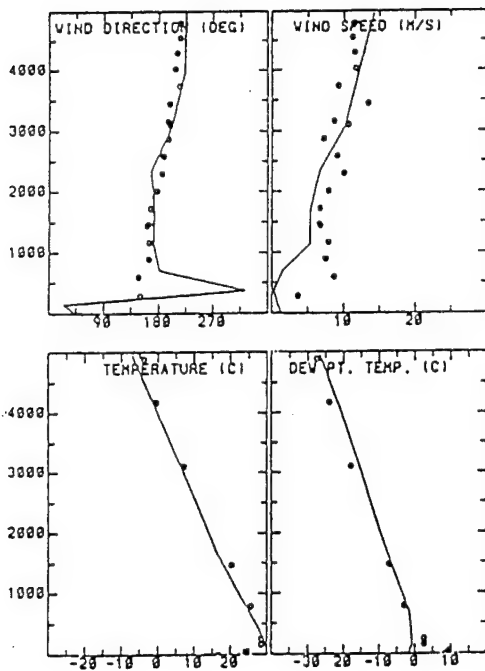
Comparisons between observations and simulations of the wind directions and speed, temperature, and dew point showed fairly good agreement, both spatially and temporally, throughout entire 24-hour periods. Thus, a single station sounding could be used to represent



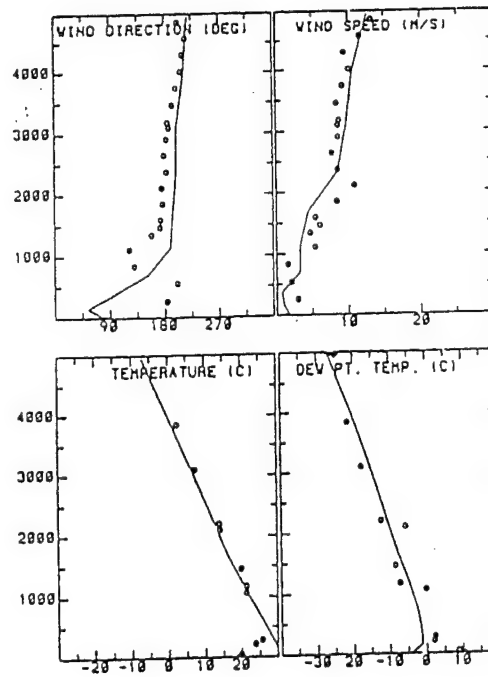
(A)



(B)



(C)



(D)

Figure 11. Vertical Distributions of Wind Direction and Speed, Temperature and Dew Point at Station 4 for Phase I. (A) 1100 LT, Day 178, (B) 1700 LT, Day 178, (C) 0100 LT, Day 179, (D) 0700 LT, Day 179 (- Simulation, and o Observation).

large-scale meteorological conditions over the model domain fairly well. However, if the area were under strong synoptic influences, the present method should not be applied, and synoptic-scale weather variations should be incorporated into a mesoscale model by specifying time-dependent lateral boundary conditions or by nesting a mesoscale model into a large-scale model.

Statistical parameters, including the mean and standard deviation of both the observed and simulated variables, the systematic and unsystematic components of the root-mean-square differences as well as the total root-mean-square difference (RMSD_s , RMSD_u , and RMSD , respectively), and the agreement measures were calculated hourly using the surface station data. These statistical parameters were calculated for three different wind fields simulated by nudging to the target winds, with no nudging, and with persistence. The wind fields obtained by nudging to target winds yielded better agreement in wind direction and speed when compared to the two other wind fields. However, the magnitudes of the standard deviation and RMSD were comparable among the three wind fields. Agreement measures of wind speed using the persistence winds were greater than those obtained from the two other wind fields. Hence, model performance should be evaluated carefully, by several different means.

B. TASK 2: *Develop a method to restart HOTMAC prediction and maintain on disk the wind and turbulence forecast data for the next 24 hours.*

A complex scheme was developed to operate HOTMAC and RAPTAD interactively. HOTMAC runs continuously and always maintains 24-hour forecast data. The interactive scheme dictates that as soon as RAPTAD starts computation, HOTMAC halts its forecasting. RAPTAD displays an hourly surface-concentration distribution plot on the screen as soon as one hourly computation is completed.

HOTMAC produces 24 hourly files, **hot01** through **hot24**. Once a 24-hour forecast is completed and the forecast data are written to a disk, HOTMAC “sleeps” until the next computation time. HOTMAC “wakes up” at the clock hour and begins to advance the forecast one hour. At the end of the one hour forecast, files are renamed: **hot02** becomes **hot01**, **hot03**

becomes **hot02**, and so on. The newest forecast is written as **hot24**, so that forecast data for the next 24 hours are always available.

RAPTAD reads HOTMAC output files **hotxx**, where wind speed, wind direction, temperature, and turbulence forecast data are stored. Graphics program **hotplt** produces graphics for vertical profiles of wind, temperature, and turbulence.

If the continuous operation of HOTMAC is interrupted (for maintenance, or by a power failure or mistakes), HOTMAC may be restarted by using one of the **hotxx** files. The restart time may be specified in input file **hotinp2**. The restart parameter may be set to zero if reinitialization is desired.

In addition to using the default mode's 24-hour forecast, the user can extend the range of the forecast period, up to 48 hours, for planning operations.

C. TASK 3: *Develop a method to combine upper-air wind-sounding and tower data taken at VAFB with HOTMAC forecast winds so that RAPTAD can use the composite (forecast and observed) winds.*

Winds measured by upper-air soundings and at towers were combined with the winds forecasted by HOTMAC. A simple $1/r^2$ weighting method was used to compute the wind at a puff center. First, we computed wind at a puff center based on the winds measured at towers. For example, Figures 12 through 16 show wind vectors at tower locations (with numbers) and those extrapolated for puff centers (without numbers) at different hours. Tower winds show considerable variation in space, but winds at puff centers are relatively uniform, because variations of tower winds are minimized by averaging. These wind distributions are similar to those generated by diagnostic wind models where winds are adjusted to satisfy the mass continuity equation.

The winds at puff centers (obtained from tower winds) were then combined with winds computed by HOTMAC. Figures 17-20 show examples of composed wind vectors at puff centers. Tower winds are again indicated by wind vectors with numbers. Tower winds are weighted based

WIND VECTORS VAFB 11193 1110 12ft

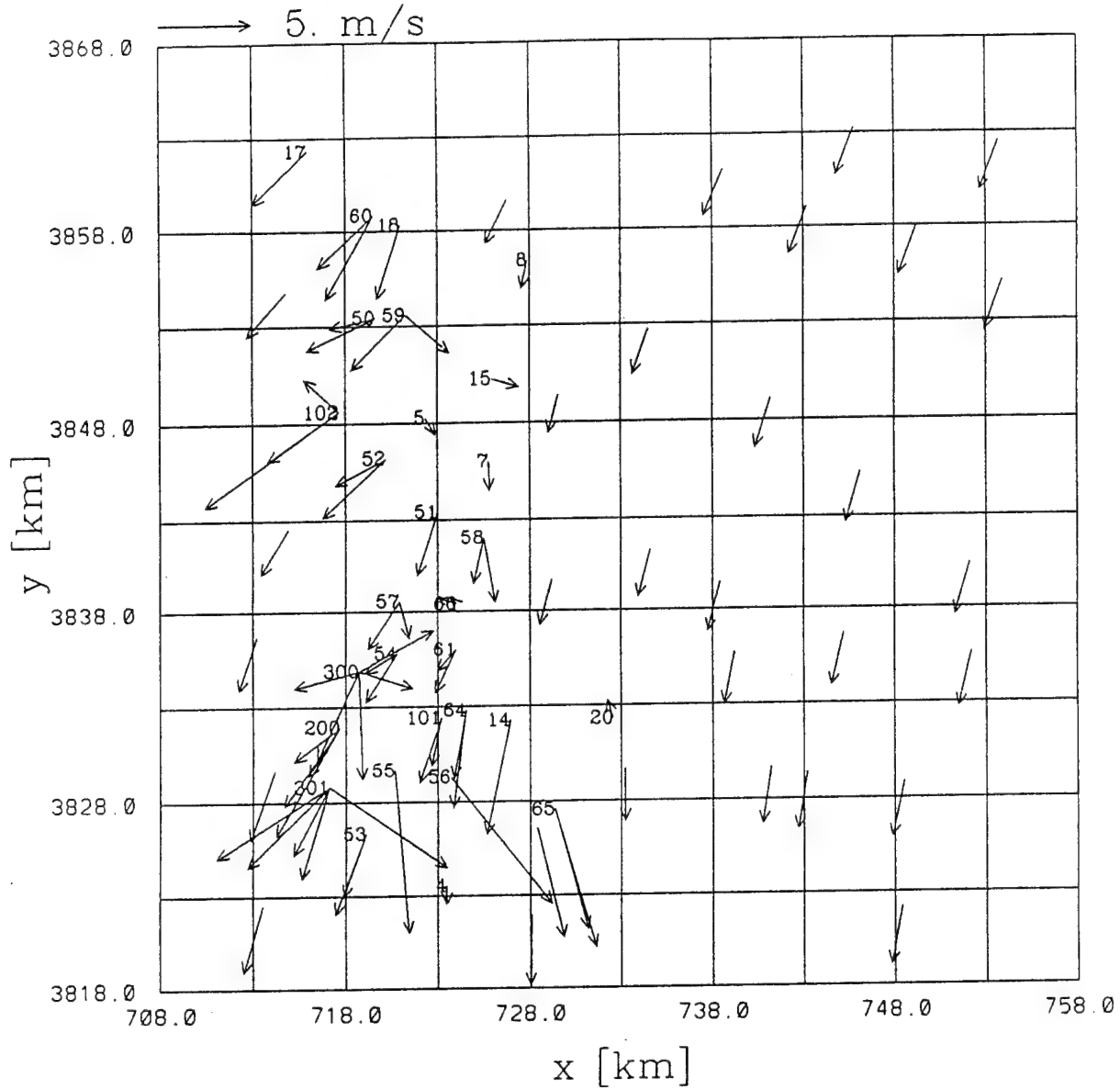


Figure 12. Wind Vectors at Tower Locations (With Numbers) and those at Puff Centers (Without Numbers) at 1110 LT, January 11, 1993. Puff Velocities were Extrapolated from Tower Velocities.

WIND VECTORS VAFB 11293 1110 12ft

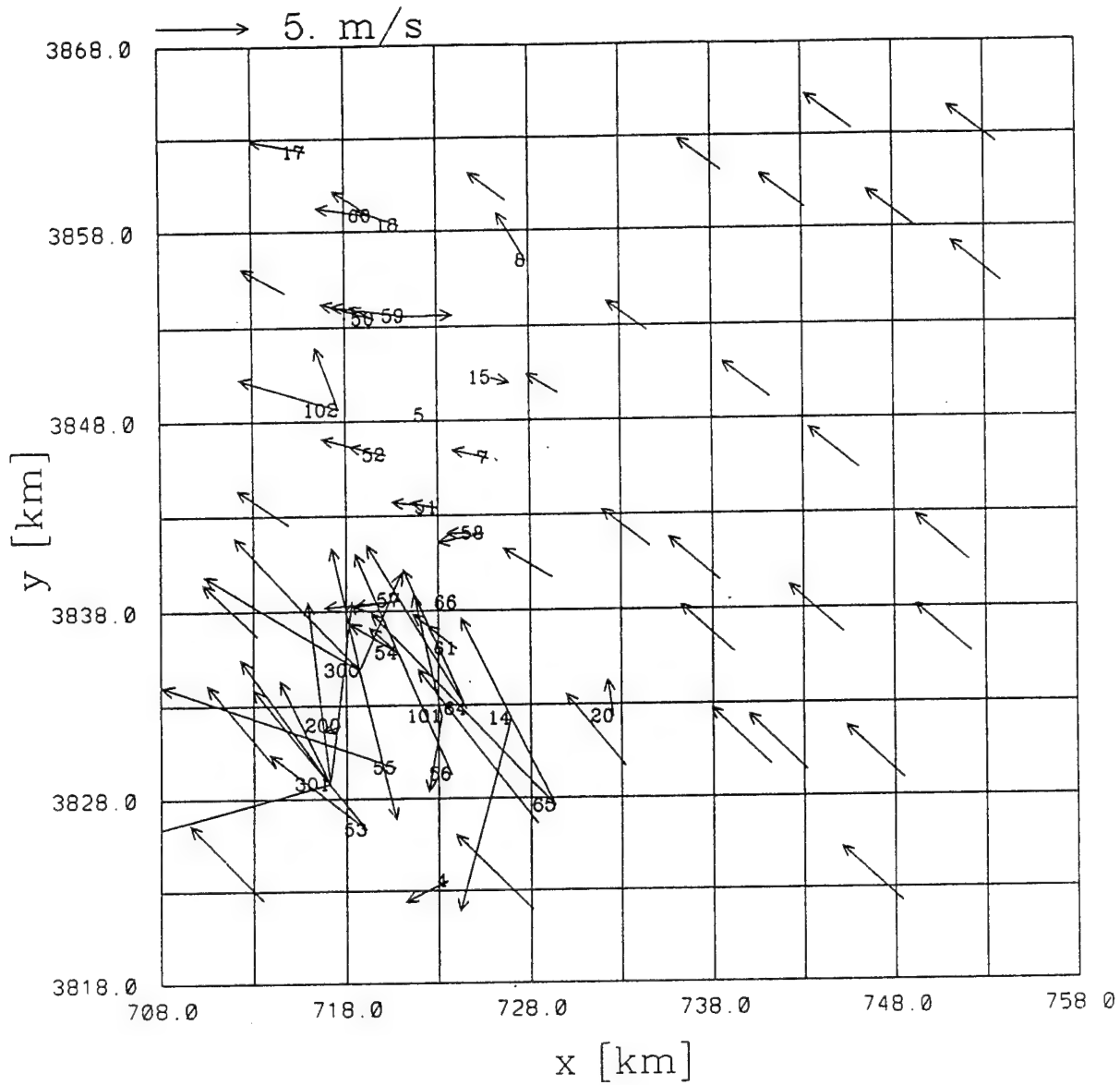


Figure 13. Similar to Figure 12 but for January 12, 1993.

WIND VECTORS VAFB 11393 1110 12ft

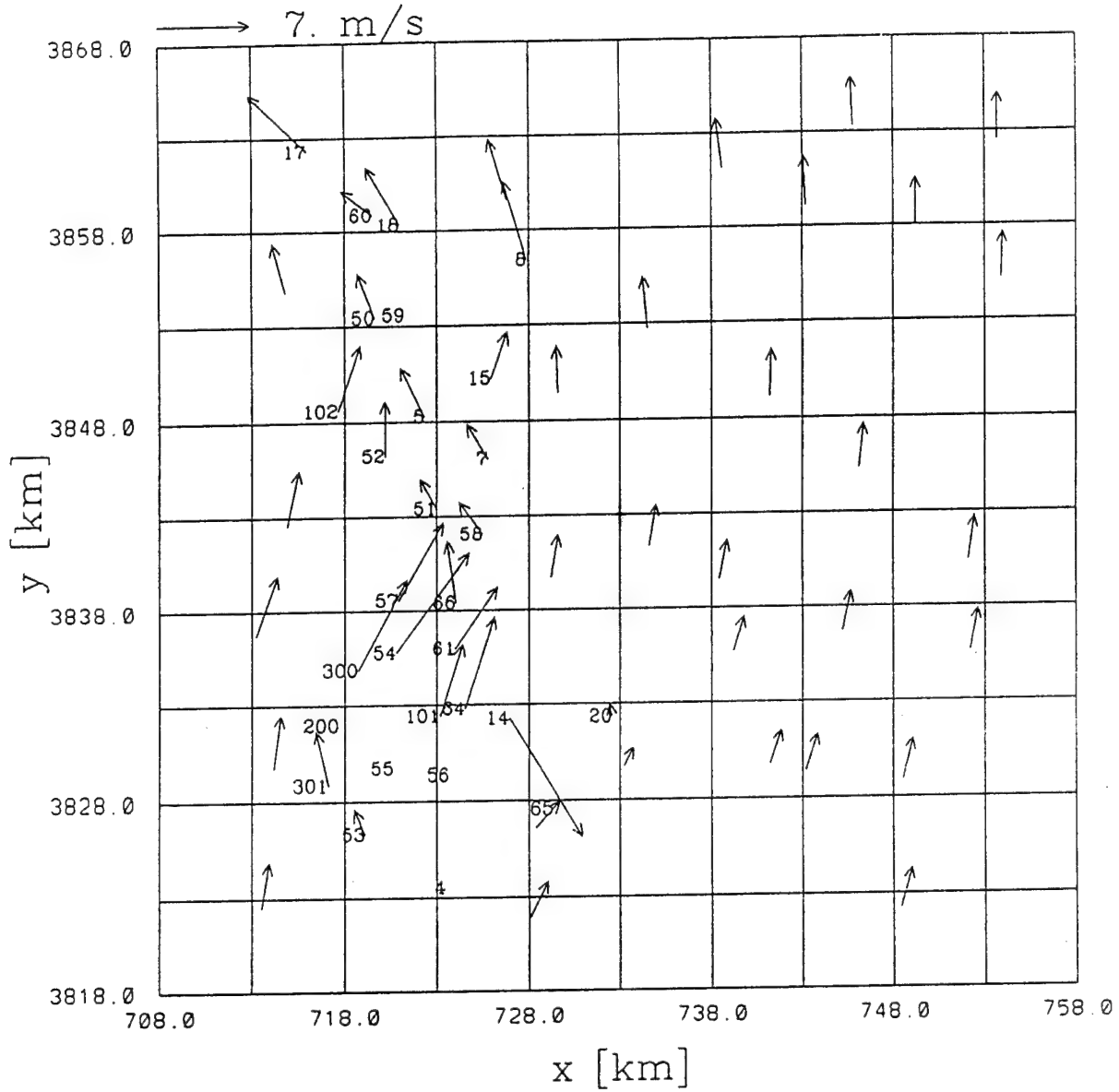


Figure 14. Similar to Figure 12 but for January 13, 1993.

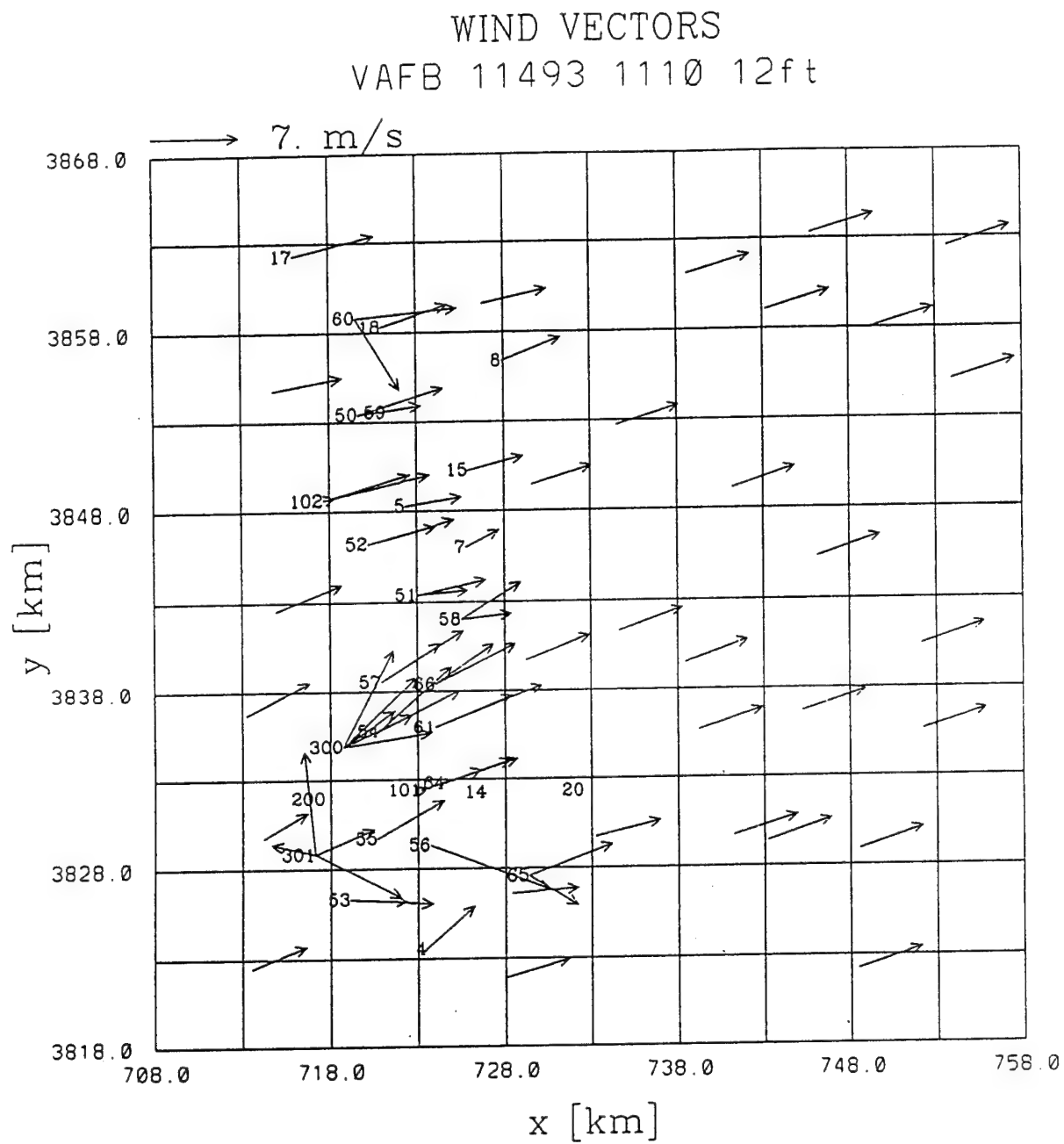


Figure 15. Similar to Figure 12 but for January 14, 1993.

WIND VECTORS VAFB 11593 1110 12ft

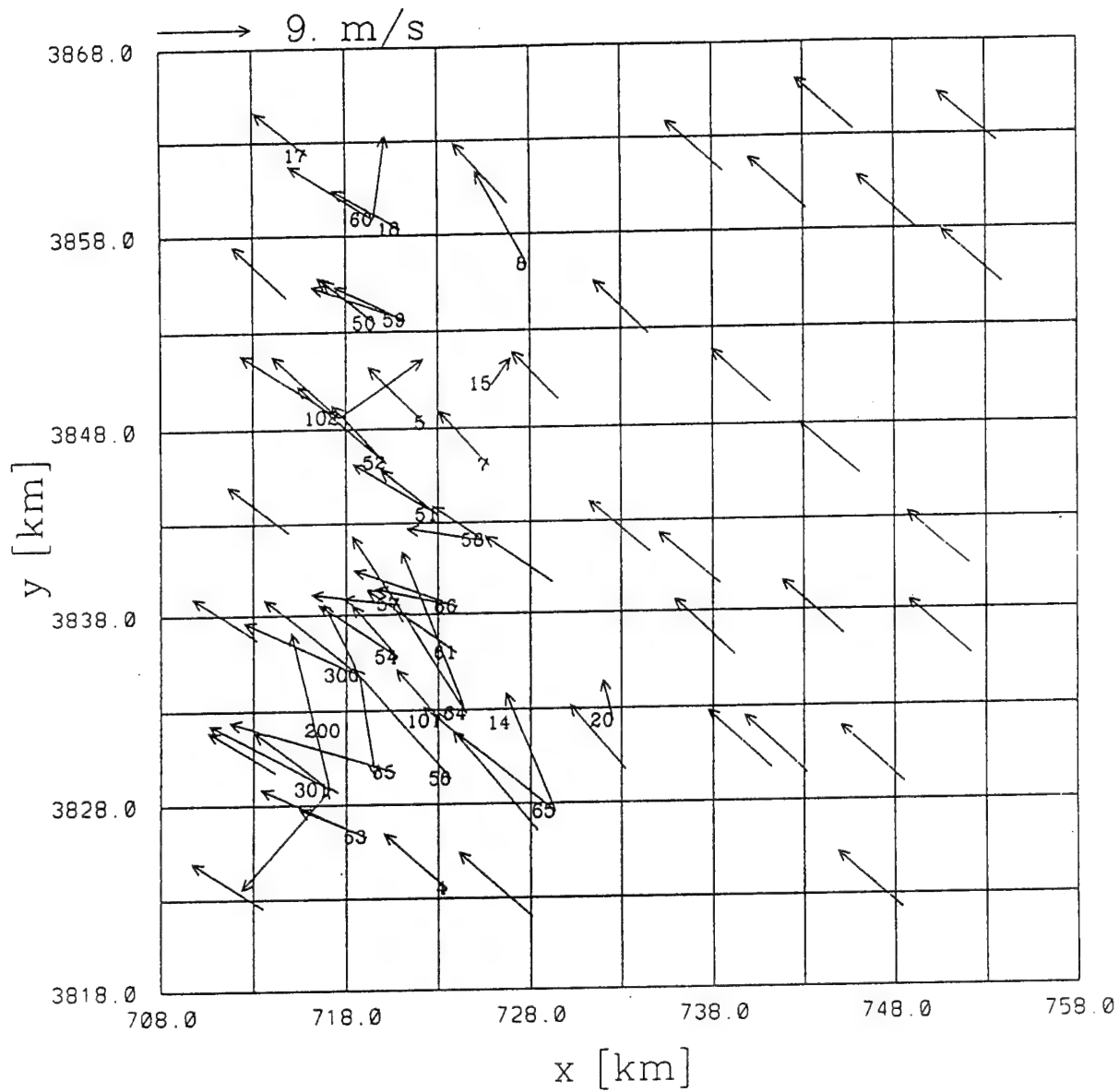


Figure 16. Similar to Figure 12 but for January 15, 1993.

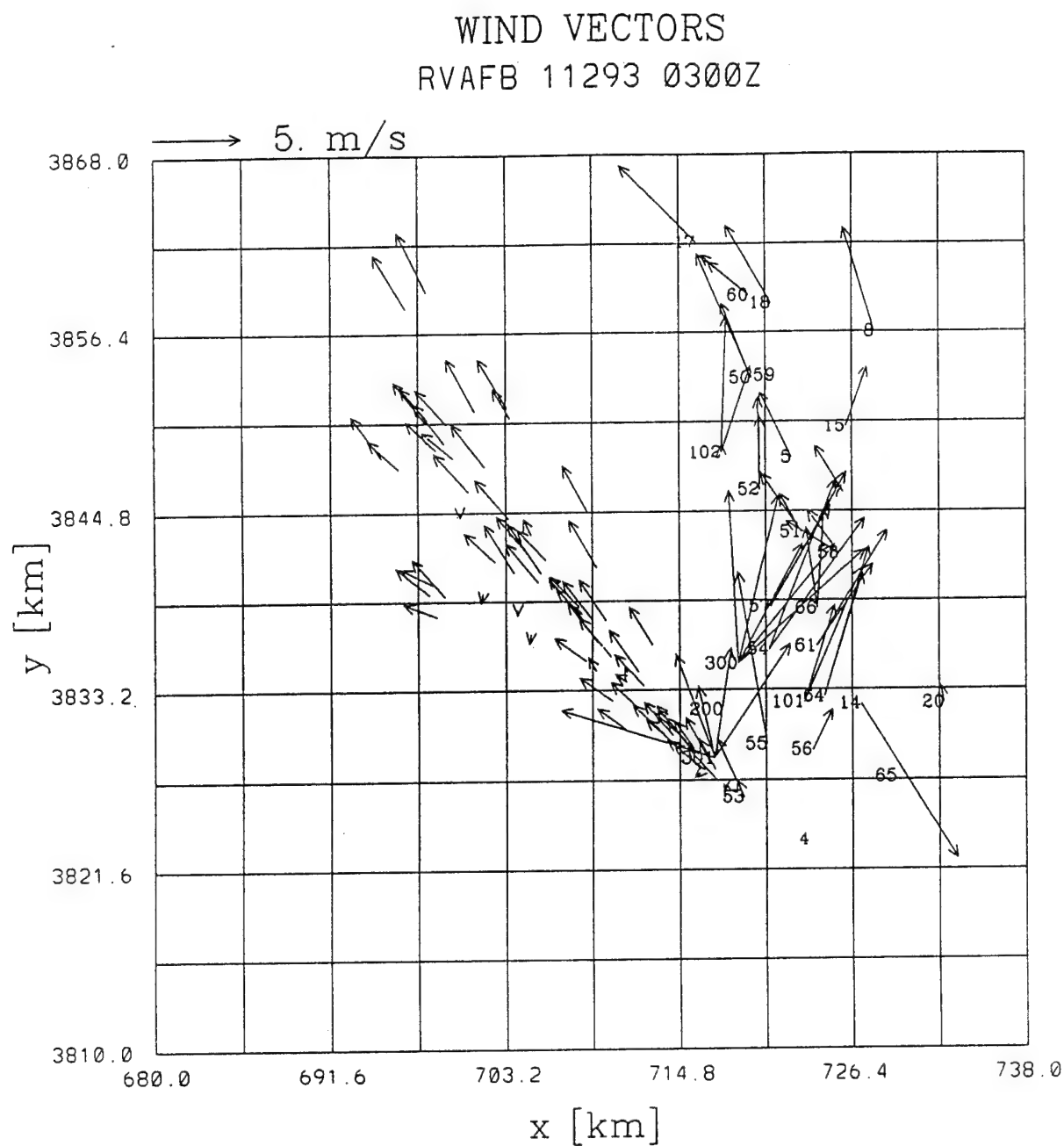


Figure 17. Wind Vectors at Tower Locations (With Numbers) and Those at Puff Centers (Without Numbers) at 0300 Z, January 12, 1993. Puff Velocities Were Computed from Tower Data and HOTMAC Winds by $1/r^2$ Weighting Method.

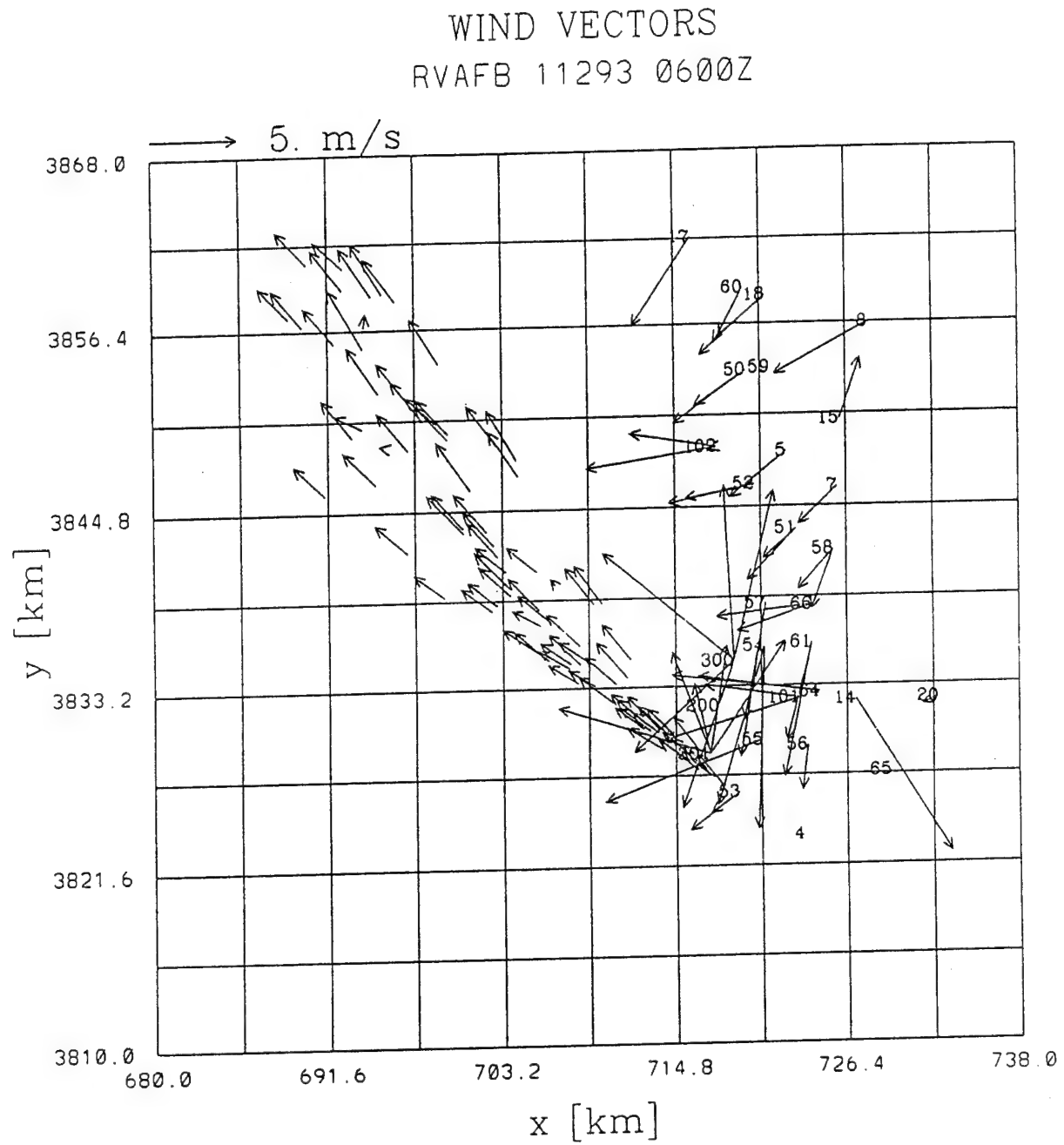


Figure 18. Similar to Figure 17 but for 0600 Z, January 12, 1993.

45

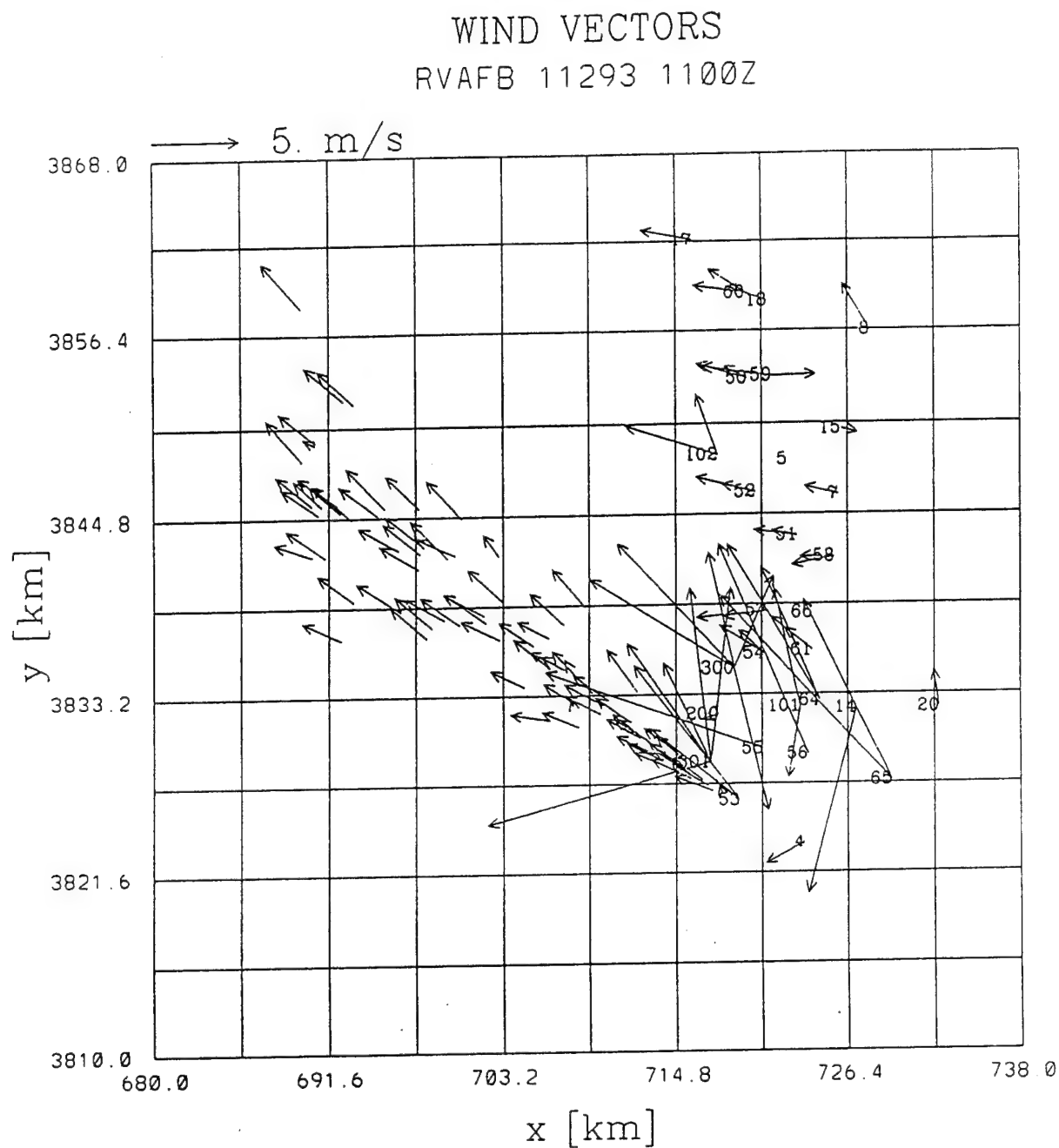


Figure 20. Similar to Figure 17 but for 1100 Z, January 12, 1993.

on the distance between a puff center and the nearest tower site. If a puff is located at a tower site, then the tower wind is used for puff velocity. The weight function decreases exponentially as the distance between a puff and a tower increases. Such an assumption is particularly reasonable for airflows over complex terrain, where wind distributions are largely localized.

Tower data are optional. An input file **rpinp** sets a flag for simulations with and without tower data.

D. TASK 4: *Add to the model the physics necessary to forecast the formation and dissipation of fog.*

Fog and/or low stratus clouds are frequently observed at VAFB, and affect the heat energy balance at the ground. The interaction of fog, solar heating, long-wave radiation heating/cooling, and turbulence mixing is complex and is not yet well understood. Fog physics was incorporated into a one-dimensional version of HOTMAC and the results were tested with the data taken at Cabaw meteorological tower (Reference 32). The results were satisfactory, and the fog physics was incorporated into a three-dimensional version of HOTMAC.

1. Ensemble Cloud Modeling

The terms for the rate of condensation are purposely eliminated by introducing the liquid water potential temperature ($\tilde{\theta}_l$) and mixing ratio of total water (\tilde{Q}_l). In order to recover the potential (or absolute) temperature and the mixing ratios of water vapor and liquid water, Gaussian cloud relations, proposed by Sommeria and Deardorff (Reference 33) and Mellor (Reference 34), are used. The present method has been applied to simulations of the BOMEX data (Reference 35), and GATE data (Reference 36).

Following Mellor (Reference 35) we assume the probability density function G for $\tilde{\theta}_l$ and \tilde{Q}_l to be Gaussian so that

$$G = \frac{1}{2\pi\sigma_{\theta l}\sigma_{qw}(1-r^2)^{1/2}} \exp \left[\frac{-1}{1-r^2} \times \left\{ \frac{\theta_l^2}{2\sigma_{\theta l}^2} - r \frac{\theta_l q_w}{\sigma_{\theta l}\sigma_{qw}} + \frac{q_w^2}{2\sigma_{qw}^2} \right\} \right], \quad (9)$$

where $\sigma_{\theta l}^2 \equiv \overline{\theta_l^2}$, $\sigma_{qw}^2 \equiv \overline{q_w^2}$, $r \equiv \overline{\theta_l q_w} / \sigma_{\theta l}\sigma_{qw}$, and \sim represents an instantaneous value. The results are presented here without details of derivation. Readers are referred to Mellor (Reference 34) for details.

First we define

$$a \equiv \left(1 + Q_{sl,T} \frac{L_v^{-1}}{c_p} \right), \quad (10)$$

$$b \equiv a \frac{\langle T \rangle}{\langle \Theta \rangle} Q_{sl,T}, \quad (11)$$

$$\Delta Q \equiv Q_w - Q_{sl}, \quad (12)$$

$$Q_{sl,T} \equiv \left(\partial \tilde{Q}_s / \partial \tilde{T} \right)_{\tilde{T}=T_l} = 0.622 \frac{L_v}{R_d} \frac{Q_{sl}}{T_l^2}, \quad (13)$$

$$Q_{sl} = 0.622 e_s(T_l) / (P - e_s(T_l)), \quad (14)$$

$$e_s(T_l) = 6.11 \exp \left[\frac{L_v}{R_w} \left(\frac{1}{273} - \frac{1}{T_l} \right) \right], \quad (15)$$

and

$$T_l \equiv (P/P_o)^k \Theta, \quad (16)$$

where Q_{sl} is the mean saturation mixing ratio of water vapor at T_l ; T_l is the liquid water temperature defined by Equation (16); $e_s(T_l)$ is the saturation water vapor pressure at T_l ; and R_w is the gas constant for water vapor. Mellor (Reference 34) obtained the following expressions. A

function R which indicates a fraction of cloud coverage for a given volume of air is found, i.e.,

$$R = \int_{-\infty}^{\infty} \int_{-\infty}^{\infty} H(\tilde{Q}_w - \tilde{Q}_s) G d\tilde{Q}_w d\tilde{\theta}_l \quad (17)$$

$$= \frac{1}{2} \left[1 + \operatorname{erf} \left(Q_1 / \sqrt{2} \right) \right],$$

where $\operatorname{erf}(x) = 2/\sqrt{\pi} \int_0^x \exp(-y^2) dy$ and $H(x)$ is the Heaviside function. For Q_c

$$\frac{Q_c}{2\sigma_s} = RQ_1 + \frac{1}{\sqrt{2\pi}} \exp\left(-\frac{Q_1^2}{2}\right), \quad (18)$$

where

$$Q_1 \equiv a\Delta Q / (2\sigma_s), \quad (19)$$

and

$$\sigma_s^2 = \frac{1}{4} \left(a^2 \overline{q_w^2} - 2ab \overline{q_w \theta_l} + b^2 \overline{\theta_l^2} \right). \quad (20)$$

Furthermore,

$$\frac{\overline{q_c \theta_l}}{a \overline{q_w \theta_l} - b \overline{\theta_l^2}} = \frac{\overline{q_c q_w}}{a \overline{q_w^2} - b \overline{q_w \theta_l}} = R', \quad (21a,b)$$

and

$$\frac{\overline{u_j q_c}}{a \overline{u_j q_w} - b \overline{u_j \theta_l}} = R', \quad (22)$$

where

$$R' = R - \frac{Q_1}{2\sigma_s} \frac{1}{\sqrt{2\pi}} \exp\left[-\frac{Q_1^2}{2}\right]. \quad (23)$$

Finally, $\overline{q_l^2}$, the variance of cloud water mixing ratio, is expressed as

$$\frac{\overline{q_c^2}}{4\sigma_s^2} = R \left[1 + \left(Q_1 - \frac{Q_c}{2\sigma_s} \right)^2 \right] + \left(Q_1 - 2 \frac{Q_c}{2\sigma_s} \right) \frac{1}{\sqrt{2\pi}} \exp\left[-\frac{Q_1^2}{2}\right]. \quad (24)$$

Figure 21 shows R , $Q_c/2\sigma_s$, and $q_c^2/4\sigma_s^2$ as functions of Q_1 obtained according to Equations (17), (18), and (24), respectively.

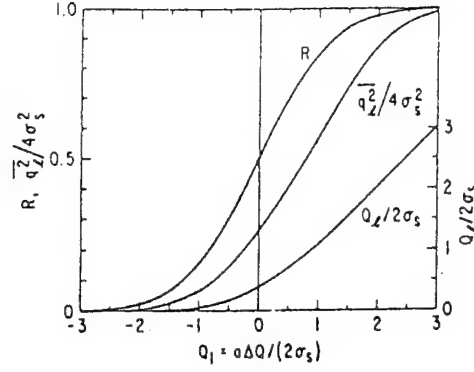


Figure 21. Fraction of Cloud Coverage R , Mixing Ratio of Liquid Water Q_c , and Variance of Liquid Water, $q_c^2/4\sigma_s^2$ as a Function of Q_1 .

As seen from Figure 21, a fraction of cloud coverage R varies gradually with Q_1 and takes non-zero values even if Q_1 is negative. In other words, clouds can exist even if the mixing ratio of water vapor averaged over a grid volume is not saturated. This is realistic because the grid spacing normally used in mesoscale models are larger than the size of small clouds. Therefore, the present cloud model can use a relatively large grid spacing, which could save substantial computational time. A statistical cloud model such as the present one avoids the ambiguous condensation criteria often used by coarse-grid models, where saturation values are lowered arbitrarily to compensate for the amount of cloud not resolved by the grids.

The turbulence second moments in Equation (20) and Equations (21 a,b) are obtained by solving second-moment turbulence-closure equations. Those expressions are given in Yamada and Mellor (Reference 35).

2. Short-Wave and Long-Wave Radiation Parameterizations

Solar and long-wave radiation play important roles in the formation and dissipation of clouds and fog. For example, radiation fog forms when moist air near the surface condenses as the ground temperature decreases due to long-wave radiation cooling. As the sun rises, fog reflects, absorbs, and transfers short-wave solar radiation. The solar energy absorbed in a fog layer heats the air and converts liquid water to water vapor. The solar energy transmitted through

fog heats the ground and increases ground temperature. The warmed ground, in turn, heats the air above it.

This interaction between radiative transfer and cloud development is thus understood qualitatively. Quantitative description is complex, however, and involves considerable computations (Reference 37; Reference 38). This is why many numerical models either neglect the radiative effects on clouds or adopt a very simple, highly parameterized method.

Hanson and Derr (Reference 39) proposed a parameterized solar radiation scheme whose parameters were obtained by curve-fitting to numerical radiative-transfer results using the ATRAD narrow-band model (Reference 40). This parameterized method is simple, yet reproduced solar flux profiles within a single cloud layer which were in good agreement with the numerical results obtained from ATRAD.

Motivated by the success of the solar radiation scheme, Hanson and Derr proposed an infrared (IR) radiation scheme expressed by exponential functions whose decay parameters were determined by the emissivity methods (Reference 41). This method reproduced IR flux profiles within layered clouds which were in good agreement with the numerical results and observations for thick clouds (-800 meters). However, the parameterization overestimated the flux decrease at the cloud top and underestimated the cloud base warming compared to the numerical model for thin clouds (-300 meters).

We proposed to adopt the Hanson and Derr parameterization scheme because of its simplicity and because it can produce flux profiles which are in good agreement with observations and numerical model results.

The solar and IR parameterizations are summarized in the following.

a. Short-Wave Radiation

Following the two-stream model solutions by Stephens (Reference 42), reflection (R_e), transmission (T_r) and absorption (A) are expressed as:

(i) Nonabsorbing medium [$\tilde{w}_0 = 1(\lambda \leq 0.75\mu m)$]

$$R_e(\mu_0) = \frac{\beta(\mu_0)\tau_N/\mu_0}{1 + \beta(\mu_0)\tau_N/\mu_0} \quad (25)$$

$$T_r(\mu_0) = 1 - R_e(\mu_0) \quad (26)$$

(ii) Absorbing medium [$\tilde{w}_0 < 1(\lambda > 0.75\mu m)$]

$$R_e(\mu_o) = [(u^2 - 1)\exp(\tau_{eff}) - \exp(-\tau_{eff})]/R \quad (27)$$

$$T_r(\mu_o) = 4u/R \quad (28)$$

$$A_b(\mu_o) = 1 - R_e(\mu_o) - T_r(\mu_o) \quad (29)$$

where

$$u^2 = [1 - \tilde{w}_o + 2\beta(\mu_o)\tilde{w}_o]/(1 - \tilde{w}_o) \quad (30)$$

$$\tau_{eff} = \{(1 - \tilde{w}_o)[1 - \tilde{w}_o + 2\beta(\mu_o)\tilde{w}_o]\}^{\frac{1}{2}}\tau_N/\mu_o \quad (31)$$

$$R = (u + 1)^2\exp(\tau_{eff}) - (u - 1)^2\exp(-\tau_{eff}) \quad (32)$$

In the above expressions, μ_o is the zenith angle, τ_N is the optical thickness of the cloud, \tilde{w}_o is the single-scattering albedo, and β is the backscattered fraction of monodirectional incident radiation. The values for \tilde{w}_o and β are tabulated as functions of τ_N and μ_o .

Now solar radiation flux profile within the layered cloud is computed from the following equations (Reference 39):

$$F(z) = F_B - (F_B - F_C)[1 - \exp(-(z_B - z)/\lambda_S)] / \{1 - \exp[-(z_B - z_C)/\lambda_S]\} \quad (33)$$

where

$$\lambda_S = a(\mu_o)W + b(\mu_o)(1 - \exp\{-[\gamma W + c(\mu_o)]\}) \quad (34)$$

$$F_C = F_B + A_b F_B \downarrow \quad (35)$$

$$a(\mu_o) = -0.022 + 0.038(1 - \mu_o) \quad (36)$$

$$b(\mu_o) = 56.8 - 14.7(1 - \mu_o) \quad (37)$$

$$c(\mu_o) = 1.07 - 1.15(1 - \mu_o) \quad (38)$$

In the above expressions W is the total cloud liquid water content, which is given as,

$$W = \int_{z_C}^{z_B} \rho(z) Q_C(z) dz \quad (39)$$

where $\rho(z)$ is the air density, z_B is the cloud top, and z_C is the cloud base. The units of W are gm^{-2} and $\gamma=0.021$. $F_B = -F_{B\downarrow}\{1-R(\mu_o)\}$ where $F_{B\downarrow}$ is the downward solar flux just above the top of the cloud.

b. Long-Wave Radiation

This parameterization relies on values of external conditions: T_B and T_C are the absolute temperature at the cloud top and the cloud base, respectively; $G_{B\downarrow}$ is the downward IR flux at the cloud top; $G_{C\downarrow}$ is the upward IR flux at the cloud base; $\alpha\uparrow = 0.13$ and $\alpha\downarrow = 0.158$.

The IR flux profiles in the layered cloud are given as

$$G(z) = G_L \exp[-(z - z_c)/\lambda_L] + G_u \exp[-(z_B - z)/\lambda_u], \quad (40)$$

where

$$G_L = \left\{ \tilde{G}_0 - \tilde{G}_1 \exp[-(z_B - z_C)/\lambda_U] \right\} / \tilde{D}, \quad (41)$$

$$G_U = \left\{ \tilde{G}_1 - \tilde{G}_0 \exp[-(z_B - z_C)/\lambda_L] \right\} / \tilde{D}, \quad (42)$$

$$\tilde{D} = 1 - \exp\{-(z_B - z_C)/\lambda_N\}, \quad (43)$$

$$\frac{1}{\lambda_N} = \frac{1}{\lambda_U} + \frac{1}{\lambda_L}, \quad (44)$$

$$\tilde{G}_0 = G_C \uparrow - B_C + (B_C - G_B \downarrow) \exp(-\eta \downarrow), \quad (45)$$

$$\tilde{G}_1 = (G_C \uparrow + B_B - 2B_C) \exp(-\eta \uparrow) + B_B - G_B \downarrow \quad (46)$$

$$\eta \uparrow, \downarrow = \alpha \uparrow, \downarrow W, \quad (47a,b)$$

$$B_C = \sigma T_C^4, \quad (48)$$

$$B_B = \sigma T_B^4, \quad (49)$$

$$\lambda_L = 70W / \left(W - W^{\frac{1}{2}} + 2.67 \right), \quad (50)$$

$$\lambda_U = 140W^{-0.56} \quad (51)$$

where σ is the Stefan-Boltzmann constant.

3. Precipitation Microphysics

Following Nickerson (Reference 43), the microphysics are expressed in the following equations:

$$\frac{\partial Q_w}{\partial t} = -\left(\frac{\partial Q_r}{\partial t}\right)_{sedi} \quad (52)$$

$$\frac{\partial Q_r}{\partial t} = \left(\frac{\partial Q_r}{\partial t}\right)_{auto} + \left(\frac{\partial Q_r}{\partial t}\right)_{accr} - \left(\frac{\partial Q_r}{\partial t}\right)_{evap} + \left(\frac{\partial Q_r}{\partial t}\right)_{sedi} \quad (53)$$

$$\frac{\partial N_r}{\partial t} = \left(\frac{\partial N_r}{\partial t}\right)_{auto} - \left(\frac{\partial N_r}{\partial t}\right)_{self} + \left(\frac{\partial N_r}{\partial t}\right)_{sedi} \quad (54)$$

where Q_w is the sum of mixing ratios for water vapor, cloud water, and rain water. Q_r is the rain water mixing ratio and N_r is the raindrop number concentration. The subscript *auto* is for autoconversion of cloud droplets into raindrops, *accr* is for accretion of cloud droplets by raindrops, *self* is for the self-collection of the raindrops, *evap* is for rain evaporation and *sedi* is for rain sedimentation. Nickerson (Reference 43) discussed in detail the expressions for those microphysics processes. This hydrological model is substantially more complex than Kessler's (Reference 44) classical parameterization for the treatment of microphysics. The model is based on a more realistic log-normal distribution than the Marshall-Palmer distribution in Kessler's parameterization. The mean diameter of raindrops in a given volume is estimated from equations for the mean rain water mixing ratio and the raindrop number concentration. The terminal velocity of raindrops in each volume is calculated as a function of the mean raindrop diameter, thus the terminal velocity values in the model are expected to be more accurate than those obtained by a simple parameterization.

4. Simulation of Maritime Stratus Clouds

A numerical simulation was conducted to investigate complex interactions among clouds, turbulence, and atmospheric radiation. Maritime stratus clouds were simulated by using a one-dimensional version of HOTMAC (Reference 20).

Integration initiated at 0000 LT on day 200 and continued for 48 hours. The results for the second 24-hour simulations are presented here. Figure 22 shows a time-height variation of the mixing ratio of cloud liquid water. Clouds were thick during the nocturnal period and occupied the layer between 1200 meters and 1600 meters above the sea surface. As the short-wave solar radiation heating increased, clouds dissipated from the lower part and the clouds became as thin as 100 meters by 1800 LT. As the solar heating subsided, the cloud thickness increased again. Figure 23 shows the diurnal variations of the mixing ratio of rain water. Rain was produced in the cloud but evaporated before it reached the surface except during a short period between 0600 and 0800.

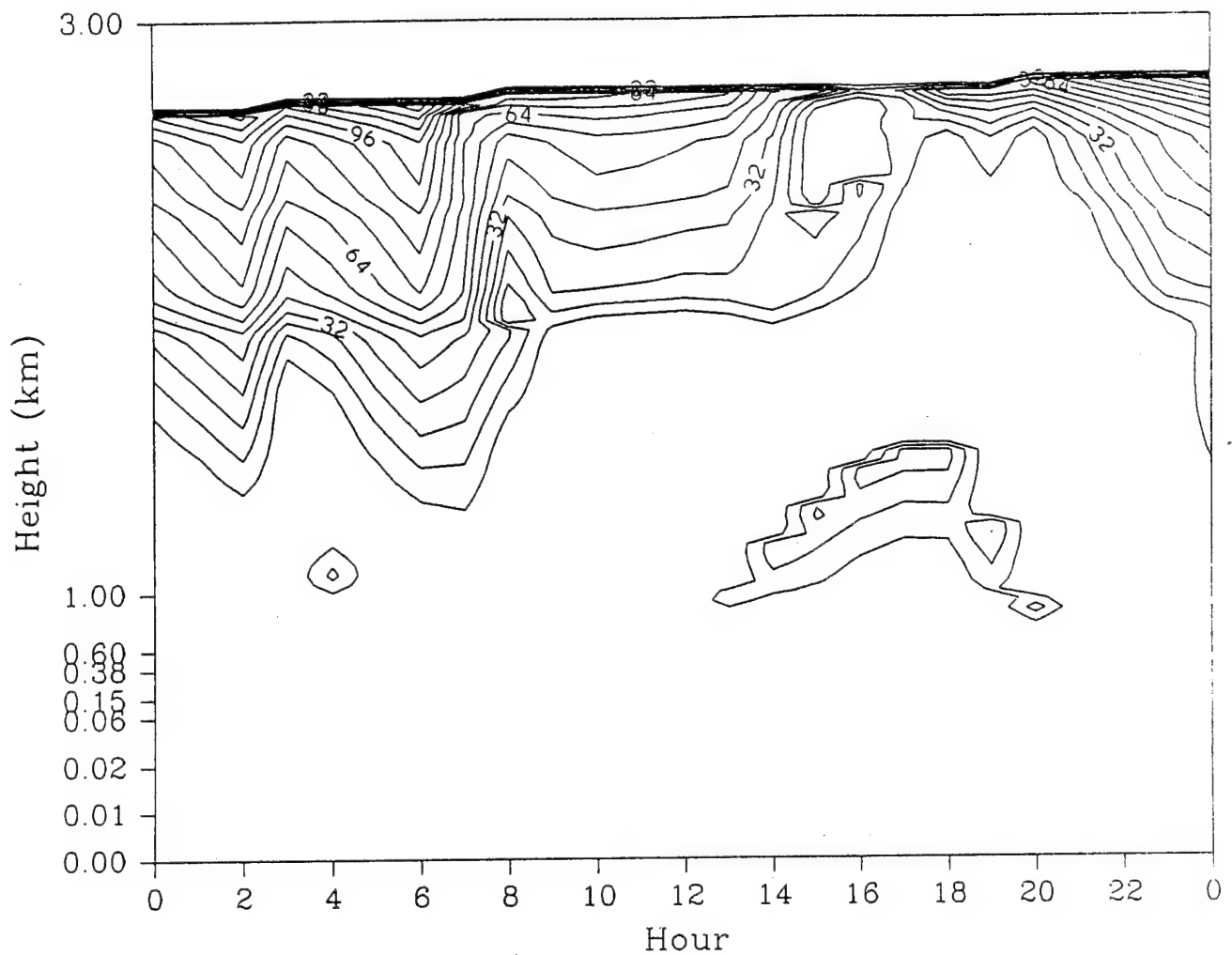
Figures 24 and 25 show, respectively, the short-wave radiation heating rate ($^{\circ}\text{C}/\text{day}$) and the long-wave radiation cooling rate ($^{\circ}\text{C}/\text{day}$). The short-wave radiation heating was maximum at the cloud top and decreased exponentially within the cloud (Reference 39). Short-wave radiation heating (Figure 24) was offset by long-wave radiation cooling at the cloud top (Figure 25). Figure 25 also indicates long-wave radiation warming at the cloud base.

No attempt was made to compare simulations with observations.

A one-dimensional version of HOTMAC was used to simulate time evolution of fog over horizontally homogeneous terrain. The results were compared with data taken at Cabaw meteorological tower in the Netherlands (Reference 31). Wind, temperature, and the mixing ratio of water vapor were initialized with measurements. Simulations were initiated at midnight of day 215 and continued for 24 hours.

Fog began to form almost immediately, as the air temperature decreased due to cooling at the ground (Figure 26). The height of the fog increased as the air temperature near the fog

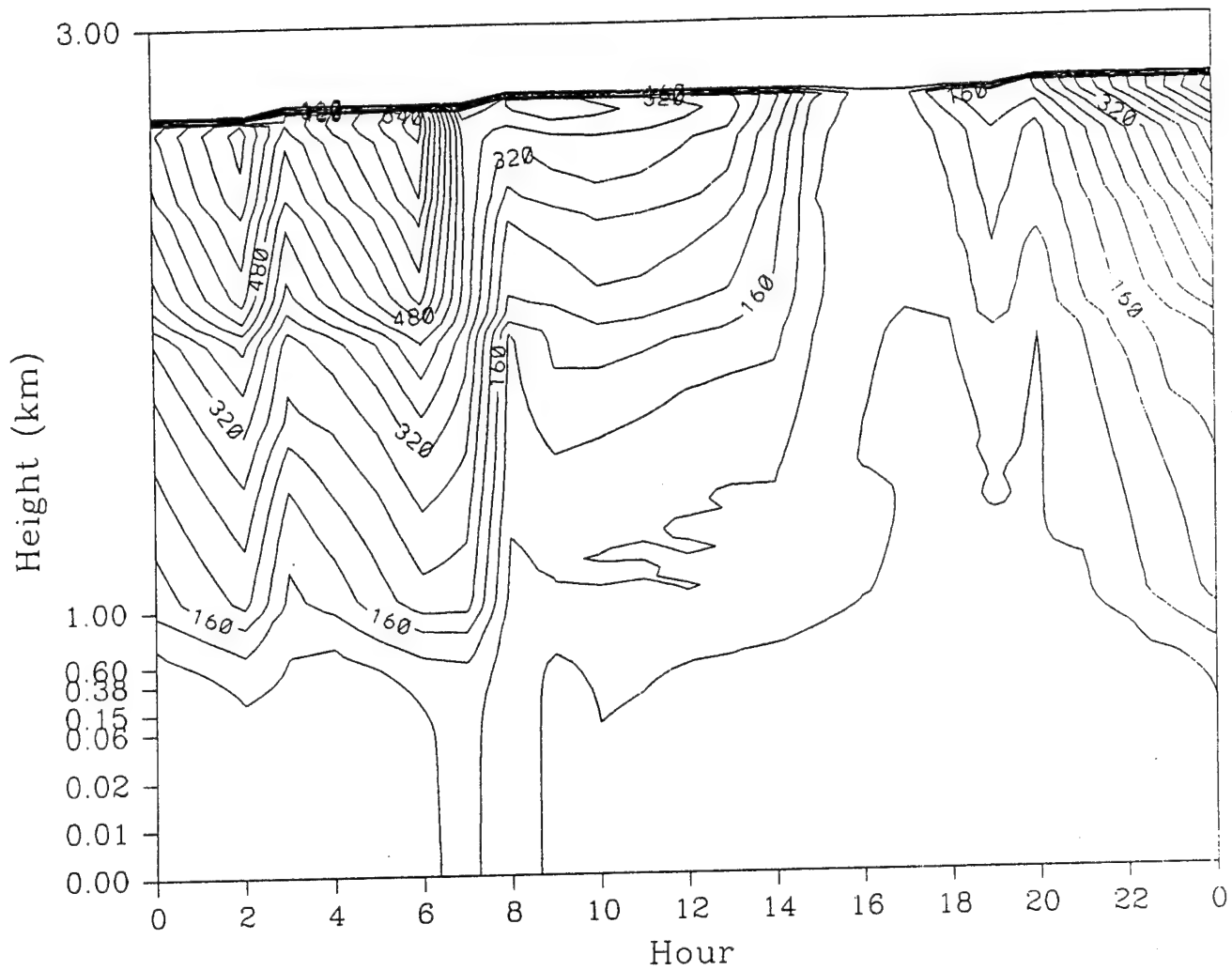
CLIQ
Day 201



CONTOUR FROM 0. TO 0.12800E-02 CONTOUR INTERVAL OF 0.80000E-04 PT(3,3)= 0.19017E-09 LABELS SCALED BY 0.10000E+06

Figure 22. Diurnal Variation of the Cloud Water Mixing Ratio. Simulation of Maritime Stratus Cloud. Contour From 0 to 128 with an Interval of 8. Labels Scaled by 1.0×10^5 .

RLIQ
Day 201



CONTOUR FROM 0. TO 0.72000E-03 CONTOUR INTERVAL OF 0.40000E-04 PT(3,31) 0.74393E-04 LABELS SCALED BY 0.10000E-07

Figure 23. Similar to Figure 22, except for the Rain Water Mixing Ratio (g/g). Contour from 0 to 720 with an Interval of 40. Labels Scaled by 1.0e06.

RADSW Day 201

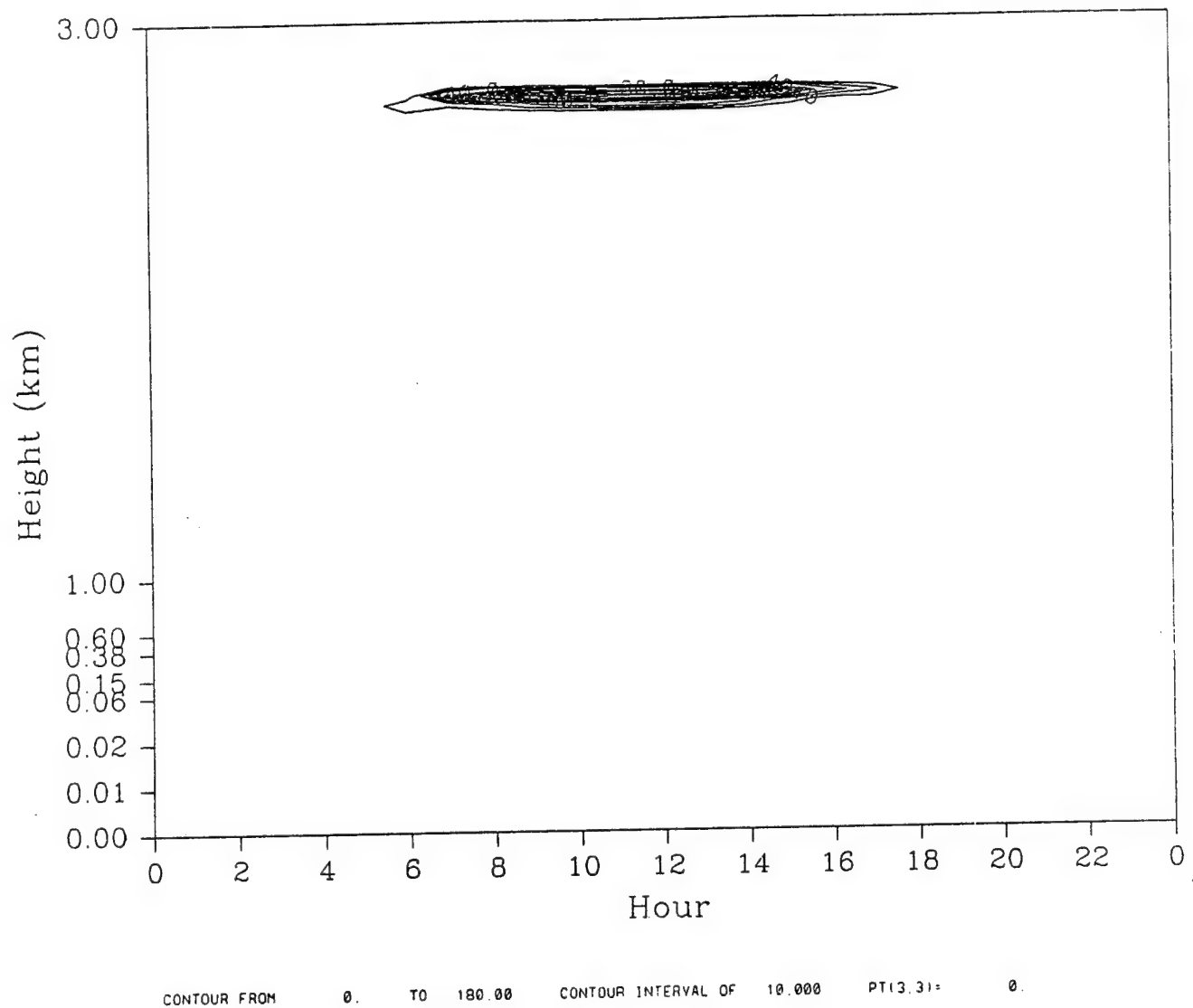
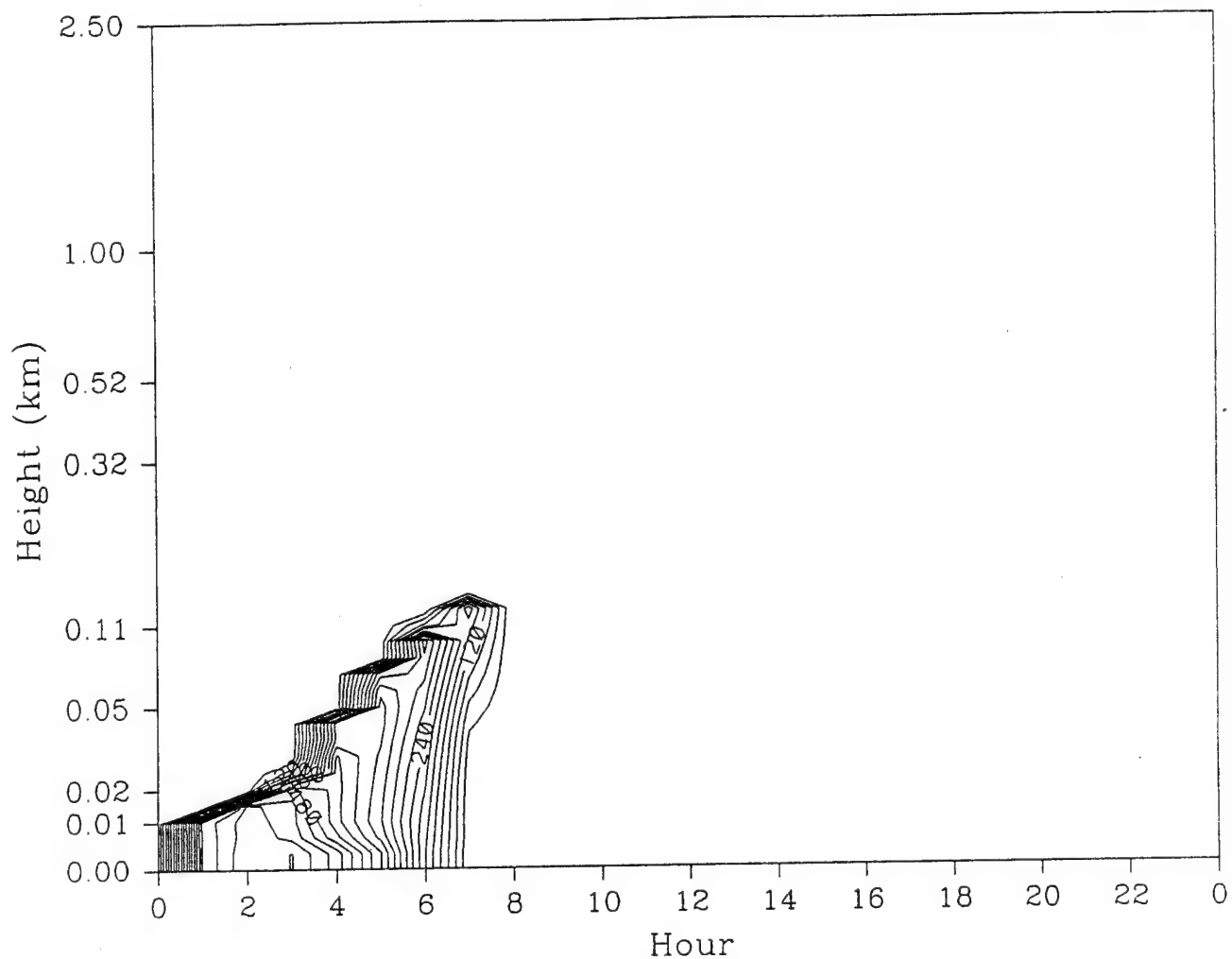


Figure 24. Similar to Figure 22, except for the Short-Wave Radiation Cooling Rate ($^{\circ}\text{C}/\text{day}$). Contour From 0 to 180 with an Interval of 10.

CLIQ
Day 215



CONTOUR FROM 0. TO 0.60000E-03 CONTOUR INTERVAL OF 0.30000E-04 PT(3,3)= 0.58686E-03 LABELS SCALED BY 0.10000E+07

Figure 26. Diurnal Variation of the Cloud Water Mixing Ratio. Simulation of Radiational Fog.
Contour from 0 to 600. Labels Scaled by 1.0e06.

5. Simulation of Fog

top decreased due to long-wave radiation cooling. The mixing ratio of cloud water reached a maximum value around 0300.

Sunrise was shortly after 0500, but fog did not dissipate until 0700 because the amount of solar energy reached the ground was reduced considerably, due to reflection and absorption by the fog.

Figure 27 shows the modeled and observed temperature and mixing ratio of water vapor at 1.1 meters agl. The mixing ratio at the ground was assumed to be saturated while fog existed and a constant after fog dissipated. Simulations were in good agreement with observations.

E. TASK 5: *Develop an innovative method to treat plumes that are not neutrally buoyant.*

Highly buoyant plumes modify the wind and turbulence distributions of the ambient flow. It is almost impossible to parameterize or express such modifications without deploying a dynamic plume model. A physically correct way to treat nonneutrally buoyant plumes is to incorporate plume dynamics into HOTMAC. However, the dynamic plume model requires considerable computer time and is not practical for emergency modeling. This is a dilemma, for one must choose between being accurate (but impractical) and being practical (but inaccurate). It is necessary to adopt a plume parameterization scheme (instead of a dynamic plume model) to meet the time constraints of an emergency response modeling system.

We have tried two approaches: (1) modified HOTMAC to include plume dynamics (a fire code) and (2) modified RAPTAD only to incorporate the buoyant plume parameterization proposed by Van Dop (Reference 45). The fire code was previously run on a Cray supercomputer but has never been run on a Sun workstation. The fire code and graphics programs were modified to run on a workstation. The model produced the results identical to those produced on the supercomputer. But, as expected, run time was too long to be practical for emergency modeling.

Observed and Computed Values at 1.1 meter

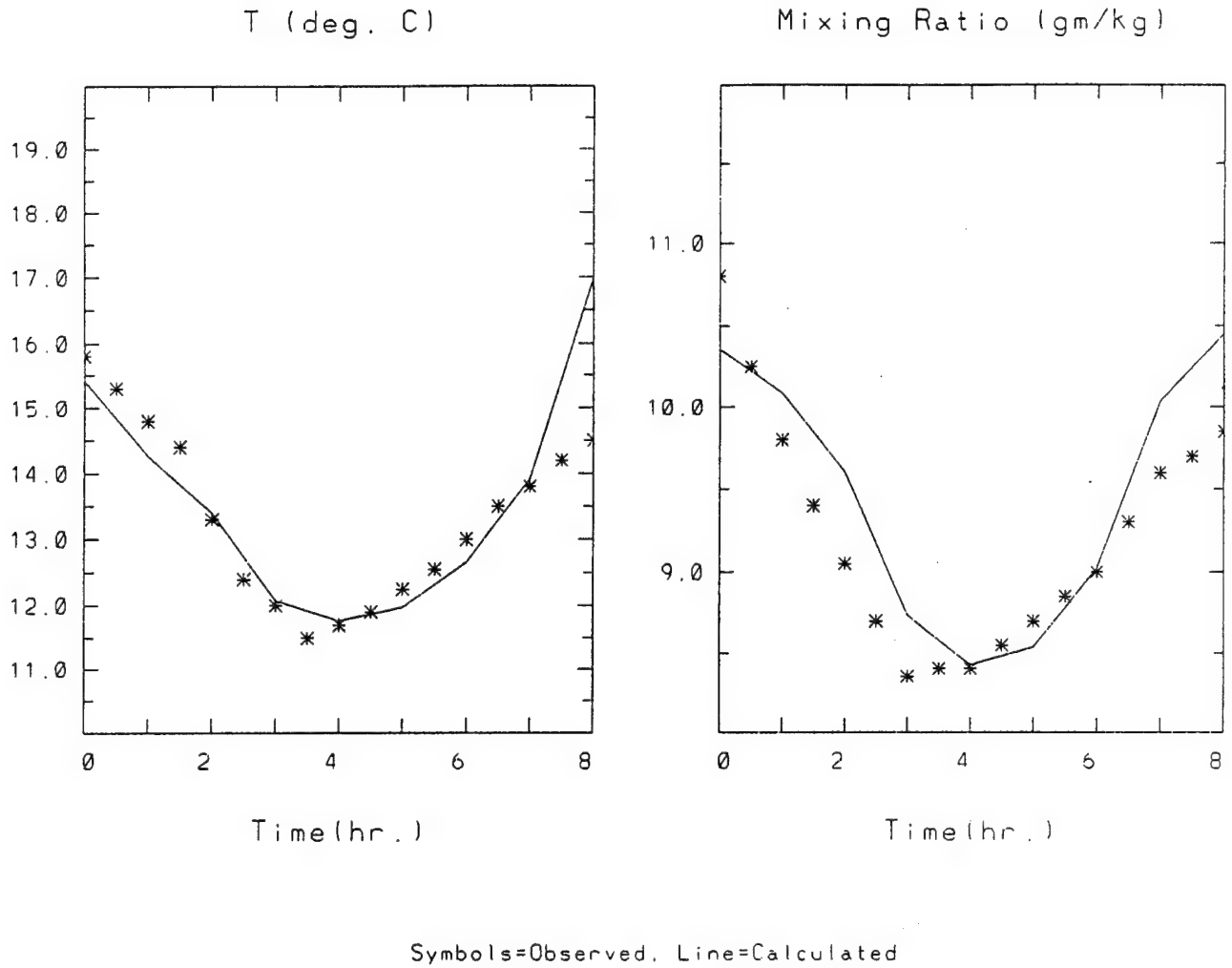


Figure 27. Time Variations of Modeled (-) and Observed (*) Temperature and Mixing Ratio of Water Vapor at 1.1 Meters agl.

The second approach, to modify RAPTAD to include buoyant plume effects, has the advantage of being faster. The disadvantage is that it does not consider the effects of a buoyant plume on the ambient airflows. In other words, the ambient airflows are considered to be unchanged even if a buoyant plume modifies both wind and temperature distributions. Thus, this approach is justifiable only when ambient air modifications are confined to a small area and the magnitude of any modification is small.

The vertical velocity of a buoyant plume is computed from the Langevin equation of motion for a homogeneous and stationary turbulent flow. The temperature of a buoyant plume is also assumed to be computed by the Langevin equation. Following Van Dop (Reference 45), vertical velocity (\overline{W}), buoyancy (\overline{B}), and plume height (\overline{Z}) are computed from the following equations.

$$\frac{d\overline{W}}{dt} = -\frac{\overline{W}}{T_W} + \overline{B}, \quad (55)$$

$$\frac{d\overline{B}}{dt} = -\frac{\overline{B}}{T_B} - N^2\overline{W}, \quad (56)$$

$$\frac{d\overline{Z}}{dt} = \overline{W}, \quad (57)$$

where

$$B = \frac{g}{T}(\Theta - \Theta_a), \quad (58)$$

$$N^2 = \frac{g}{T} \frac{d\Theta_a}{dz}, \quad (59)$$

$$T_w = T_B = A(t + t_o), \quad (60)$$

$$A = 3/4, \quad (61)$$

$$t_o = 1 \text{ sec.} \quad (62)$$

In the above equations, Θ and Θ_a are potential temperatures of plume and ambient air, respectively.

Test simulations were conducted under neutral conditions ($N^2 = 0$) and the results were compared with analytical solutions. Figure 28 shows time variations of \bar{B} , \bar{W} , and \bar{Z} where initial buoyancy of 1 m/s^2 and initial vertical velocity of 0.1 m/s were used. Simulations and analytical solutions are in good agreement.

Simulations were repeated under stable ($N^2 > 0$) and unstable ($N^2 < 0$) atmospheric conditions. Figures 29 and 30 show time variations of \bar{B} , \bar{W} , and \bar{Z} when $N^2 = (0.408)^2$ and $N^2 = -(0.408)^2$, respectively. Initial buoyancy of 1 m/s^2 and initial vertical velocity of 0 m/s were used.

Finally, simulations were conducted for a plume whose initial density is heavier than the ambient air. Initial buoyancy of -1 m/s^2 and initial vertical velocity of 0 m/s were used. Figures 31 and 32 show time variations of \bar{B} , \bar{W} , and \bar{Z} when $N^2 = (0.408)^2$ and $N^2 = -(0.408)^2$, respectively.

All simulations were conducted with an integration time step of 0.1 seconds. Accuracy decreased rapidly with increases in the integration time step. RAPTAD uses a time step of 10 seconds, but a small time step was necessary to simulate initial plume rise (drop) accurately. Therefore, a time step which increased linearly with time was used: the time step was 0.1 seconds initially and became 10 seconds at 100 seconds after the release. Figure 33 shows time variations of \bar{B} , \bar{W} , and \bar{Z} where $N^2 = -(0.408)^2$, $B_0 = -1$, and a variable time step were used. The results are in good agreement with those in Figure 32, where a constant time step of 0.1 was used.

F. TASK 6: *Develop a method to predict concentration variances, which are used to determine how a required confidence level affects the extent of a critical area.*

Relatively short time-averaging values are required for predicting concentrations of toxic materials. Such values normally exhibit great variations in time and space. Thus, predictions of

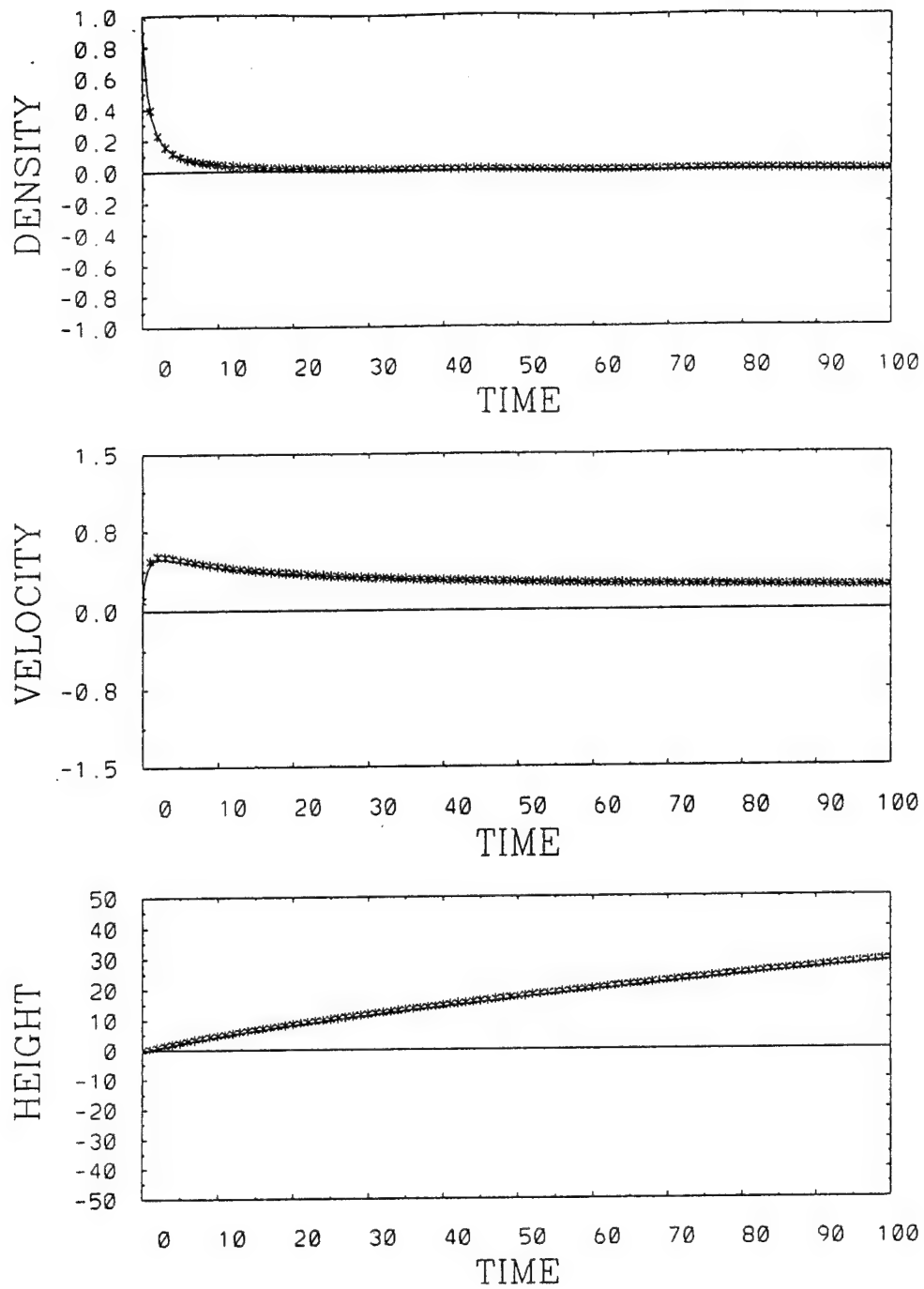


Figure 28. Time Variation of Buoyancy (m/s^2), Vertical Velocity (m/s), and Plume Height (m) in the Neutral Condition. Initial Buoyancy of 1 m/s^2 and Initial Vertical Velocity of 0 m/s were used.

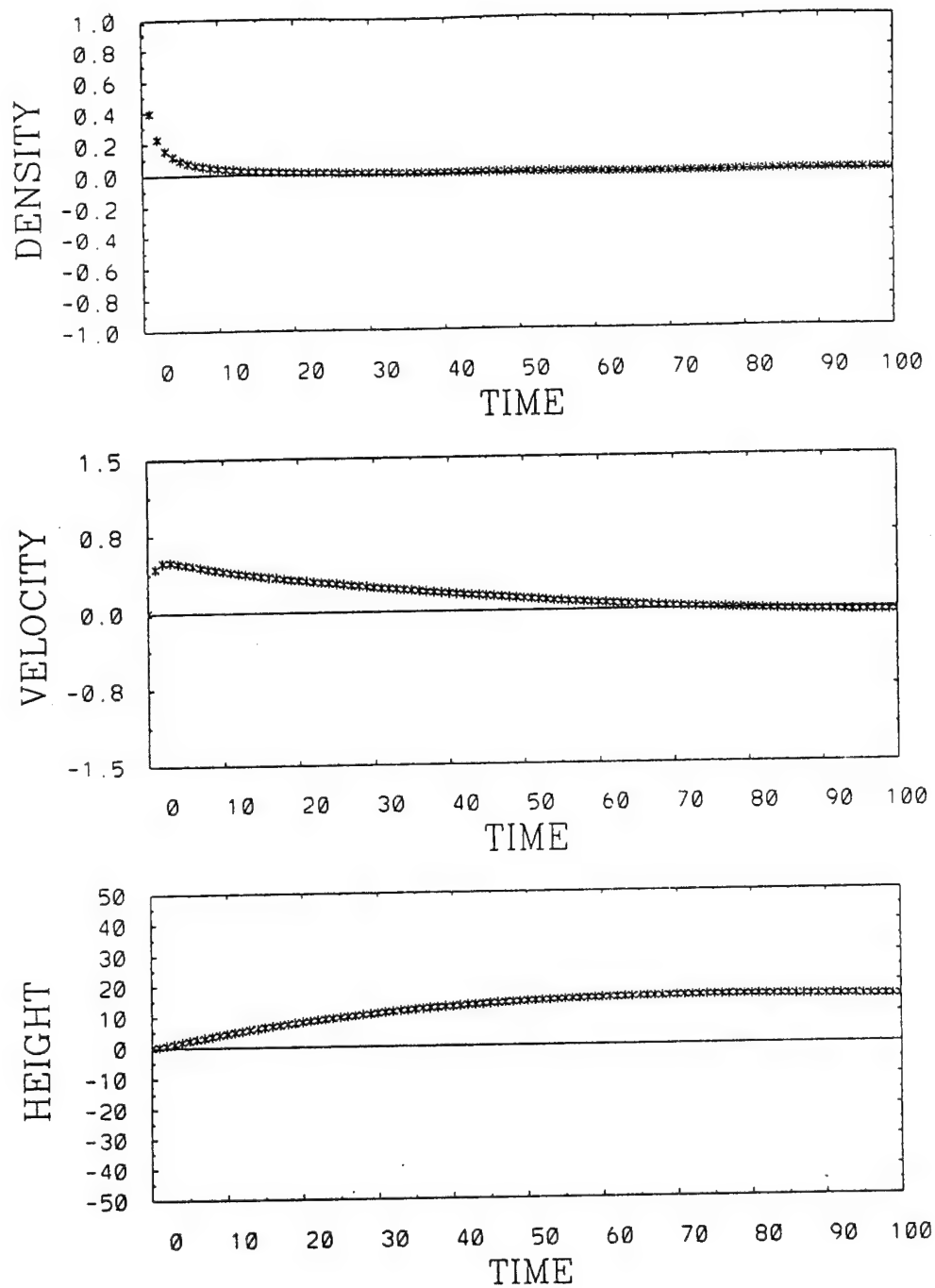


Figure 29. Time Variation of Buoyancy (m/s^2), Vertical Velocity (m/s), and Plume Height (m) in the Stable Condition ($N^2 = (0.408)^2$). Initial Buoyancy of 1 m/s^2 and Initial Vertical Velocity of 0 m/s were used.

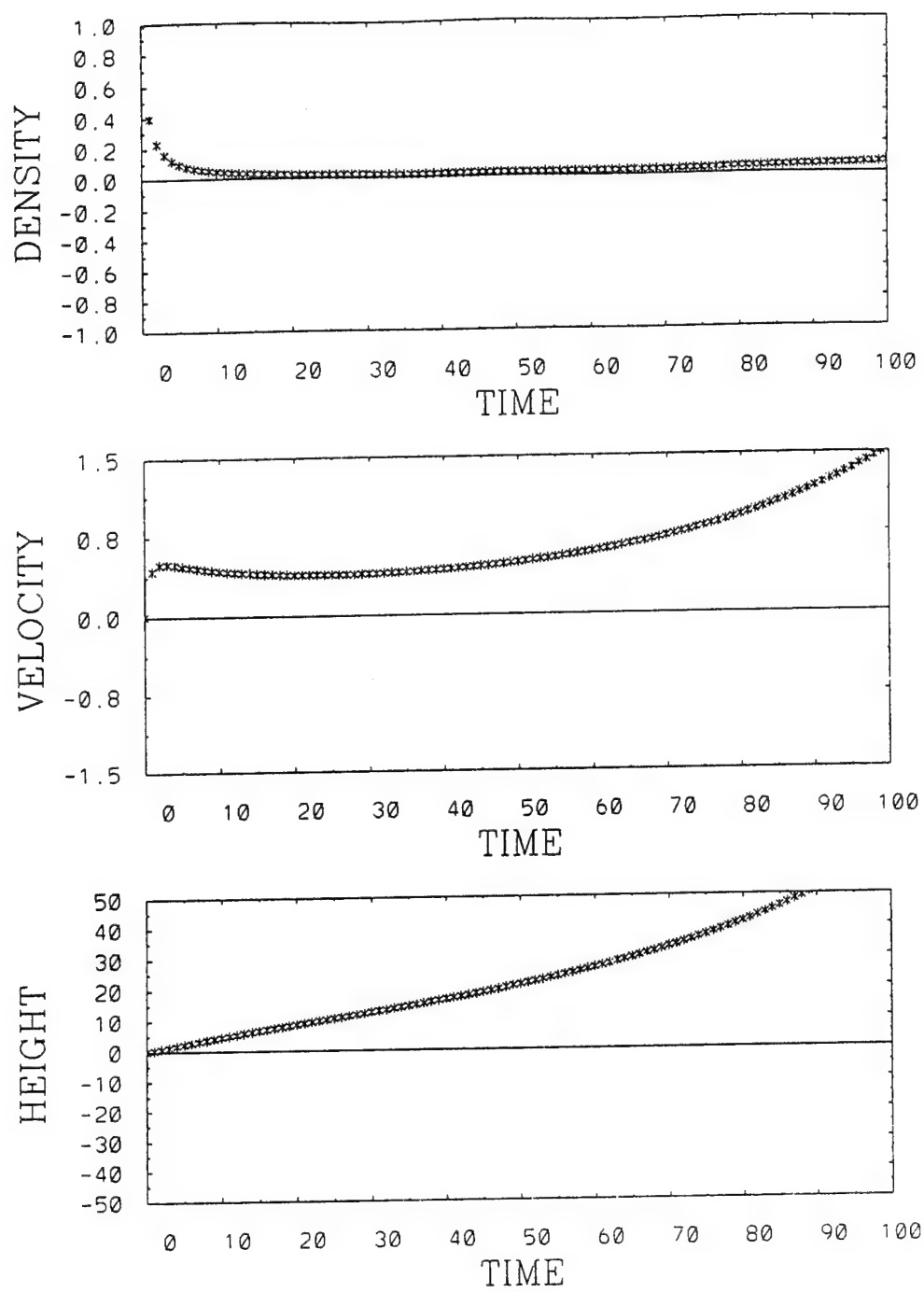


Figure 30. Similar to Figure 29 except in the Unstable Condition ($N^2 = -(0.408)^2$).

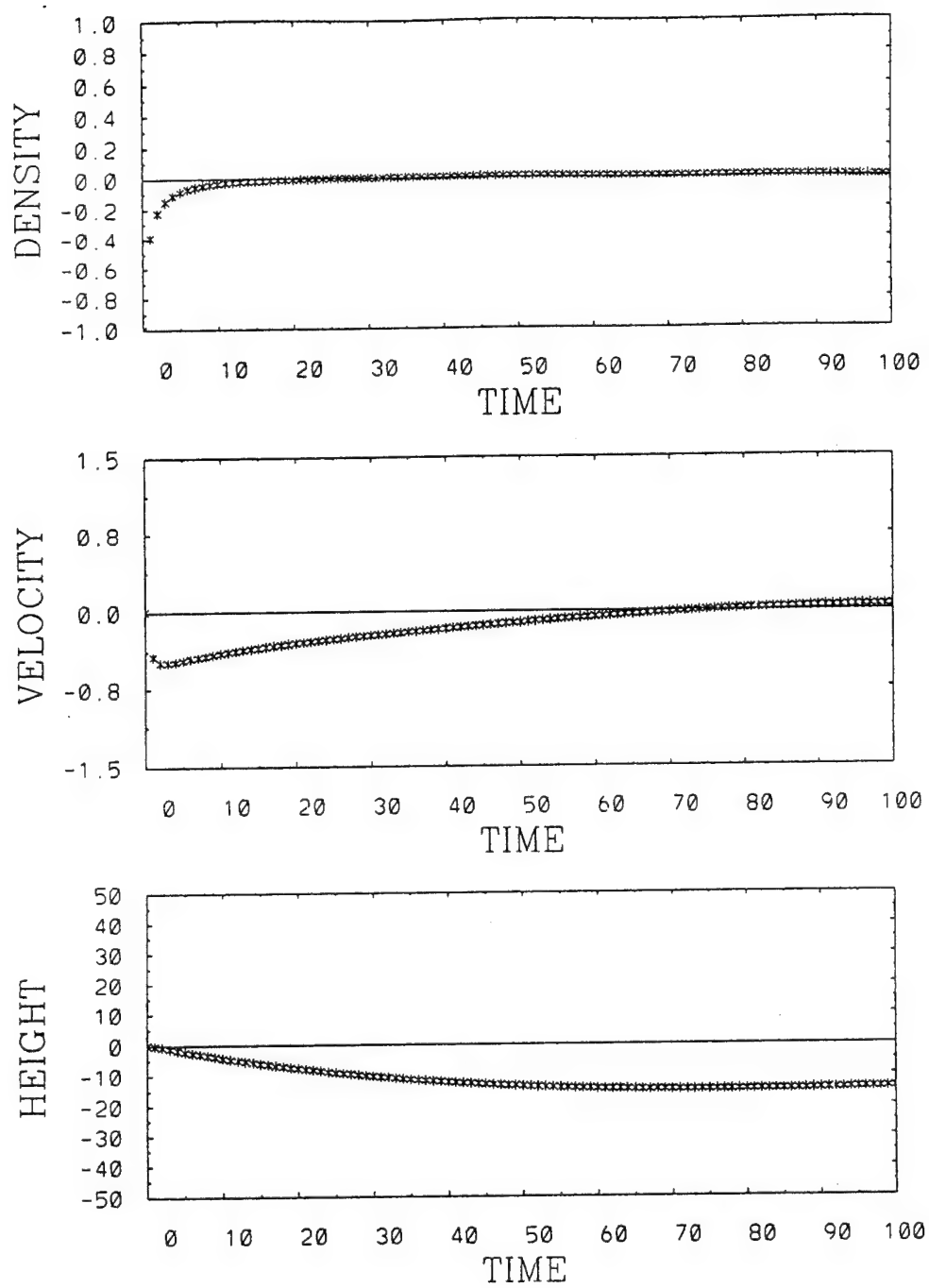


Figure 31. Similar to Figure 29 except Initial Buoyancy of -1 m/s^2 was used.

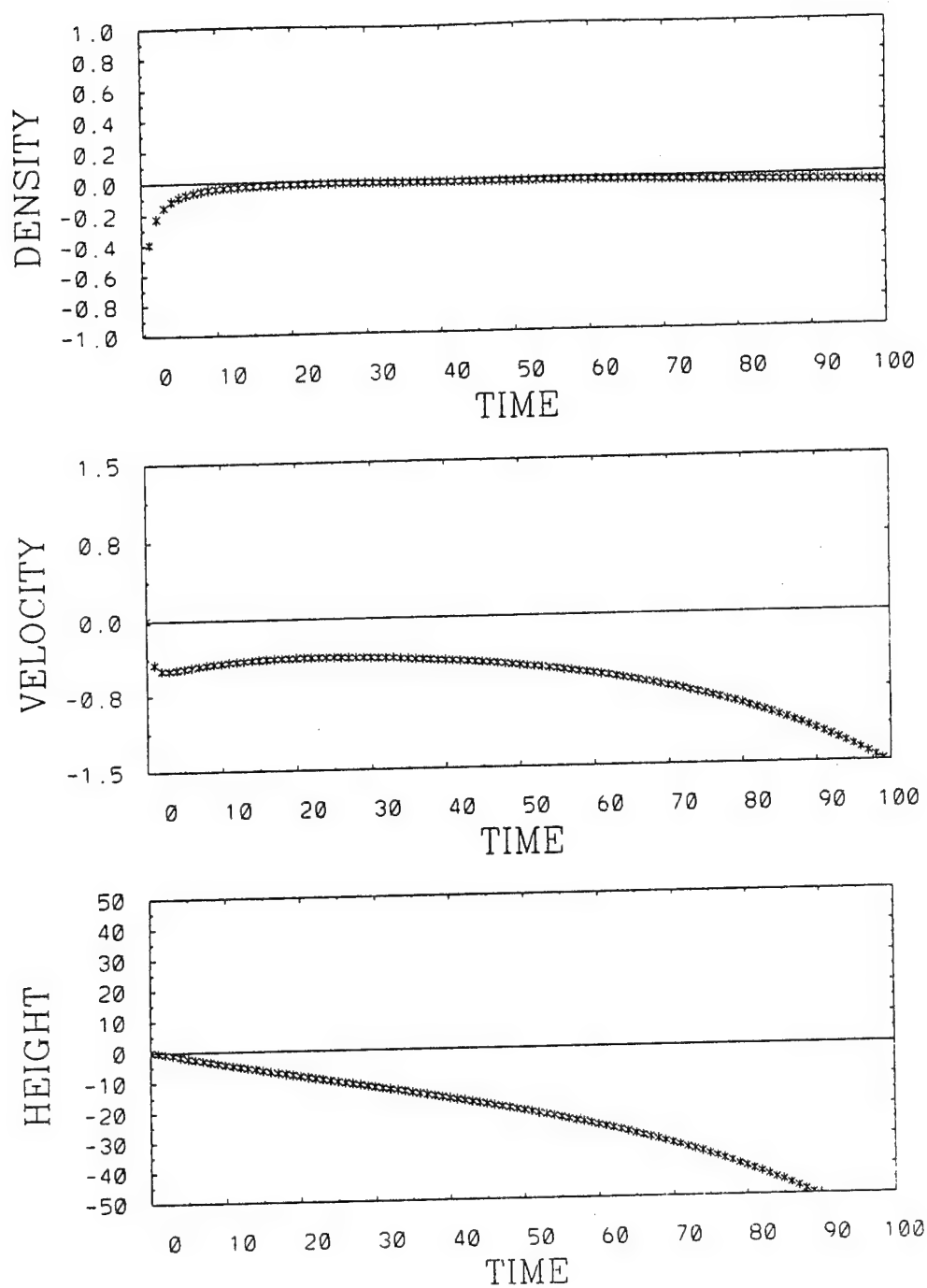


Figure 32. Similar to Figure 30 except Initial Buoyancy of -1 m/s^2 was used.

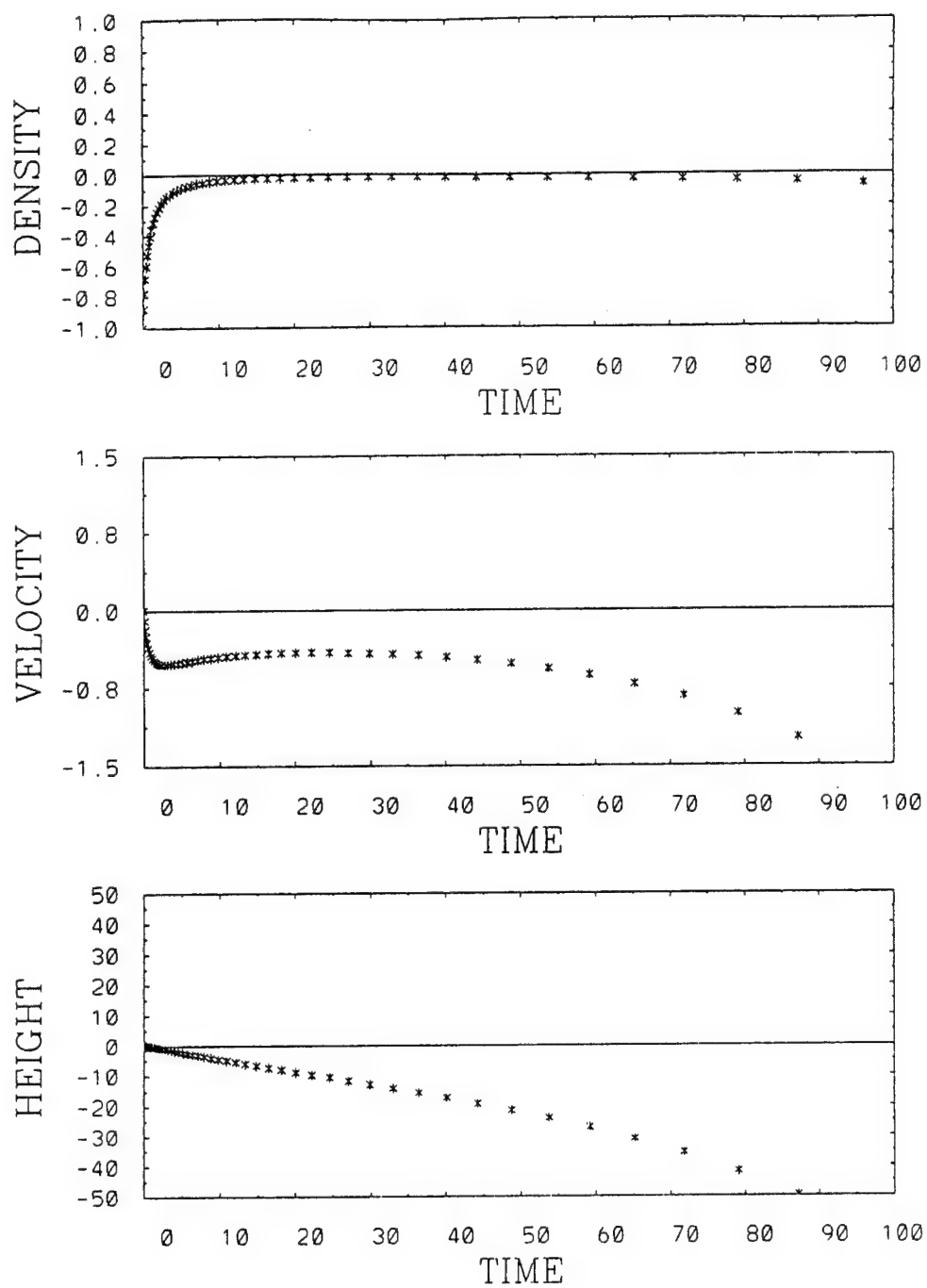


Figure 33. Similar to Figure 32 except Variable Integration Time Steps of 0.1 Seconds to 10 Seconds were used.

not only the mean but also the variance of concentrations are essential to determine the extent of a critical area where concentration values exceed specified limits. The size of a critical area becomes larger if a higher confidence level is required.

Natural variations of concentration could be large even with the use of 30- to 60-minute averaging times, which are used for the primary toxics at VAFB. The initial scope of this task was narrow, focusing on the specific question of how a required confidence level affects plume footprint size.

RAPTAD used an integration time step of 10 seconds, but concentrations were sampled every 120 seconds to reduce computational time. The current version of RAPTAD allows sampling at up to 50 stations.

Figures 34 through 36 show examples of time variations of mean concentration and ratios of standard deviation to mean values which are averaged over a time period of 15 minutes. These figures indicate that the standard deviation of concentration could be as large as several times the mean concentration, particularly near the plume edge. Although the ratios were at their minimum along the plume axis and increased rapidly toward the plume edge, both mean values and standard deviations were at their maximum along the plume axis and decreased toward the plume edge. Mean values decreased more rapidly than standard deviations, thus the ratios increased moving from the axis to the edge. Only a limited number of concentration fluctuation measurements are available for comparison. The best measurements were obtained by using wind tunnels. Preliminary comparisons indicate that our simulations are qualitatively in good agreement with wind tunnel data.² Both standard deviations, and ratios of standard deviation to mean, showed characteristics similar to those found in measurements where measured mean wind and turbulence were used in RAPTAD computation. No effort was made to compare simulations with atmospheric data because we are not aware of the existence of any such data.

² Lee, J.T., (Personal communication), 1990.

Time Variation of Concentration Station : B

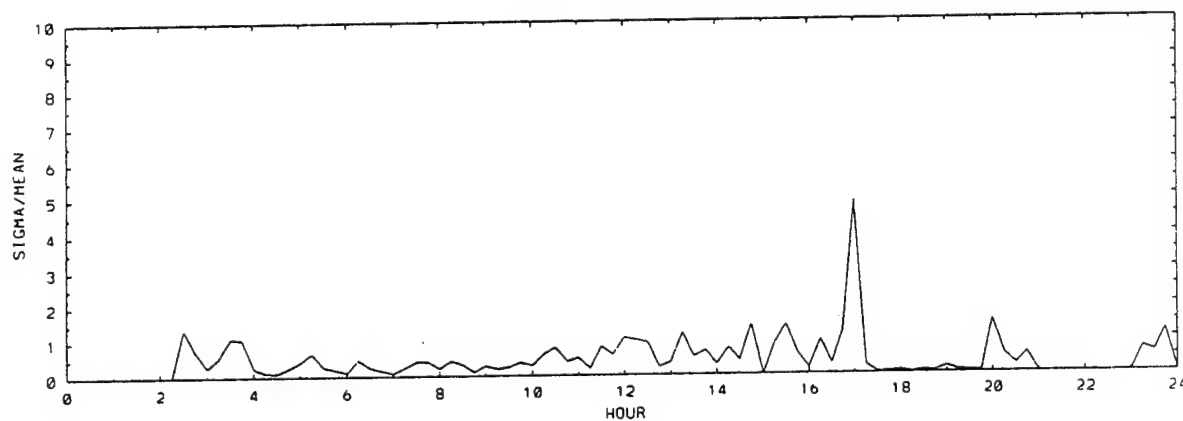
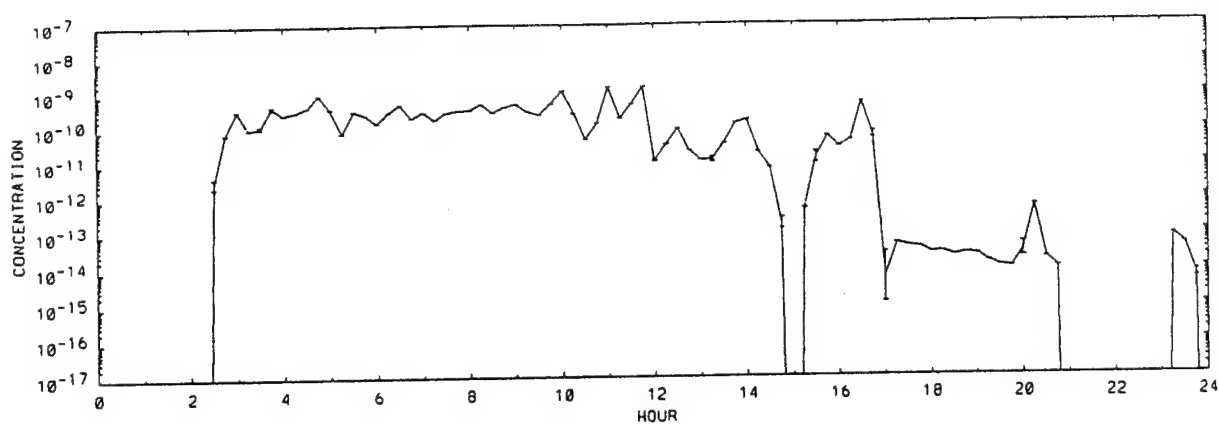


Figure 34. Examples of Time Variations of Mean Concentration (Top) and Ratio of Standard Deviation to Mean Concentration at Station B.

Time Variation of Concentration Station : C

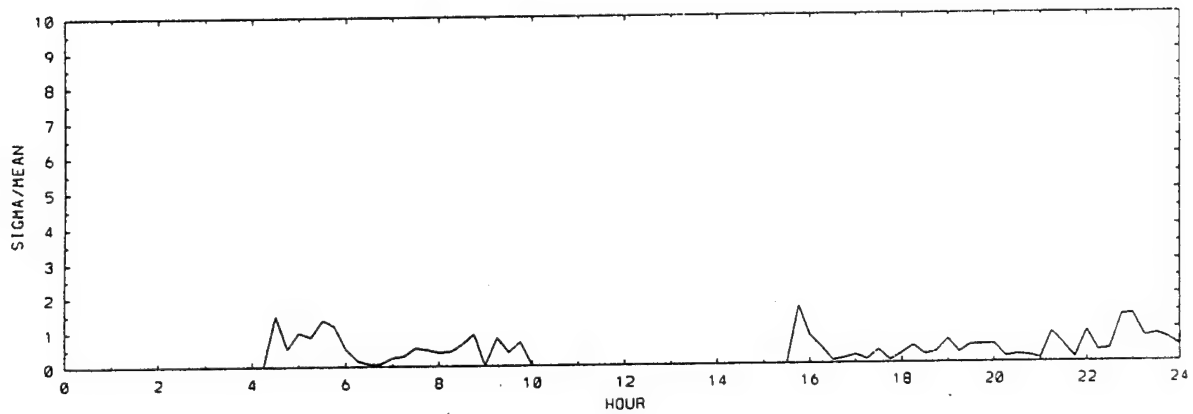
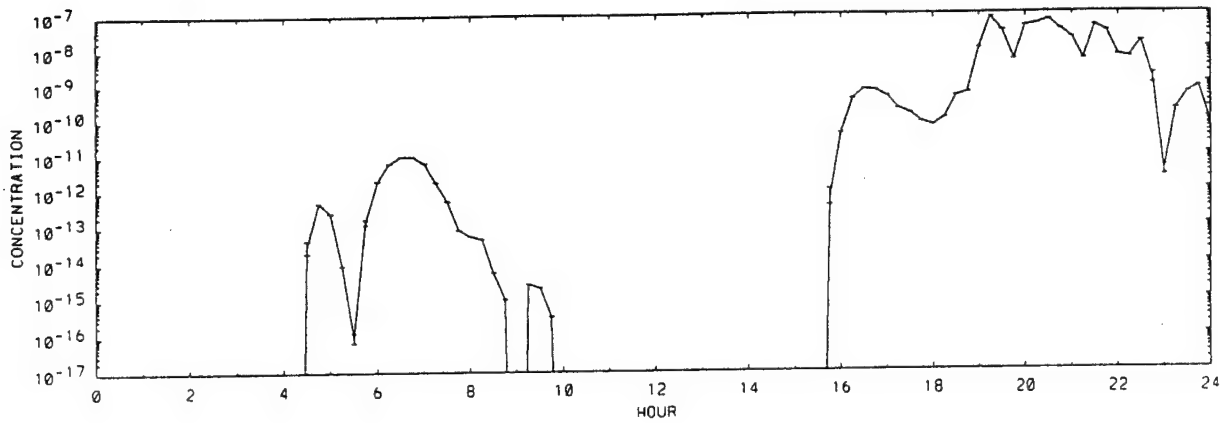


Figure 35. Similar to Figure 34 except at Station C.

Time Variation of Concentration Station : I

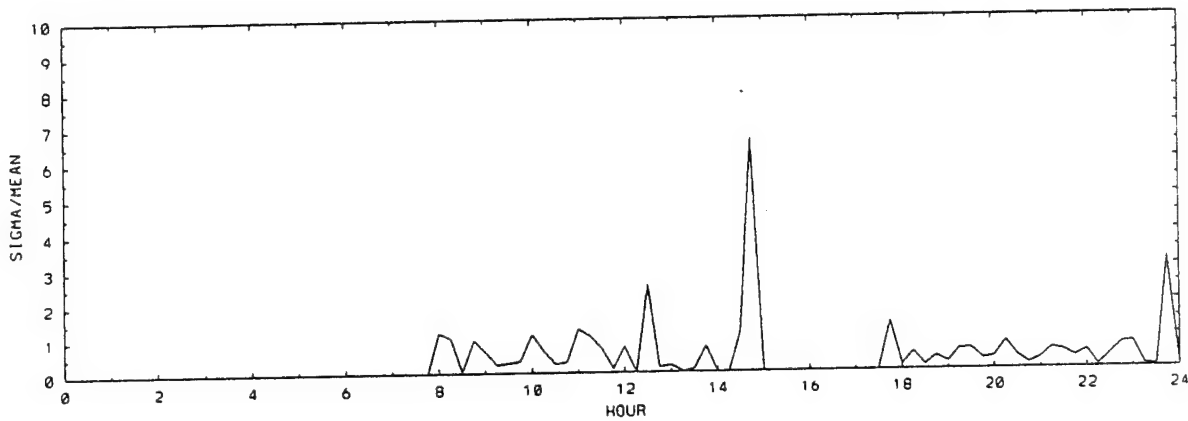
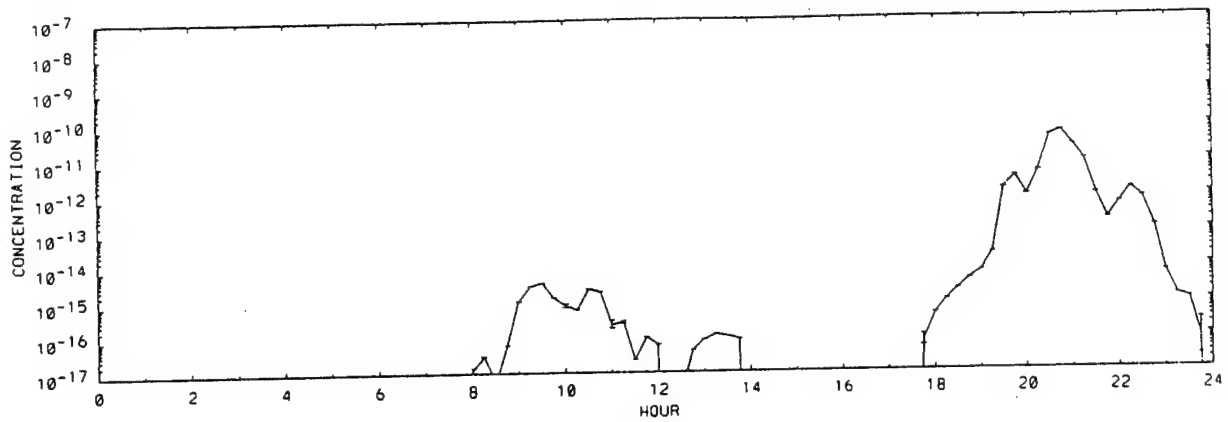


Figure 36. Similar to Figure 34 except at Station I.

G. TASK 7: *Perform model verification runs with a nested grid version of HOTMAC on a workstation.*

A nested grid version of HOTMAC had been used with a Cray supercomputer, but it had never been used with a workstation because it would require too much computer time. However, with the rapid advancement of workstation performance, a nested grid version of HOTMAC can now be run on a workstation.

Test simulations were performed to demonstrate systematically how nested grids improved the simulation of wind distributions. Three nested grids were used in a control run. Horizontal grid spacings (in both X and Y directions) were 500 meters, 2000 meters, and 8000 meters for the innermost grid (Grid 3), intermediate grid (Grid 2), and the outer grid (Grid 1), respectively. The number of grids used in the horizontal directions were 32 X 32, 16 X 16, and 8 X 8, respectively for Grid 3, Grid 2, and Grid 1. Each grid had 16 vertical levels.

Simulations began at 0600 LT on a mid-August day (arbitrarily chosen) and continued for 24 hours. A two-way nesting method was used: the outer grid provided boundary values to the inner grid, and the inner grid updated outer grid values with new values at grid points common to both grids.

Figure 37 shows 1500 LT wind vector distributions at 6 meters agl at 1500 LT where grid spacings in the horizontal directions are 8 kilometers. Areas enclosed by dashed lines indicate nested grids. Figures 38 and 39 show wind distributions for Grid 2 and Grid 3. As expected, more variations in space were simulated when grid spacing decreased to 2 kilometers (Figure 38) and 500 meters (Figure 39). Wind direction was northwesterly and wind speed was 3 m/s in the levels above the boundary layer. Wind directions in the surface layer show considerable variations due to nonhomogeneous temperature distributions over complex terrain. Sea-breeze and upslope flows were clearly seen in Grid 3 (Figure 39).

Wind directions in the surface layer vary considerably with time. Figure 40 shows next morning 0200 LT wind distributions at 6 meters agl in the Grid 1 computational domain (64

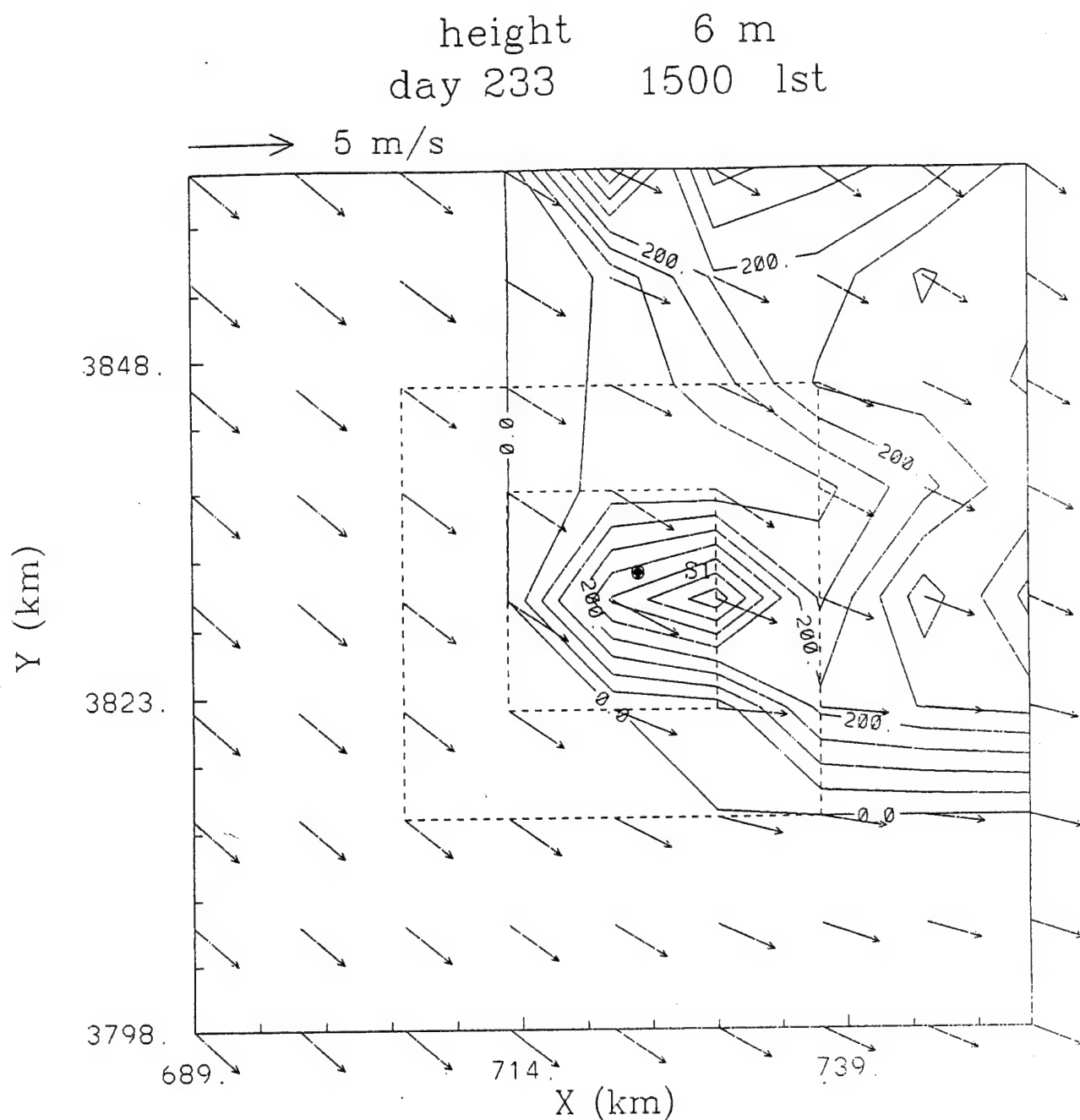


Figure 37. Wind Distributions at 6 Meters agl at 1500 LT on Day 233. Arrows indicate Wind Vectors, whose Scale is shown at the Left Upper Corner. Solid Lines indicate Ground Elevation Contours in increments of 50 Meters. Areas enclosed by Dashed Lines show Nested Grids. Computation Domains are referred to as Grid 1, Grid 2, and Grid 3 for the Outer, Intermediate, and Inner Grids, respectively.

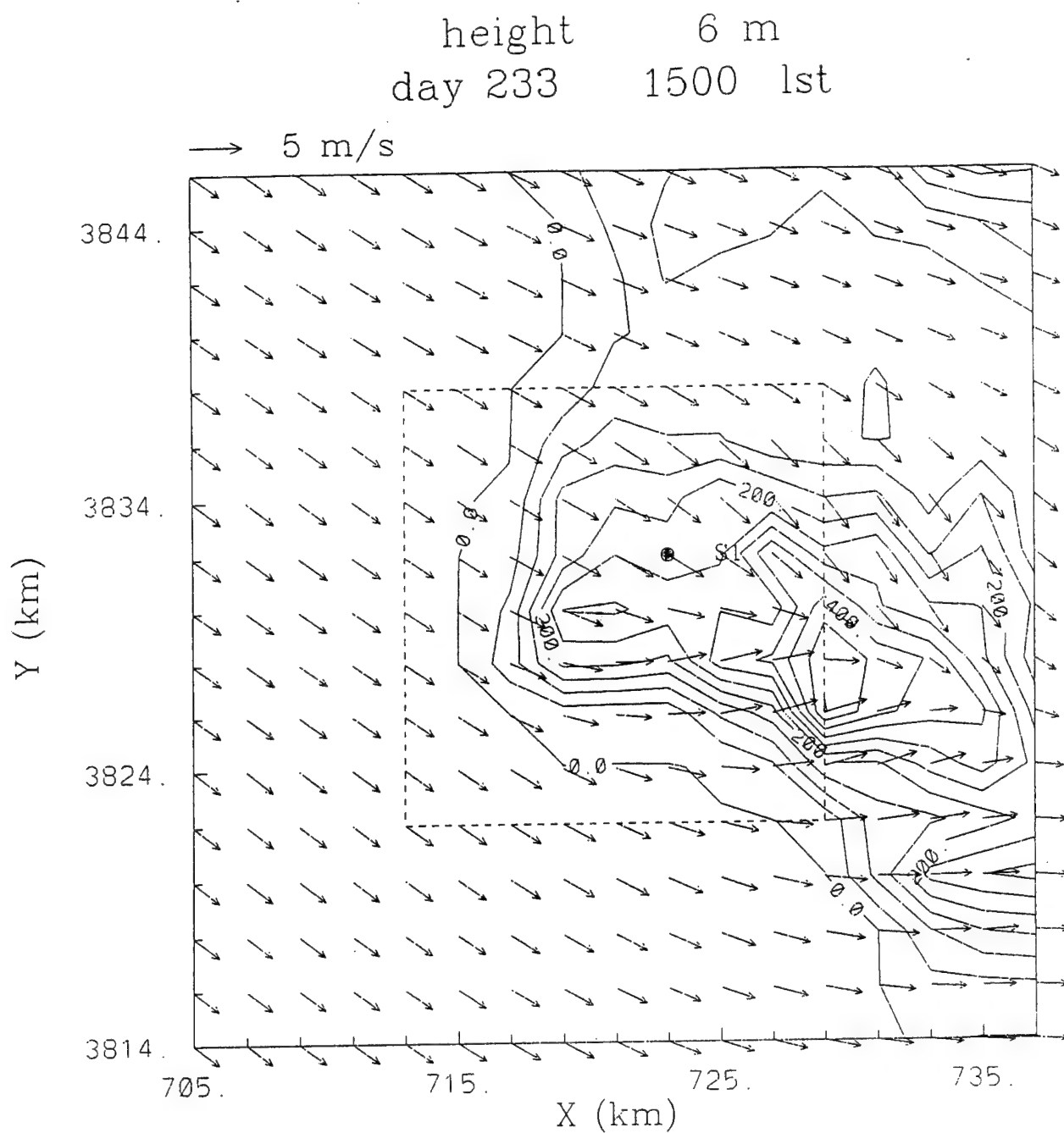


Figure 38. Similar to Figure 37 except Showing Grid 2. The Area enclosed by the Dashed Lines shows the Grid 3 Domain.

height 6 m
day 233 1500 1st

→ 5 m/s

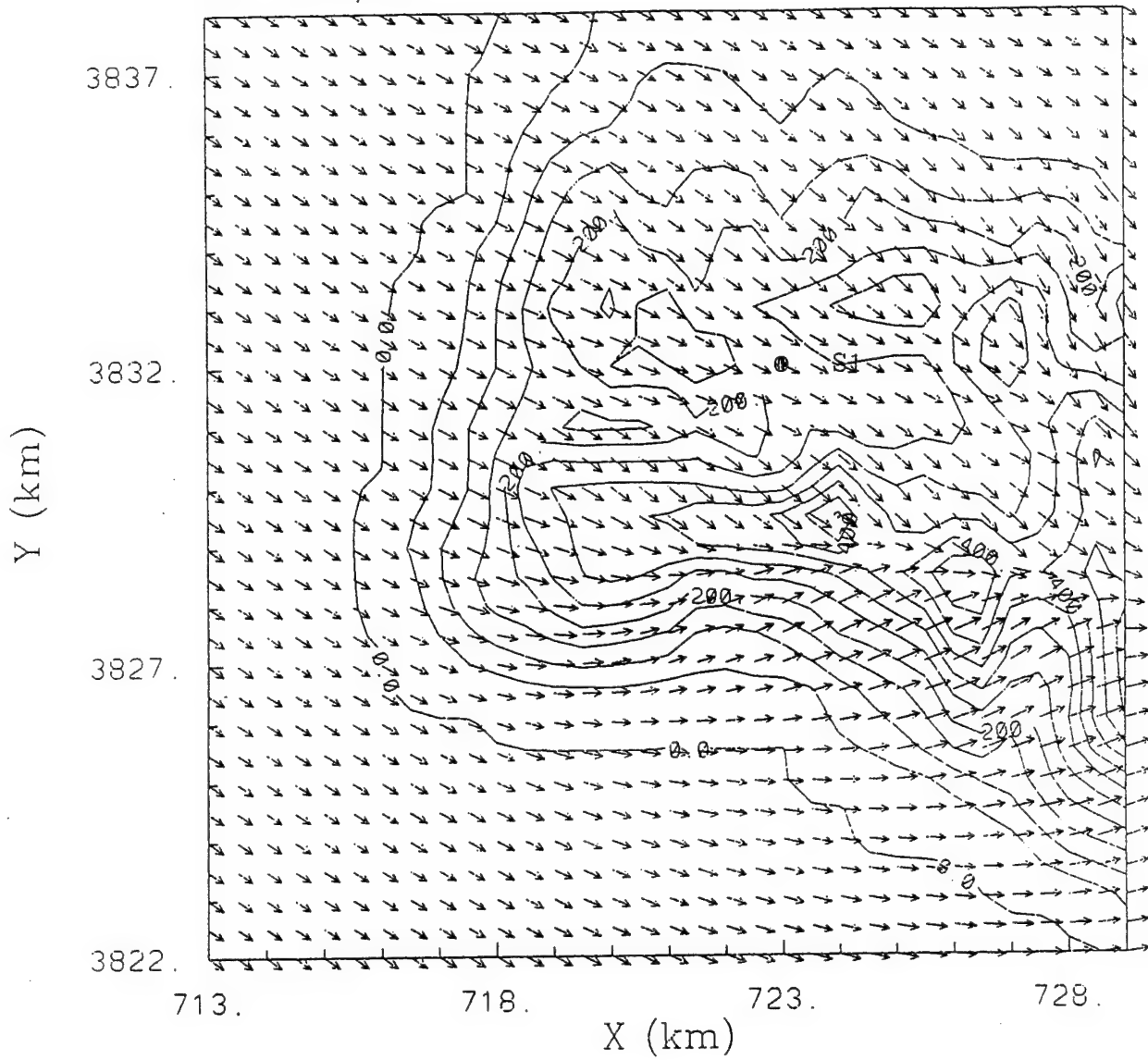


Figure 39. Similar to Figure 37 except showing Grid 3.

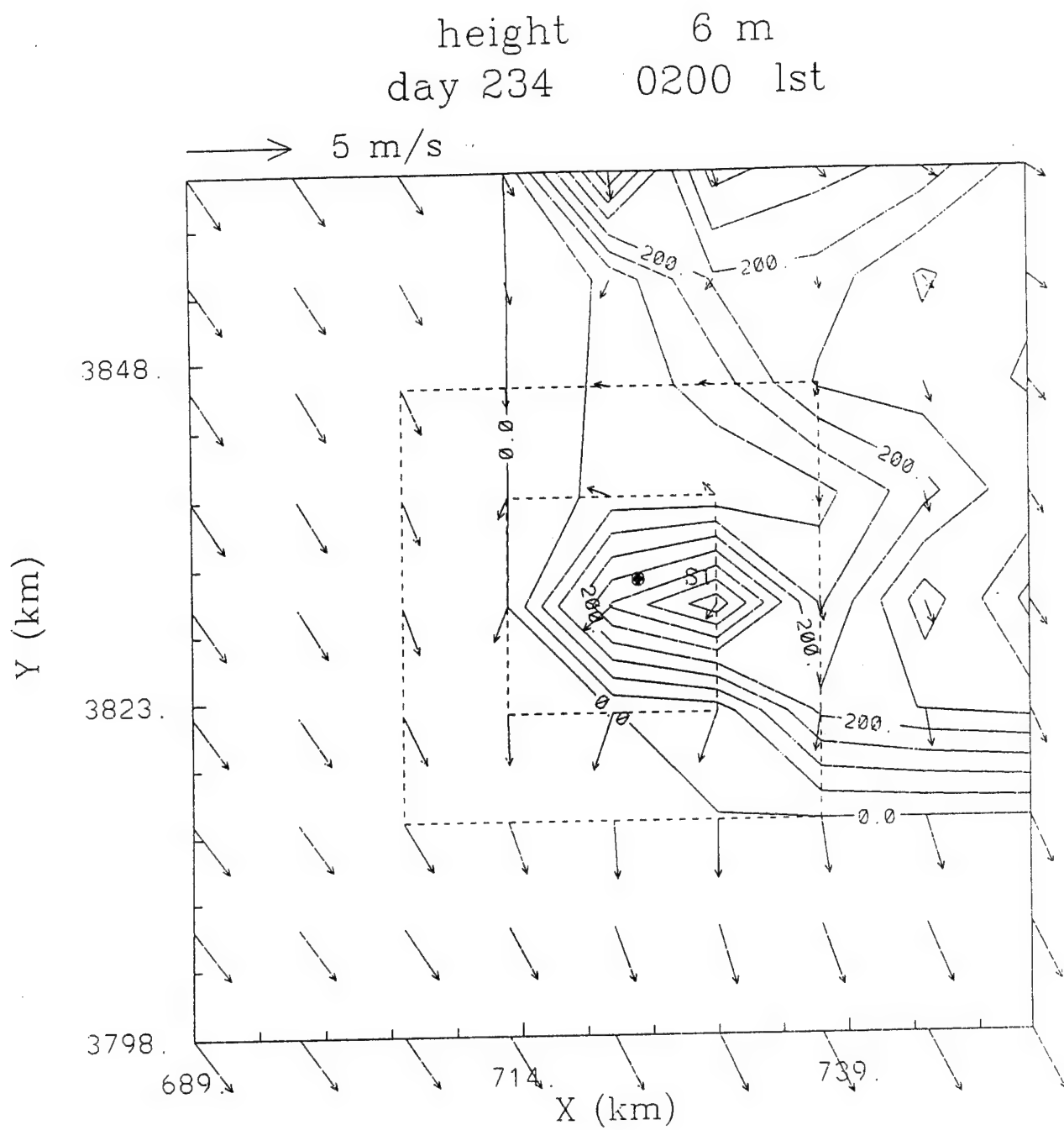


Figure 40. Similar to Figure 32 except at 0200 LT on Day 234.

kilometers X 64 kilometers), where the grid spacing was 8 kilometers. Figures 41 and 42 show corresponding wind distributions over the Grid 2 and Grid 3 computational domains. Sea breezes were replaced by land breezes, and upslope flows were replaced by downslope flows. These variations are common in coastal complex-terrain areas, provided that synoptic wind forcing is small.

Figures 43 through 46 show wind distributions where only two grids were used, in comparison with the control run, where three grids were used. The innermost grid of the control run was omitted. Figures 43 and 44 are control run counterparts of Figures 37 and 38, respectively. Atmospheric turbulence was significant, due to strong heating from the ground and enhanced momentum transfer in the vertical direction. This resulted in relatively uniform wind distributions in space. On the other hand, turbulence mixing was at a minimum during the nocturnal period, due to stable density stratification created by radiation cooling at the ground. Thus, winds in the surface layer were often decoupled from the winds in the upper levels. Figures 45 and 46 are 0200 LT wind distributions at 6 meters agl where two grids were used. Figures 45 and 46 are control run counterparts of Figures 40 and 41. There are noticeable differences in the wind distributions between the three-grid (control) and two-grid runs, particularly in the areas where Grid 3 was nested in the control run.

Finally, simulations were conducted without a nested grid. Figures 47 and 48 show 1500 LT and 0200 LT wind distributions at 6 meters agl. Wind distributions at 1500 LT (Figure 47) are similar to those for the control run (Figure 37) because of strong mixing in the vertical direction, due to turbulence, which resulted in almost uniform wind distributions. On the other hand, wind distributions at 0200 LT (Figure 48) are considerably different from those for the control run (Figure 40), particularly in the area where Grid 3 was nested.

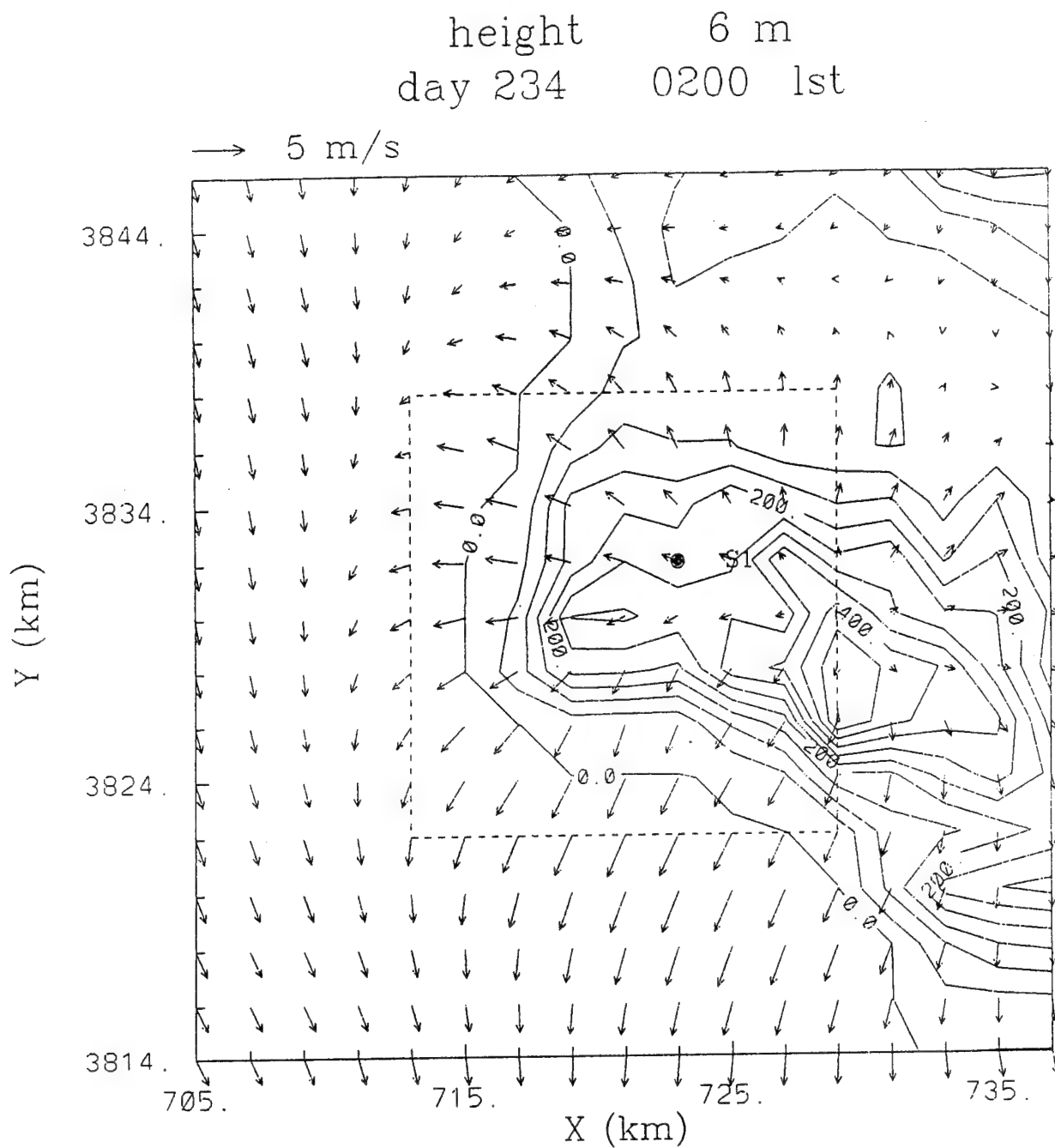


Figure 41. Similar to Figure 40 except showing Grid 2. The Area enclosed by the Dashed Lines shows the Grid 3 Domain.

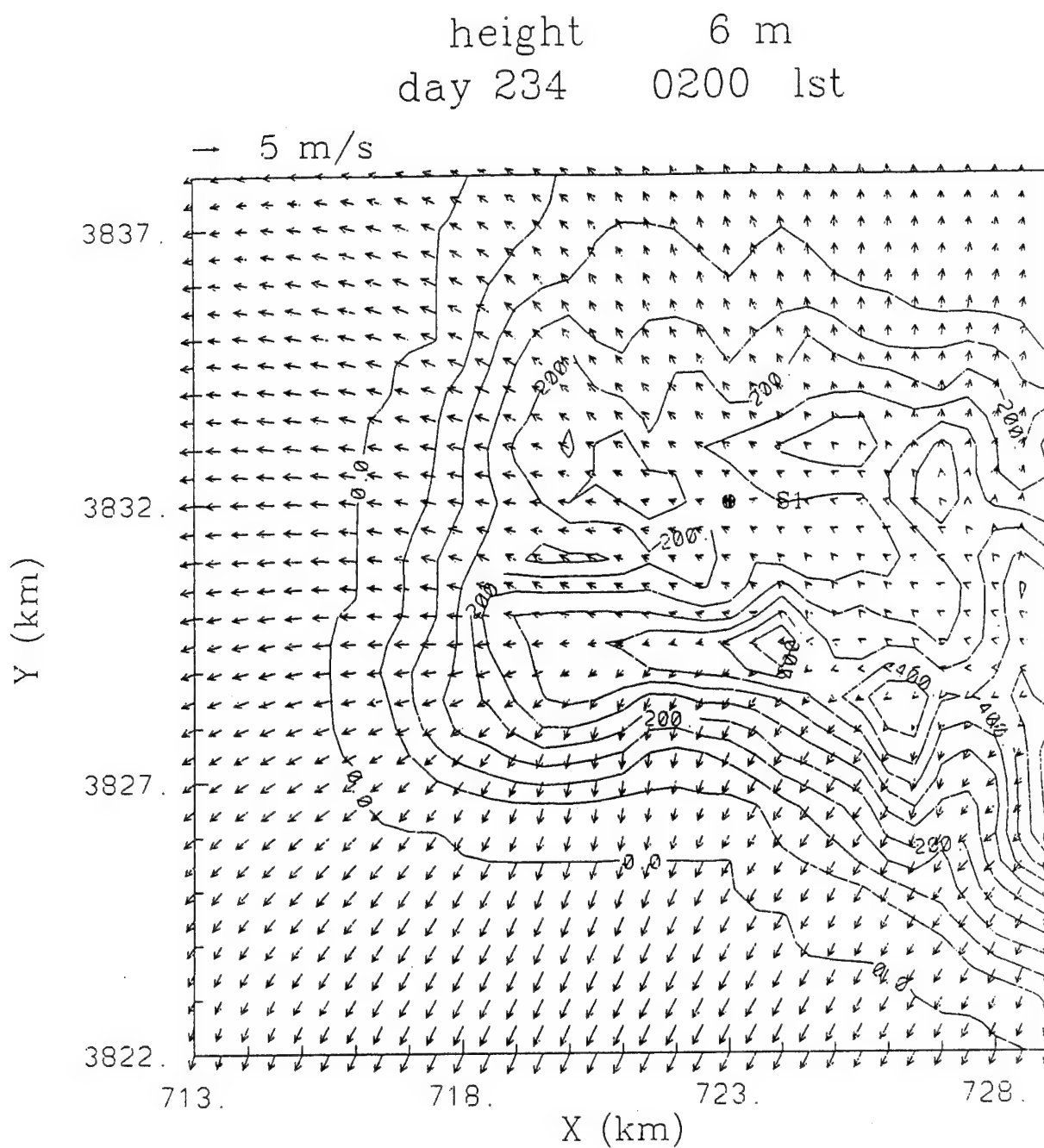


Figure 42. Similar to Figure 40 except showing Grid 3.

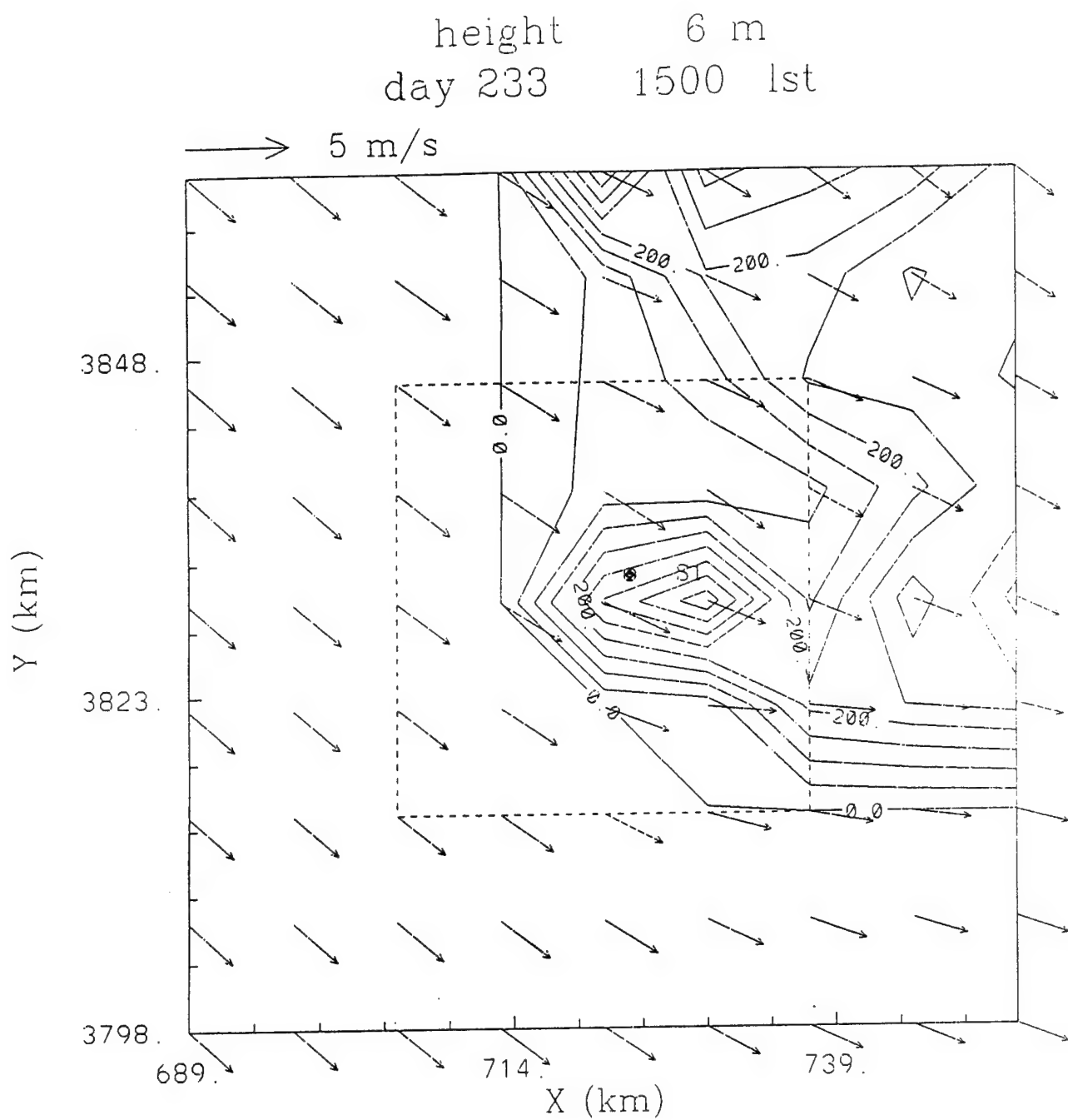


Figure 43. Similar to Figure 37, but using only Grid 1 and Grid 2.

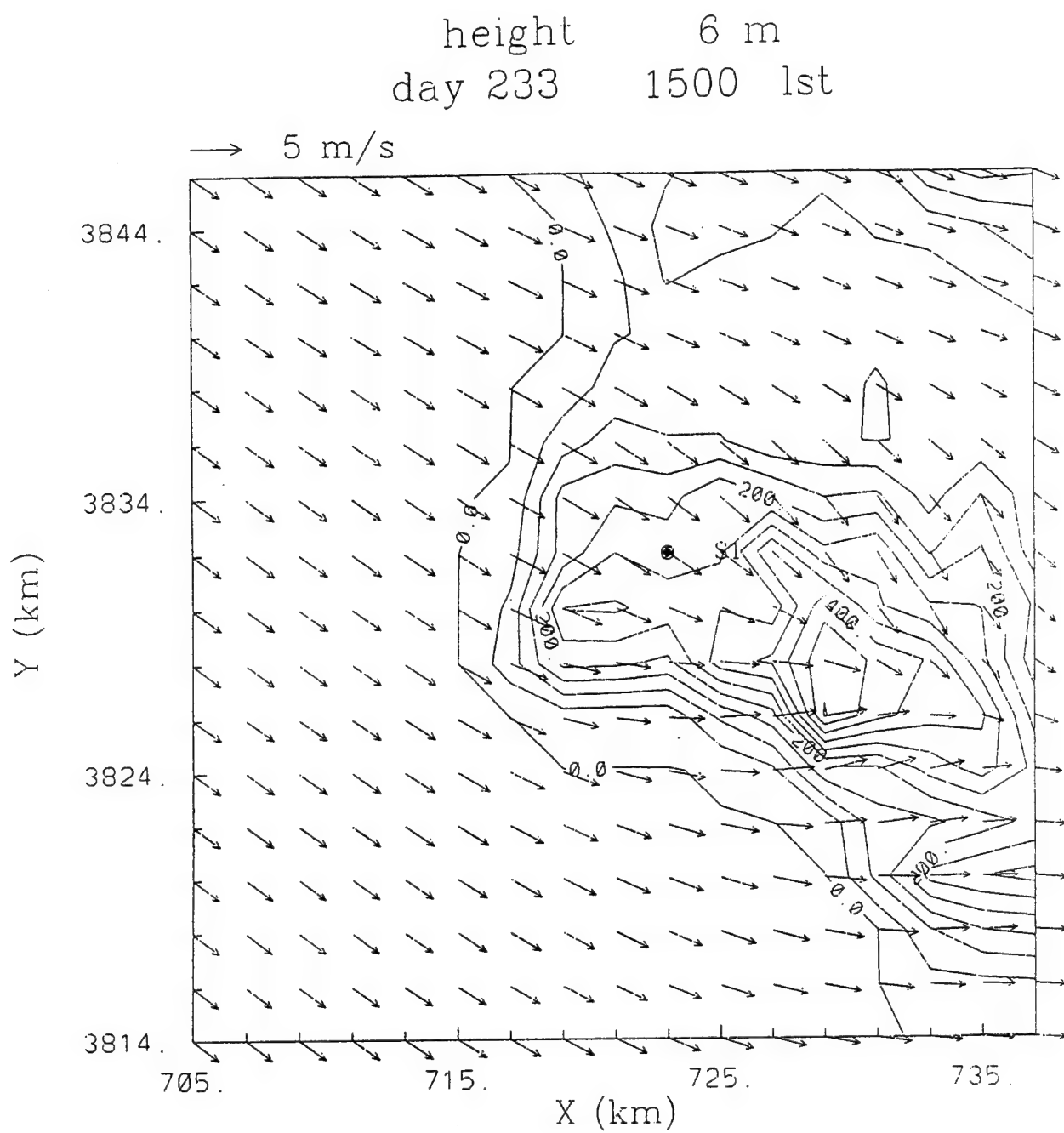


Figure 44. Similar to Figure 38, but using only Grid 1 and Grid 2.

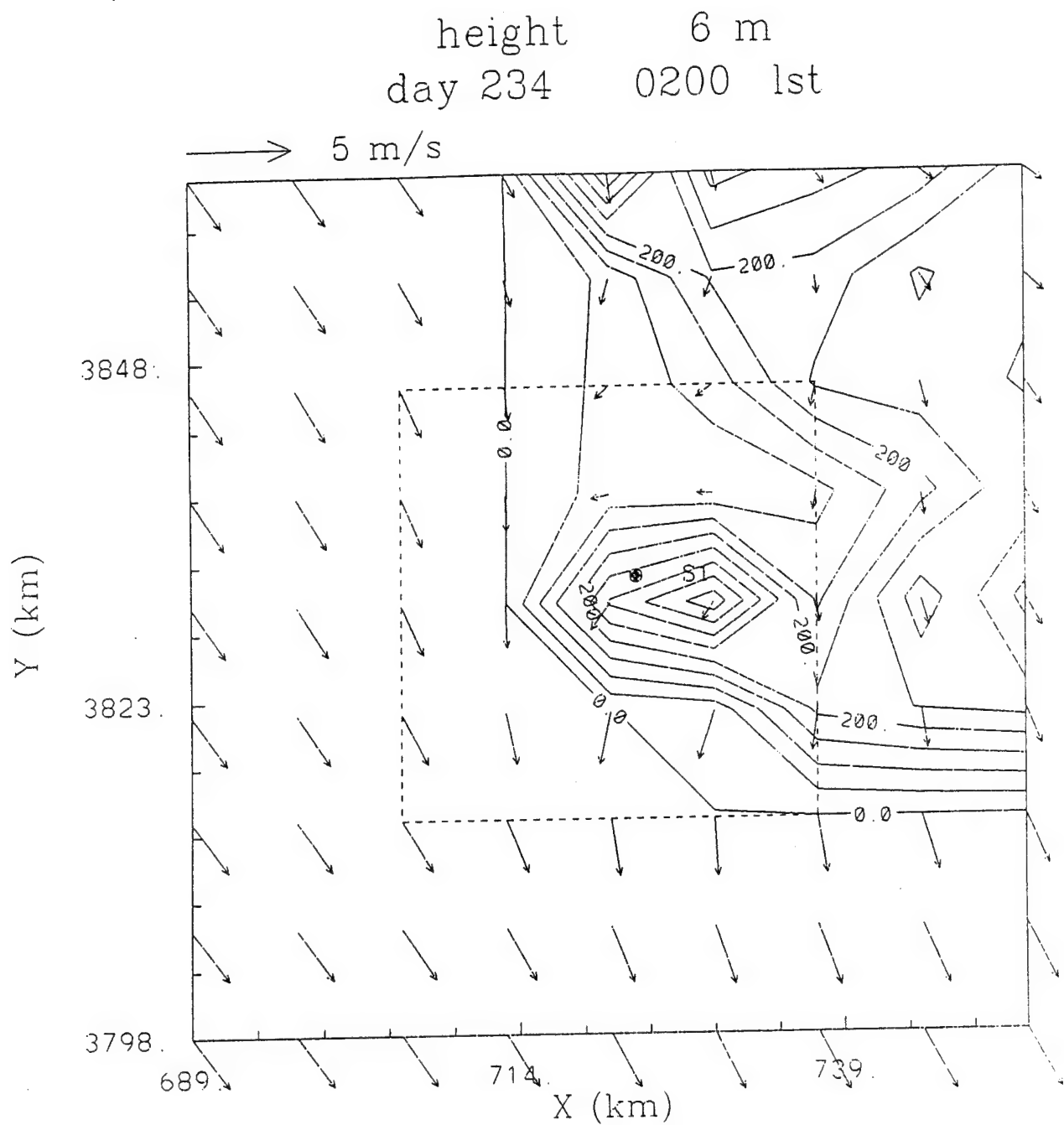


Figure 45. Similar to Figure 40, but using only Grid 1 and Grid 2.

height 6 m
day 234 0200 1st

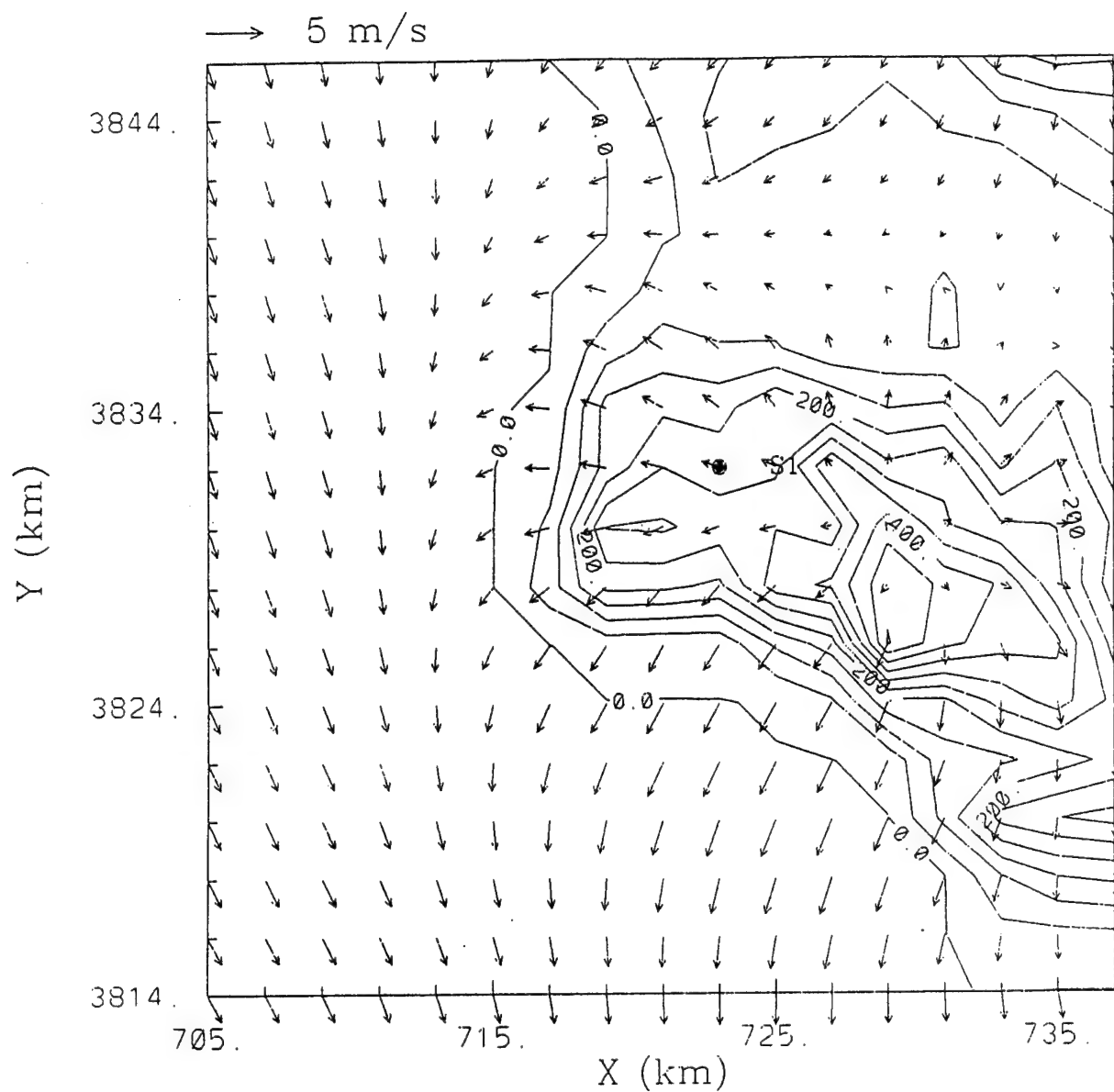


Figure 46. Similar to Figure 41, but using only Grid 1 and Grid 2.

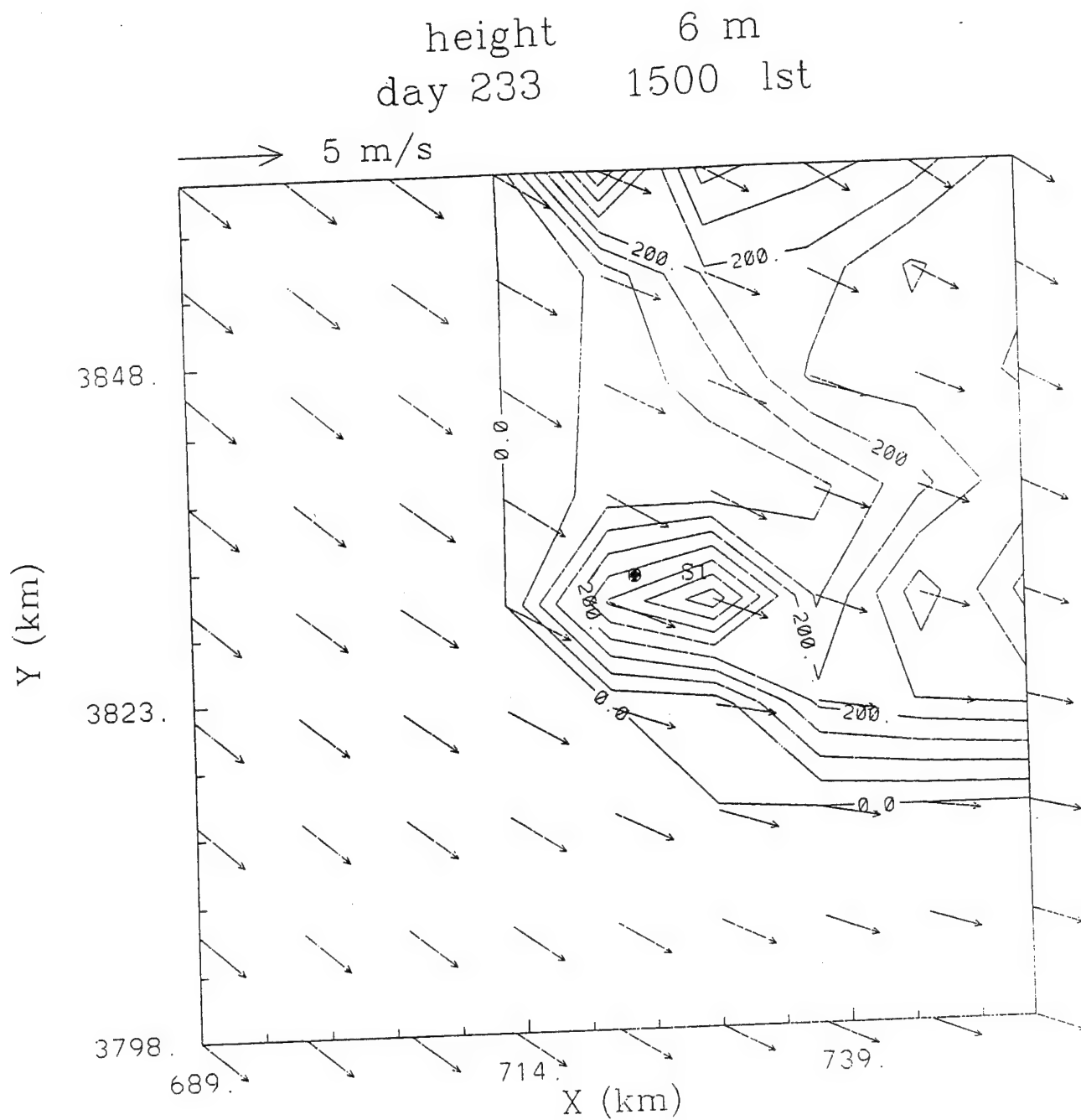


Figure 47. Wind Distributions at 6 Meters agl at 1500 LT on Day 233. Similar to Figures 37 and 43, but without a Nested Grid.

height 6 m
day 234 0200 1st

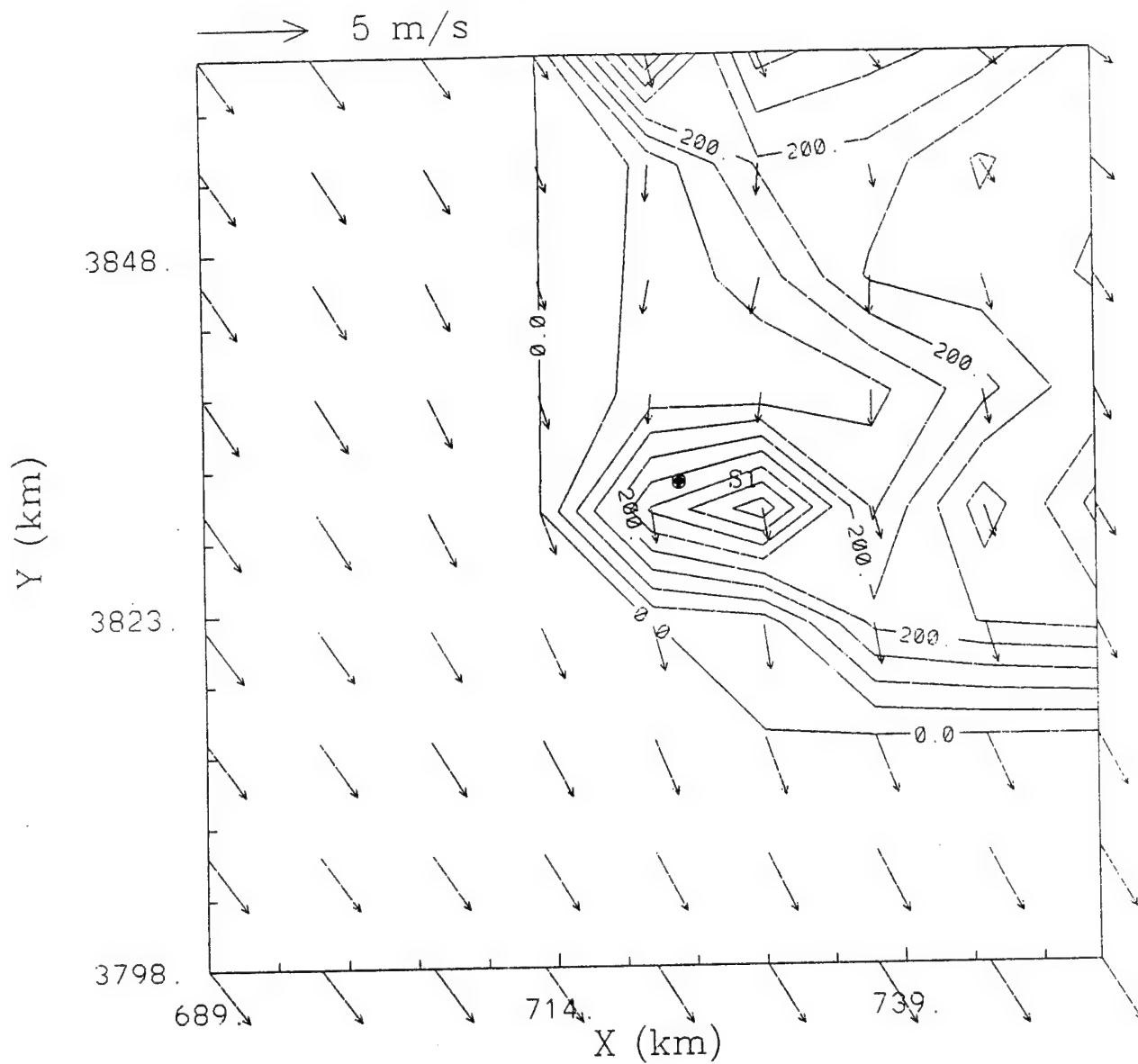


Figure 48. Similar to Figure 47, except at 0200 LT on Day 234.

H. TASK 8: *Upgrade computer capabilities used for emergency response modeling at VAFB.*

HOTMAC and RAPTAD have been run on several workstations produced by leading computer companies, including Sun Microsystems, Silicon Graphics, Data General, Hewlett-Packard, and Digital Data Corporation. We have developed a user-friendly menu system which includes a variety of graphic displays for the Sun Microsystems and Silicon Graphics workstations. We rewrote our interface and graphics software for the Sun's OpenLook window.

We performed the first half of this project with YSA computer equipment in order to: (1) fully coordinate the feasibility and support for installation of a suggested workstation at VAFB, and (2) take advantage of any performance gains which might become available during the first half of the project period.

Based on discussions between the personnel at VAFB and YSA, the following computer hardware and software were selected:

1. A Sun SPARCstation 10 with 32 Mb RAM, 19" color monitor, 400 Mb internal SCSI disk, 1.44 Mb 3 $\frac{1}{2}$ " internal floppy disk.
2. A 1.2 Gb external disk.
3. A 150 Mb tape drive.
4. A CD drive.
5. Sun FORTRAN compiler.
6. Sun C compiler.
7. NCAR Graphics.

Hardware and software were installed and tested at YSA, and delivered to VAFB.

SECTION IV

CONCLUSION AND RECOMMENDATIONS

A. CONCLUSION

- It is feasible to operate, on a workstation, a nested-grid, three-dimensional atmospheric model, HOTMAC, and a three-dimensional dispersion model, RAPTAD, to forecast the transport and diffusion of airborne materials at VAFB.
- The computer capabilities for emergency response applications at VAFB were upgraded. HOTMAC and RAPTAD were installed and tested on a Sun SPARCstation10.
- HOTMAC was modified to run continuously and store wind and turbulence forecasts for the next 24 hours. When an emergency occurs, RAPTAD can be used immediately with the wind data stored on disk. The RAPTAD computation is much faster than that of HOTMAC. Thus, this approach meets better the time constraints of emergency situations.
- A method was developed to integrate large-scale weather data into HOTMAC. The weather data are used to initialize and correct HOTMAC forecasts. A four-dimensional data assimilation method was used.
- A method was developed to predict concentration variances which can be used to estimate uncertainties associated with predictions.
- Model physics was added to simulate fog formation and dissipation. Fog is frequently observed at VAFB and affects the heat energy balance at ground level.
- Positive and negative buoyancy effects of plumes were incorporated into RAPTAD.

B. RECOMMENDATIONS

- Become familiar with the background theories and operating procedures of HOTMAC and RAPTAD. Increase experience by running the models under different weather conditions.

- Consider customizing pre- and post- processors of HOTMAC and RAPTAD to meet specific needs at VAFB. The current versions of HOTMAC and RAPTAD are designed for general applications.
- Continue to upgrade computer capabilities at VAFB. Computer hardware technology is expected to advance further and to allow much more sophisticated models to be operated in much less time than previously considered possible.
- Continue to improve the model physics of HOTMAC and RAPTAD. These codes have model physics which is considered to be the state-of-the-science, but falls short of replicating the complex physics in the real atmosphere. In particular, we strongly recommend that the new model physics added here (precipitation microphysics, radiation transfer in fog and clouds, and positive and negative plume buoyancy effects) be tested further by comparing simulations with observations.

REFERENCES

1. Stephens, J. B. and Stewart, R. B., Rocket Exhaust Effluent Modeling for Tropospheric Air Quality and Environmental Assessments, NASA TR R-473, 1977.
2. Bowman, C. R. and Bjorklund, J. R., User's Manual for the REEDM Computer Program for Launches at Vandenberg Air Force Base, vols. 1 and 2, H. E. Cramer Company Technical Report TR-85-157-01, Prepared for Department of the Air Force, Eastern Space and Missile Center/AFSC, Patrick AFB, Florida, 1985.
3. Haugen, D. A. and Fuquay, J. J., Editors, The Ocean Breeze and Dry Gulch Diffusion Programs, vols. 1 and 2, AFCRL-63-791 (I, II), Air Force Cambridge Research Laboratories, Hanscom AFB, MA, 1963.
4. Hinds, W. T. and Nickola, P. W., The Mountain Iron Diffusion Program: Phase I South Vandenberg: Volume I, vol. I, AFWTR-TR-67-1, BNWL-572, AEC Research Development Report, Pacific Northwest Laboratory, Richland, WA, 1967.
5. Hinds, W. T. and Nickola, P. W., The Mountain Iron Diffusion Program: Phase I South Vandenberg: Volume II, vol. II, AFWTR-TR-67-1, BNWL-572, AEC Research Development Report, Pacific Northwest Laboratory, Richland, WA, 1968.
6. Daubek, H. G., Dotson, W. L., Ramsdell, J. V., and Nickola, P. W., The Mountain Iron Diffusion Program, Phase II: South Vandenberg, vol. III, AFWTR-TR-67-1, BNWL-572 (III) UC-53, Pacific Northwest Laboratory, Richland, WA, 1969.
7. Kunkle, B. A., User's Guide for the Air Force Toxic Chemical Dispersion Model (AFTOX), AFGL-TR-88-0009, Hanscom AFB, MA, 1988.
8. Conley, K., Haber, J., Hudson, J., Nyman, R., Philipson, L., and Ting, D., Requirement for Predicting Toxic Dispersion at the Western and Eastern Test Ranges, vols. I and II, ACTA Report No. 90-229/33-03 & 236/05-01, ACTA Inc., 24430 Hawthorne Blvd., Torrance, CA 90505, 1990.
9. Hunter, S. M., Winds on Critical Streamline Surface (WOCSS) Model - An Evaluation Using Vandenberg AFB Terrain and Meteorological Data, Riso National Laboratory, Denmark, 1988.

10. Ludwig, F. and Endlich, R., User's Guide for the Winds on Critical Streamline Surfaces (WOCSS) code, Prepared for U.S. Army Atmospheric Sciences Laboratory, White Sands, SRI International, 1988.
11. Thykier-Nielsen, S., Mikkelsen, T., Larsen, S. E., Troen, I., de Baas, A. F., Kamada, R., Skupniewicz, C., and Schacher, G., "A Real Time Puff-model for Accidental Releases in Complex Terrain," Proceedings of 2nd International Real Time Workshop, CEC, Luxembourg, 16-19 May 1989.
12. Yamada, T., Bunker, S., and Moss, M., "Numerical Simulations of Atmospheric Transport and Diffusion Over Coastal Complex Terrain," Journal of Applied Meteorology, pp. 565-578, 1991.
13. Yamada, T. and Bunker, S., Three-Dimensional Modeling of Rocket Propellant Dispersion, Report ESC-TR-90-32, Air Force Engineering and Services Center, H.Q. AFESC/RDVS, Tyndall Air Force Base, FL 32403-60001, 1991.
14. Henmi, T. and Yamada, T., "Simulation of the Project WIND Phase I data: Application of the nudging method for incorporation of large-scale wind flow," Monthly Weather Review, 1993.
15. Anthes, R. A., "Data Assimilation and Initialization of Hurricane Prediction Models," Journal of Atmospheric Sciences, vol 31, pp. 702-710, 1974.
16. Hoke, J. E. and Anthes, R. A., "The Initialization of Numerical Models by a Dynamic-Initialization Technique," Monthly Weather Review, vol 104, pp. 1551-1556, 1976.
17. Hoke, J. E. and Anthes, R. A., "Dynamic Initialization of a Three-Dimensional Primitive Equation Model of Hurricane Alma of 1962," Monthly Weather Review, vol 105, pp. 1266-1280, 1977.
18. Cionco, R. M., Project WIND Documentation and User Guide, Phase I: 24-hr Period, 1000 HRS PST, 1 February - 1000 HRS PST, 2 February 1986, US Army Atmospheric Sciences Laboratory, WSMR, NM, 1989.

19. Yamada, T. and Bunker, S., "Development of a Nested Grid, Second Moment Turbulence Closure Model and Application to the 1982 ASCOT Brush Creek Data Simulation," Journal of Applied Meteorology, vol 27, pp. 562-578, 1988.
20. Yamada, T. and Bunker, S., "A Numerical Model Study of Nocturnal Drainage Flows with Strong Wind and Temperature Gradients," Journal of Applied Meteorology, vol 28, pp. 545-554, 1989.
21. Mellor, G. L. and Yamada, T., "Development of a Turbulence Closure Model for Geophysical Fluid Problems," Rev. Geophys. Space Physics, vol 20, pp. 851-875, 1982.
22. Yamada, T., "A Numerical Simulation of Nocturnal Drainage Flow," Journal of Meteorological Society Japan, vol 59, pp. 108-122, 1981.
23. Dyer, A. J. and Hicks, B. B., "Flux-Gradient Relationships in the Constant Flux Layer," Quarterly Journal of the Royal Meteorological Society, vol 96, pp. 715-721, 1970.
24. Yamada, T., "A Numerical Model Study of Turbulent Airflow in and above closure model," Journal of Meteorological Society Japan, vol 60, pp. 439-454, 1982.
25. Richtmyer, R. D. and Morton, K. W., Difference Methods for Initial-Value Problems, 2nd ed., 405 pp., Interscience Publishers, J. Wiley and Sons, New York, 1967.
26. Willmott, C. J., Ackleston, S. G., Davis, R. E., Feddema, J. J., Klink, K. M., Legates, D. R., O'Donnell, J., and Rowe, C. M., "Statistics for the Evaluation and Comparison of Models," Journal of Geophysical Research, vol 90(C5), pp. 8995-9005, 1985.
27. Steyn, D. G. and Mckendry, I. G., "Quantitative and Qualitative Evaluation of a Three-Dimensional Mesoscale Numerical Model Simulation of a Sea Breeze in Complex Terrain," Monthly Weather Review, vol 116, pp. 1914-1926, 1988.
28. Maher, Y. and Pielke, R. A., "The Effects of Topography on Sea and Land Breezes in a Two-Dimensional Numerical Model," Monthly Weather Review, vol 105, pp. 1151-1162, 1977.

29. Maher, Y. and Pielke, R. A., "A Test of an Upstream Spline Interpolation Technique for the Advective Terms in a Numerical Mesoscale Model," Monthly Weather Review, vol 106, pp. 818-830, 1978.
30. Ulrickson, B. L. and Mass, C. F., "Numerical Investigation of Mesoscale Circulations over the Los Angeles Basin, Part I: A Verification Study," Monthly Weather Review, vol 118, pp. 2138-2161, 1990.
31. Yamada, T., "The Critical Richardson Number and the Ratio of the Eddy Transport Coefficients Obtained from a Turbulence Closure Model," Journal of Atmospheric Sciences, vol 32, pp. 926-933, 1975.
32. Musson-Genon, L., "Numerical Simulation of a Fog Event with a One-Dimensional Boundary Layer Model," Monthly Weather Review, vol 115, pp. 593-607, 1987.
33. Sommeria, G. and Deardorff, J. W., "Subgrid-scale condensation in models of nonprecipitating clouds," Journal of Atmospheric Sciences, vol 34, pp. 344-355, 1977.
34. Sommeria, G. and Deardorff, J. W., "Subgrid-scale condensation in models of nonprecipitating clouds," Journal of Atmospheric Sciences, vol 34, pp. 344-355, 1977.
35. Yamada, T. and Mellor, G. L., "A Numerical Simulation of the BOMEX Data Using a Turbulence Closure Model Coupled with Ensemble Cloud Relations," Quarterly Journal of the Royal Meteorological Society, vol 105, pp. 915-944, 1979.
36. Yamada, T. and Kao, C.-Y. J., "A Modeling Study on the Fair Weather Marine Boundary Layer of the GATE," Journal of Atmospheric Sciences, vol 43, pp. 3186-3199, 1986.
37. Oliver, D. A., Lewellen, W. S., and Williamson, G. G., "The interaction between turbulent and radiative transport in the development of fog and low-level stratus," Journal of Atmospheric Sciences, vol 35, pp. 301-316, 1978.
38. Fravallo, C., Fouquart, Y., and Rosset, R., "The sensitivity of a model of low stratiform clouds to radiation," Journal of Atmospheric Sciences, vol 38, pp. 1049-1062, 1981.

39. Hanson, H. P. and Derr, V. E., "Parameterization of radiative flux profiles within layer clouds," Journal of Atmospheric Sciences, vol 11, pp. 1511-1521, 1987.
40. Hanson, H. P. and Derr, V. E., "Parameterization of radiative flux profiles within layer clouds," Journal of Atmospheric Sciences, vol 11, pp. 1511-1521, 1987.
41. Cox, S. K., "Observation of cloud infrared effective emissivity," Journal of Atmospheric Sciences, vol 33, pp. 287-289, 1976.
42. Stephens, G. L., Ackerman, S., and Smith, E. A., "A shortwave parameterization revised to improve cloud absorption," Journal of Atmospheric Sciences, vol 41, pp. 687-690, 1984.
43. Nickerson, E. C., Richard, E., Rosset, R., and Smith, D. R., "The numerical simulation of clouds, rain, and airflow over the Vosges and Black Forest Mountains: a meso- β model with parameterized microphysics," Monthly Weather Review, vol 114, pp. 398-414, 1986.
44. Kessler, E., "On the distribution and continuity of water substance in atmospheric circulation," Meteorological Monograph, American Meteorological Society, vol 10, p. 84, 1969.
45. Van Dop, H., "Buoyant Plume Rise in Lagrangian Framework," Journal of Atmospheric Environment, vol 26A, pp. 1335-1346, 1992.